Master of Science Thesis

Numerical Simulation of Crack Migration in Composite Skin-Stringer Interface

An XFEM-CZM Approach

Malolan Chithathoor Veeravalli Mukunthan

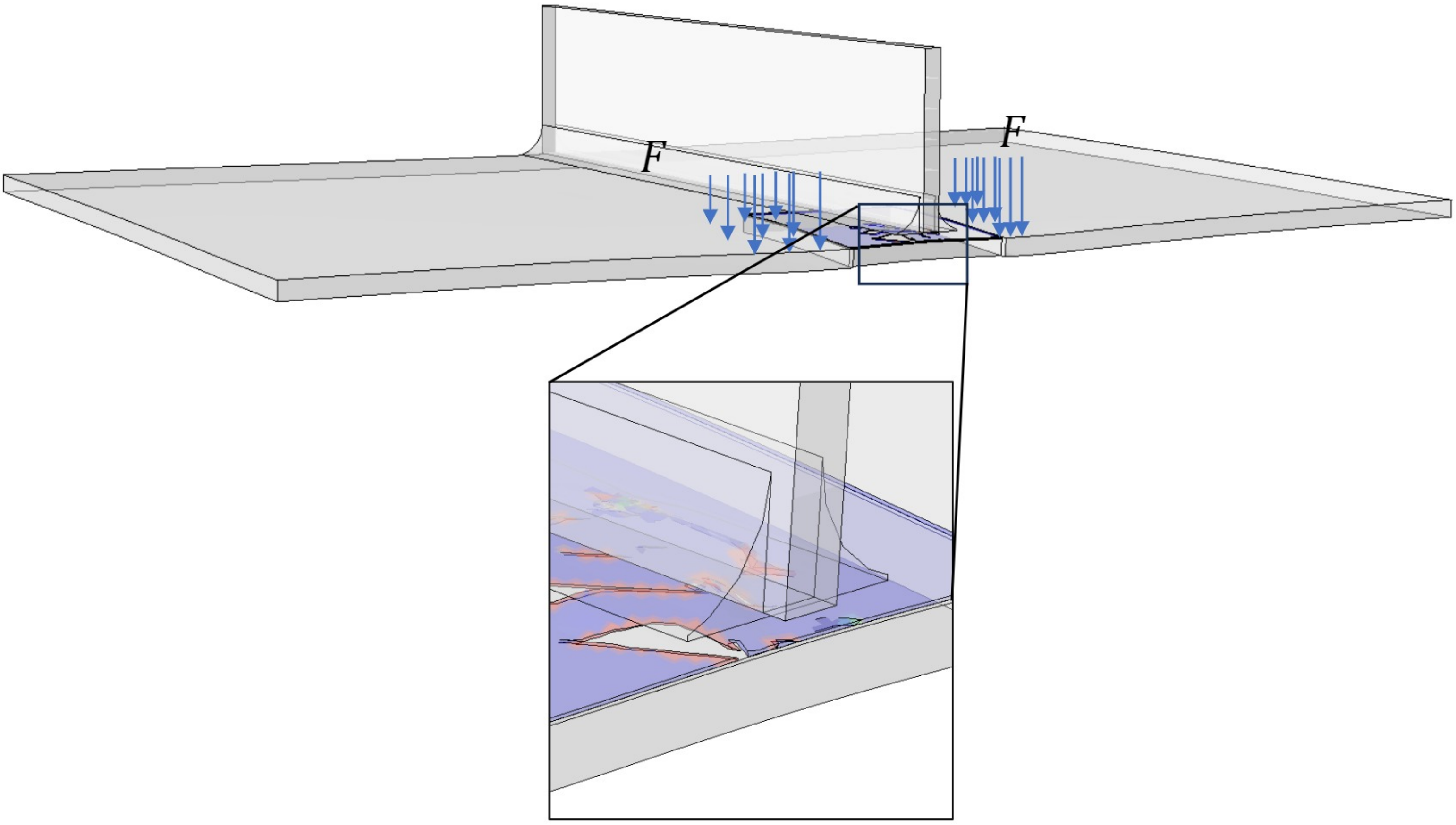

Delft University of Technology

Numerical Simulation of Crack Migration in Composite Skin-Stringer Interface

An XFEM-CZM Approach

Master of Science Thesis

For obtaining the degree of Master of Science in Aerospace Engineering
at Delft University of Technology

Malolan Chithathoor Veeravalli Mukunthan

18th October, 2024

Faculty of Aerospace Engineering · Delft University of Technology

Delft University of Technology
Faculty of Aerospace Engineering
Department of Aerospace Structures and Materials

GRADUATION COMMITTEE

Dated: 18th October, 2024

Chair holder: Dr. B. Chen

Committee members: Dr. S.R. Turteltaub

Dr. C. Kassapoglou

Abstract

In the context of damage tolerance for aeronautical structures, substantial research has focused on simulating skin-stiffener separation in stiffened composite panels. This separation is marked by unstable crack growth at the skin-stiffener interface, which can lead to structural collapse in the post-buckled regime. Recent post-buckling tests on thermoplastic butt-joint single stiffener panels indicate the development of delamination within the skin before crack propagation occurs at the skin-stiffener interface. This delamination is likely triggered by the crack extension process prior to the buckling tests, where the skin was subjected to out-of-plane loads away from the stiffener, promoting the extension of the artificial crack at the interface. It has been hypothesized that this delamination results from crack migration from the skin-stiffener interface into the ply interfaces within the skin. Crack migration, which involves complex interactions between delamination and matrix cracks, is crucial for improving numerical models. For accurate prediction, these models must capture both matrix crack and delamination interactions.

Cohesive zone models, in conjunction with the eXtended Finite Element Method (XFEM) and cohesive elements (CE), have been employed in literature to model the interaction between matrix cracks and delamination. While previous approaches often enrich cohesive elements using user subroutines, this thesis aims to leverage ABAQUS's built-in methods to model crack migration. A series of migration test simulations were conducted to evaluate the combined XFEM and CE approach. The LaRC05 failure criterion in ABAQUS was applied to initiate inclined matrix cracks within the plies, while delamination was modeled with standard 8-node linear cohesive elements. A three-dimensional mesoscale model of the test specimen was developed to simulate the migration test. The LaRC05 criterion successfully captured the orientation changes in matrix cracks due to changes in shear stress, consistent with experimental results. However, the predicted migration distance was 2-3 times greater than observed experimentally. A parametric study revealed that lower matrix strength and fracture energy facilitated migration, although increasing these parameters did not result in a consistent delay in migration, with discrepancies arising at higher values. Despite this, the methodology demonstrated the ability to predict crack migration tendencies and is considered suitable for structural-level applications.

Simulations of the butt-joint thermoplastic skin-stiffener panel under bending were also per-

formed using a global-local modeling approach. The 19-ply skin was meshed with shell elements, while the local model explicitly represented the outer two plies (45/-45) with solid elements and the remaining 17 plies with shell elements. Three modeling approaches were explored: (i) damage only at the skin-stiffener interface, (ii) damage at both the skin-stiffener and ply interfaces (global-local model), and (iii) matrix cracks combined with delamination at both interfaces (global-local model). The first two approaches predicted mode I crack extension at the skin-stiffener interface, with no interlaminar damage in the second approach. However, the third approach using XFEM-CE predicted significant matrix cracking in the outer ply beneath the filler material, which further initiated delamination at the 45/-45 interface. This method successfully predicted delamination migration in the stiffened panel, demonstrating its capability to capture complex damage interactions at the structural level.

Table of Contents

Acknowledgments xvii

1 Introduction 1

2 Literature Review 3

2.1 Damage and crack growth in composite materials 3

2.2 Modelling progressive failure in composites 7

2.2.1 Continuum Damage Approach 8

2.2.2 Discontinuous Approach 9

2.2.3 Application of damage modeling techniques 19

2.3 Skin-stiffener Failure and Simulations 28

3 Methodology 33

3.1 Research Objective and Research Questions 33

3.2 Research Plan 35

4 Crack Migration Test - Modeling 37

4.1 Finite Element Model Description 37

4.2 Test Specimen 37

4.3 Modeling Approach 38

4.4 Material Properties and Failure Criterion 38

4.5 Non-Linear Solution Method 40

4.6 Loads and Boundary Conditions 41

4.7 XFEM Enrichment 42

4.8 Mesh 42

4.9 Study on the Effect of Cohesive Zone Length 43

5 Crack Migration Test - Results **45**
5.1 Mesh Convergence of Solid Elements . . . 45
5.2 Effect of Interface Cohesive Length . . . 46
5.3 Effect of Matrix Strength . . . 51
5.4 Thickness Discretization and Integration Scheme . . . 55
5.5 Parametric Study . . . 58
5.6 Discussion . . . 60

6 Skin-stiffener - Modeling **63**
6.1 Single Stiffener Panel . . . 63
6.2 Panel Modeling Approach . . . 64
6.3 Material Properties . . . 65
6.4 Mesh . . . 67
6.5 Loads and Boundary conditions . . . 68
6.6 Non-Linear Solution Control and Additional Parameters . . . 69
6.7 Studies conducted with the panel . . . 70

7 Skin-stiffener - Results **71**
7.1 Linear Elastic Response . . . 71
7.2 Crack extension at skin-filler interface . . . 72
7.3 Ply Delamination Modeling . . . 73
7.4 Parametric Study: Viscosity . . . 75
7.5 Combined XFEM-CE simulations . . . 78
7.6 Discussion . . . 80

8 Conclusions and Recommendations **81**
8.1 Future scope and recommendation . . . 83

References **84**

List of Figures

2.1 Microcracks 4
2.2 Delamination Migration Test Set-up [1] 6
2.3 Shear Stress sign at delamination front [2] 6
2.4 Delamination propagation and migration [1] 7
2.5 VCCT in 2-dimensions [3] 10
2.6 Stress at the crack tip [4] 12
2.7 Decohesion Element depicted in [5] 12
2.8 Constitutive equations for Pure Mode crack propagation [5] 14
2.10 Restoration of cohesive state taken from [6] 16
2.9 Traction-Separation law for mixed-mode loading conditions 16
2.11 Treatment of cracks using Phantom Node Method [3] 19
2.12 Skin Stiffener debonding simulation taken from [6] 19
2.13 Interface elements used for matrix cracks and delaminations in [2] 20
2.14 Matrix cracks in OHT predicted by interface elements [2] 21
2.15 Matrix cracking in 45° using three approaches [7] 22
2.16 Shear response and failure envelope [8] 23
2.17 Crack propagation under impact load [9] 23
2.18 Crack propagation in multi-direction laminates [10] 23
2.19 Crack migration predicted by crack leading algorithm [10] 24
2.20 Augmenting the cohesive element [11] 26
2.21 Cohesive Element split by floating nodes [12] 27
2.22 Crack migration in DCB specimen [13] 27
2.23 Delamination at butt-joint interface 28
2.24 Comparison between the three levels of local high-fidelity models [14] 29

2.25 Comparison of the load-displacement by FE with experimental response [15] . . . 30
2.26 Skin-stiffener separation predicted by VCCT [15] 30
2.27 Influence of material damage in the constitutive model on the response of skin-stiffener [16] 31
2.28 Difference in prediction of debond area [16] 31

4.1 Crack Migration Test set-up 38
4.2 Modified parameters are highlighted with asterisk 41
4.3 Load applied at L/a_0=1 42
4.4 Mesh and stacking of Crack Migration model 43

5.1 Peak Load variation with decreasing element size 46
5.2 Load response curve plotted for varying delamination cohesive zone length 47
5.3 Deformed configuration of the specimen with coordinate system 48
5.4 Damage in the bottom 0/90 interface cohesive elements 49
5.5 Damage in the top 90/0 interface cohesive elements 49
5.6 Migration location as a function of Cohesive Zone Length 50
5.7 Matrix crack in 90_4 ply block 51
5.8 Force Response with modified matrix strength 52
5.9 Sequence of damage and migration for matrix strength of 33.6 MPa and 43.8 MPa shown along with force response 53
5.10 Crack Migration location for each case 53
5.11 State of damage in the specimen corresponding to the peak before second unstable load drop for the case of matrix strength of 40.32 MPa 54
5.12 Matrix Crack Profiles in 90○ ply block with matrix strength of 33.6 MPa 55
5.13 Migration predicted with single element through the thickness 56
5.14 Migration predicted with single element through the thickness 56
5.15 Migration predicted with single reduced integration element present through the thickness 57
5.16 Migration predicted with four layers of reduced integration element 58
5.17 Effect of matrix strength and fracture energy on the location of migration 60
5.18 Crack Migration location for each case 61

6.1 Panel Geometry and Dimensions 64
6.2 Panel Models 65
6.3 Cross-section with details of high-fidelity model 66
6.4 Partitions in Filler Material 68
6.5 Filler Mesh 68
6.6 Panel Simply Supported Boundary Conditions 69
6.7 Load Application 69

7.1 Reaction forces 72

7.2 Deformed Configuration of Model 1 73
7.3 Force response of skin meshed with shell elements 73
7.4 (a)Damaged cohesive elements in skin-filler interface (b)Mode Mix ratio of the damage in the interface 74
7.5 (a)Damaged cohesive elements in skin-filler interface (b)Damage in 45/-45 interface 75
7.6 (a)Damaged cohesive elements in skin-filler interface in Panel Model 2 with the distance between local regions equal to pre-crack length (b)Damaged cohesive elements in skin-filler interface in Panel Model 2 with the reduced distance between local models (c) Delamination in 45/-45 interface in Panel Model 2 with the distance between local regions equal to pre-crack length (d) Damaged cohesive elements in skin-filler interface in Panel Model 2 with the reduced distance between local models 76
7.7 (a)Peeling in ply interface cohesive elements (b)No delamination in skin observed after the distance between local model was reduced 76
7.8 Reaction force for the above three models 77
7.9 Force response with different viscosities 77
7.10 Crack extension 77
7.11 Damage at the skin-filler interface 78
7.12 Delamination in 45/-45 interface 79
7.13 Matrix cracks in 45° ply 79
7.14 Matrix cracks in 45° ply overlayed on cohesive elements in 45/-45 interface . . . 79
7.15 Cohesive elements in skin-filler interface overlayed on 45° ply 79
7.16 Force response of the applied load 80
7.17 Cross-section and detailed view of matrix cracks in the outer ply which create favorable conditions for crack migration 80

List of Tables

2.1 Damage initiation criterion in ABAQUS [17] 13

4.1 Elastic Properties of IM7/8552 39
4.2 Interlaminar Strength and Fracture Energies 39
4.3 Matrix Strength and Fracture Energies 39
4.4 Parameter study based on l_{cz} 44

5.1 Comparison of peak load obtained with different solid element lengths 46
5.2 Parametric Study with constant delamination properties 59

6.1 AS4D-PEKK Elastic Properties, Strengths and Fracture Energies 66
6.2 Skin-stiffener interface properties 67

7.1 Details of the models tested 72

Acknowledgments

I would like to express my heartfelt gratitude to my supervisor, Dr. Sergio Turteltaub, for his invaluable guidance throughout this thesis. His unwavering support, especially during the challenging final phase, where uncertainties and discrepancies emerged in the results, provided much-needed reassurance. Furthermore, I also extend my gratitude to Andres Pereira for the productive discussions on the results and modeling approach. His input during every session was both motivating and encouraging.

I am equally thankful to my friends, who have been part of this journey. Sharing both the frustrations of undesirable outcomes and the excitement of converged simulations with the DSS group—Aamir, Nathan, Tejas, and Ayush—made this thesis process much more bearable.

Finally, I am deeply grateful to my family and friends back home for being supportive, patient, and understanding during the past two years. Their encouragement has been a constant source of strength.

Delft, University of Technology
18th October, 2024

Malolan Chithathoor Veeravalli Mukunthan

Chapter 1

Introduction

Developing lightweight solutions is one of the highest priorities in the aerospace industry. The main reasons included fuel efficiency and increased payload capacity. Aeronautical structures are mostly constructed using thin-walled structures. These structures are subjected to shear or compressive forces, which often result in buckling. Traditional design philosophy and regulations do not allow aircraft structures to buckle at limited load. Although buckling is essentially the loss of stability of the structure, the structure is prone to failure in the presence of damage. However, the collapse of the structure is not anticipated until the ultimate load. Compliance with this requirement and the use of knockdown factors to compensate for deviations in predicted loads or material properties results in thick over-designed structures. However, allowing thin-walled structures to buckle before the limit load can lead to significant weight savings. This comes with the challenge of ensuring structural integrity under the limit load which calls for damage tolerant designs. Furthermore, using composite materials as a replacement for traditional aerospace metals, due to their low strength-to-weight ratio, has been one solution since the 1960s. Therefore, ensuring damage tolerance of composite structures in the post-buckled state is crucial.

The most common resin system used for composites is thermoset polymers, such as epoxy. They are characterized by low fracture toughness and fail in a brittle manner, which makes them less desirable for damage-tolerant structures. Therefore, novel designs employ high-performance thermoplastic resins, such as PolyEtherEtherKetone (PEEK) and PolyEtherKetoneKetone (PEKK), that have been characterized by higher toughness properties [18]. Carbon fiber/PEEK composites have higher compression after impact, indicating better impact resistance than carbon fiber/epoxy composites. Furthermore, thermoplastic resin systems offer shorter cure cycles and longer shelf life. The use of thermoplastic composites also allows manufacturing techniques such as welding and over-molding of short fiber composites, making it easier to construct fastener-free structures. Concurrent research in the use of thermoplastic composites is aimed at developing primary structures for aeronautical applications. Thermoplastic Affordable Primary Aircraft Structures (TAPAS) consists of several industry and academic partnerships, including TU Delft, that work closely to develop innovative solutions for the application of thermoplastic composites in future aircraft. Some of the innovations include automatic tape placement, robotic welding, and integral structural configurations such as butt-joint stiffened panels. These innovations lead to faster production cycles, reduced part counts, and significant weight savings.

In the context of damage tolerance, several tests have been conducted on butt-joint skin stiffeners to examine their resistance to damage growth. One such research is related to the crack growth in the post-buckled butt-joint skin-stringer. The most common failure mode leading to the collapse of the post-buckled composite panels is skin-stiffener separation. This failure mode is characterized by the unstable crack growth at the skin-stiffener interface. In the case of damaged panels, the crack growth starts from the pre-crack present in the panel. Internal tests were conducted on a single stiffener thermoplastic butt-joint panel with a pre-crack at the interface of the skin and the stiffener. The experiments consisted of interrupted loadings followed by ultrasonic scans (C-scans) to obtain images of damage propagation in the stiffened panel. The experiments revealed that unstable crack growth at the interface was preceded by delamination growth in the skin. The delaminations were observed at various depths from the interface. C-scans conducted before the tests also reveal delaminations within the skin which seem to have initiated during the crack extension process. The crack extension process consists of an out-of-plane displacement applied on the skin forcing the extension of the cack from the PTFE insert.

Numerical models that have been developed earlier for the analysis of the butt joint mostly focused on the failure of the skin-stiffener interface. These models do not predict delaminations in the skin due to the low-fidelity modeling approach. However, it is essential to account for delaminations and through the thickness crack propagation for an accurate representation of the damage process in the panel.

Crack onset and propagation are problems within fracture mechanics. Several advancements have been made in computational fracture mechanics that can be used to model fracture processes such as delaminations and matrix cracks in composites using finite element methods. This thesis aims to utilize such numerical simulation methods to predict the initiation and growth of damage in the stiffened panel that results in delaminations within the skin. Computational fracture mechanics technique will be used to simulate the crack propagation (and migration) to capture the damage process in the skin in a three-point bending simulation.

To solve the problem at the structural level, it is essential to understand damage mechanisms in composites at smaller levels in the structural testing hierarchy. Therefore, the following steps were taken during this thesis:

1. A Literature study was be carried out to understand the following concepts
   (a) Crack growth in composites
   (b) Computational fracture mechanics used in composite damage simulations
   (c) Numerical methods used to predict progressive damage in stiffened panels
2. A computational fracture mechanics method was selected to model damage growth in composite laminates
3. Methodology was tested at a coupon level and was validated with data from literature
4. A Numerical model of the stiffened panel was developed and the chosen methodology was used to predict damage in the panel

Chapter 2

Literature Review

In this chapter, the theoretical background required for the thesis is presented. The first section of this chapter gives an overview of the experimental studies that have been carried out to understand crack growth mechanisms in composite laminates. The following section covers the common computational methods used to model damage initiation and propagation specifically in composite materials. The final section gives an overview of post-buckling studies performed numerically that account for progressive damage growth. The objective of this chapter is to present the literature that has been perused to identify methods suitable for the numerical study that will be carried out in this thesis.

2.1 Damage and crack growth in composite materials

Damage in composite materials is often present as matrix cracks, delaminations, and fiber breakage [19]. Matrix cracks in composites result from the manufacturing process due to the differences in thermal expansion coefficient between the matrix and the fiber. The high residual tensile stress in the matrix leads to microcracks as shown in (Figure 2.1) [20]. Larger cracks such as delaminations in the aircraft structure are caused by impact loads such as tool drops or runway debris. The growth of cracks in composites occurs much more easily in the matrix due to its lower fracture toughness. Within the ply, the crack growth is arrested near the fiber due to the higher stiffness of the fiber. At very small scales, these cracks do not compromise the strength of the ply. However, when these plies are subjected to significant transverse stresses the microcracks grow to a macroscopic scale which has a detrimental effect on the ply's strength and stiffness. The macro-crack runs through the thickness of the ply between the fibers. At the level of a laminate, the growth of matrix cracks can be arrested by adjacent plies that are oriented at a different angle. These matrix cracks can continue propagating at the interface of these plies as delamination divides the plies into sub-laminates with lower strength and stiffness. In the context of damage tolerance, the growth of such damage can be controlled by choosing an appropriate ply stacking sequence. Hallet et al [21] highlights the influence of the stacking sequence on the growth of damage and the final catastrophic failure of notched composite laminates.

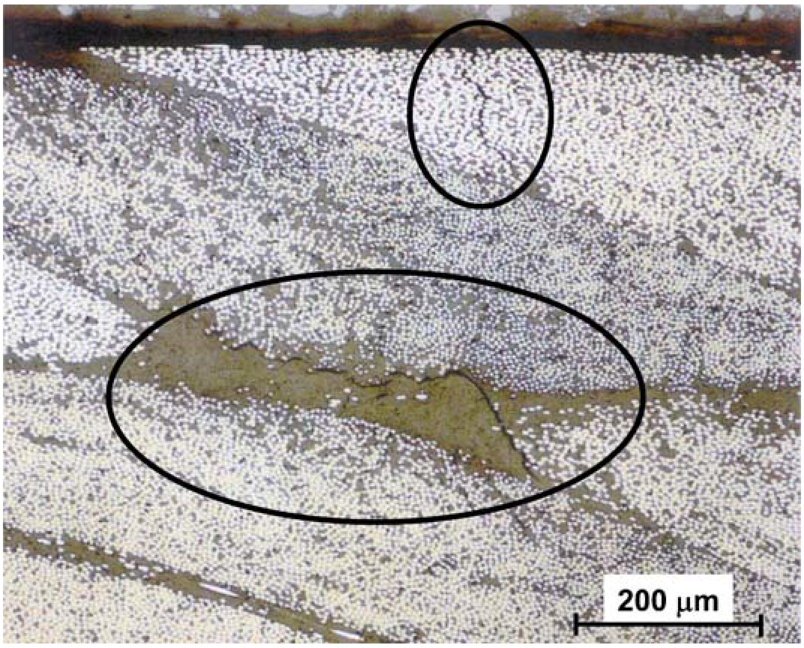

Figure 2.1: Microcracks
[20]

A study on the size effect of Open Hole Tensile (OHT) strength was carried out in [21] which describes the effect of the composite layup on crack growth through the thickness in a notched laminate. The authors performed interrupted OHT tests to examine the damage propagation using X-rays and C-scans. The dimensions of the test specimens were scaled in 3 levels to study the size effect on the strength of the laminate. The first level was thickness scaling (1D); 2D scaling constituted scaling the in-plane dimensions i.e., length, width, and hole radius; and simultaneous scaling of all dimensions was 3D scaling. The thickness of the quasi-isotropic laminate was scaled using two methods: ply-level scaling and sub-laminate-level scaling. The ply level scaling blocked similar plies together resulting in a layup such as $[45_n/90_n/-45_n/0_n]_s$. The sub-laminate level scaling repeated the base layup to the required number $[45/90/\text{-}45/0]_{ns}$.

The final failure of the notched laminate is classified into brittle failure, pull-out failure, or delamination. The brittle failure consisted of fiber failure with a crack running through the width and thickness, resulting in a flat surface of the cracked specimen. A pull-out failure was characterized by fiber failure but significant delaminations and ply splits resulted in plies pulling apart. The delamination-type failure consisted of delaminations running from the hole edge to the grips of the coupon with no fiber failures. In all these cases a sequence of sub-critical damages preceded the final failure. In the ply-level scaled specimen, the matrix cracks were initiated in the 90° plies. This was followed by matrix cracks in the 45° and −45° plies. These matrix cracks ran through the block of plies resulting in local delaminations at the hole edge. The cracks terminated at the -45/0 interface near the 0° block. The matrix cracks in the 0° ply occurred as splits in an asymmetric direction due to asymmetric delamination in the -45/0 interface. Ply splits in 0° ply redistributed the stress delaying fiber failure.

The next stage of damage involved the formation of an inner delamination region near the hole edge. The matrix cracks and local delaminations formed in the previous stage interact as the delamination region expands. The delamination propagates through the thickness by stepping down through matrix cracks within the adjacent plies. Following this, delamination continued to propagate across the width of the laminate in the off-axis ply interfaces. A free-edge delamination also occurred in these interfaces. The interaction of the delamination from the inner region and the free-edge delamination resulted in a full-width outer region delamination. The outer delamination zone was enclosed by the matrix cracks of the off-axis plies.

A load drop in the load-displacement curve characterizes the final catastrophic failure. The observed mode of failure was different for the ply-level scaled specimens and sub-laminate-level scaled specimens. In the case of sublaminate level scaling, matrix cracks, and local delaminations are arrested by the 0° ply present in the outer sublaminate. Matrix cracks occur symmetrically in this ply and delaminations are significantly restricted. Thus the final failure is characterized by pull-out or brittle failure. The interrupted tests reveal that most of the sub-critical damages were not visible until 95% of the failure load. However, the ply-level scaled specimens mostly failed due to delaminations since the blocking of similar plies together allowed the propagation of matrix cracks and delaminations. The final failure of the notched laminate is significantly influenced by the extent to which matrix cracks and delaminations are allowed to propagate.

The damage tolerance of a structure is assessed by the extent to which damage growth exists at high load. In the case of composite materials, the matrix cracks can be initiated early in the loading stage due to the low strength of the resin. The presence of matrix cracks can allow relocation or propagation of delaminations from one interface to the other as observed in the notched laminate. The relocation of delamination to adjacent interfaces through matrix cracks in the off-axis plies termed delamination migration. Experimental research has been carried out extensively to understand conditions that make it favorable for delamination migration to occur [1],[2]. Ratcliffe et al [1] developed a test to characterize delamination migration in cross-ply laminates. The test consists of a 44-ply carbon/epoxy composite laminate with a PTFE insert between a 0° and a block of four 90° plies at the midplane. The layup and geometry of the test setup are shown in Figure 2.2. The PTFE insert acts as a pre-crack and divides the laminate into two sublaminates. The upper sublaminate consists of the transverse plies close to the pre-crack. This sublaminate is loaded using displacement control and the load is coincident with the pre-crack front $L = a_0$. Where L is the distance of the load point and a_0 is the length of the pre-crack. This load introduces a local negative shear stress at the pre-crack front resulting in the crack kinking towards the bottom sublaminate, as shown in Figure 2.3. However, the crack is confined by the 0° ply present below the pre-crack. Therefore, it is energetically favorable for the crack to propagate along the surface of the 0° resulting in a delamination at the 90/0 interface. As the load continues to be applied, the delamination propagates skimming the top surface of the 0 ply up to a certain distance after which the shear stress sign changes. Consequently, the delamination kinks towards the stack of 90° plies in the upper-sublaminate resulting in a matrix crack in these plies. As the crack propagates through the transverse plies, it is arrested by the 0° ply in the upper sublaminate present above the 90° ply block. This is followed by the crack propagating as a delamination on the top 0/90 interface as can be seen in Figure 2.4. In the cases where the load application point on the sublaminate was $L > a_o$, the migration location occurred closer to the load application point. This is attributed to the mixed-mode loading that causes the delamination before the migration event. However, the sequence of damage remained consistent in every case.

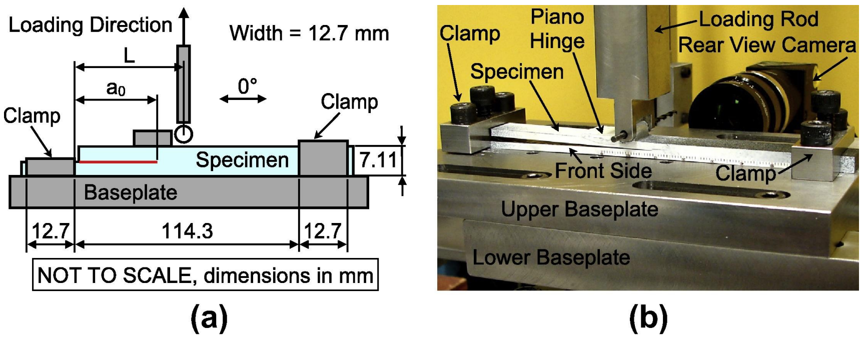

Figure 2.2: Delamination Migration Test Set-up [1]

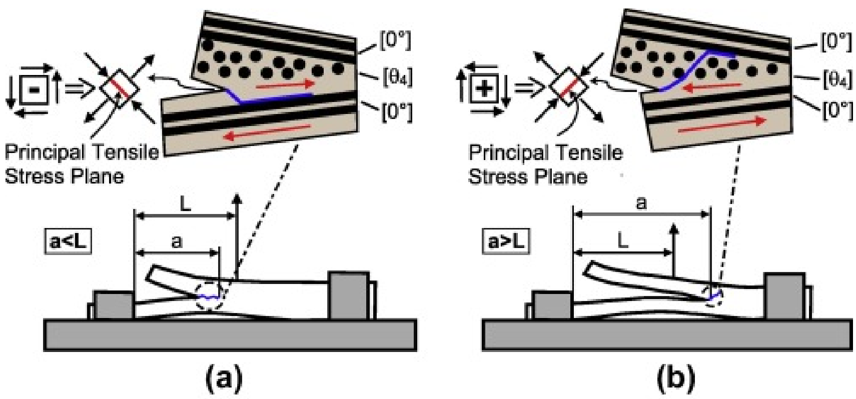

Figure 2.3: Shear Stress sign at delamination front [2]

A similar test by Pernice et al [2] was developed for laminates with plies oriented at 60° and 75°. In the case of the cross-ply laminates, the shear stress and the mixed-mode loading are uniform across the width of the laminate. Therefore, the delamination migration occurs at the same location across the width of the laminate. However, for other orientations, the shear stress distribution across the width of the laminate is not uniform. The migration event is preceded by multiple crack-kinking events. Cracks are either arrested by the top 0-degree plies or the kinked crack fails to propagate through the θ ply stack due to energetically unfavorable conditions. The location of migration is also different along the two lateral edges of the specimen. The migration was observed to occur when two independently kinked cracks within the laminate propagated to the top $0/\theta$ interface. This is unlike the cross-ply laminate where a single crack delaminates and propagates through the transverse plies.

The above experiments highlight the complexity involved in matrix-dominated damage in composite laminates. The interaction of matrix cracks and delamination has been observed in composite structures subjected to low-velocity impact. It has also been observed during skin-stiffener separation of post-buckled panels in some cases. End-notched flexure (ENF) experiments that were used to determine Mode II fracture toughness in angle-plied laminates have also reported the occurrence of delamination migrating through plies due to matrix cracks. The focus of this thesis is the progressive damage analysis of the thermoplastic

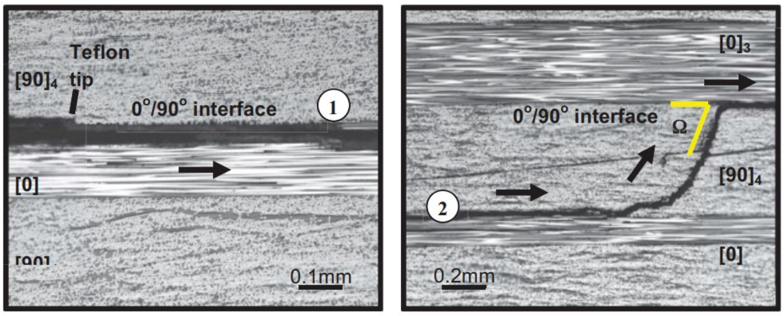

Figure 2.4: Delamination propagation and migration [1]

butt-joint skin-stringer under post-buckling which consists of a pre-crack at the skin-stiffener interface. Multiple delaminations have been observed before the collapse of the panel and these may be attributed to the interaction of skin-stiffener debond and matrix cracks present in the adjacent plies. The propagation of these cracks may have resulted in delaminations in the structure. To ensure the damage tolerance of the thermoplastic-butt joint skin-stiffener, the damage analysis will require high-fidelity numerical simulations that account for interactions between intralaminar and interlaminar failure that enable the migration of delamination. Therefore, it is necessary to identify the damage modeling technique that can capture such interactions.

2.2 Modelling progressive failure in composites

When using finite element methods to computationally model crack initiation and propagation, it was often necessary to employ remeshing strategies. A fine mesh was needed near the crack tip to capture the crack singularity accurately. After each increment, a new mesh generation algorithm would be required. As the crack size increased, the size of the stiffness matrix would also significantly increase. It's important to note that this issue arose when modeling crack initiation and propagation in 2D plane strain simulations of isotropic materials. Predicting failure in composite laminates is challenging due to the multi-scale nature of composite materials and 3-dimensional stress states. Moreover, predicting local damage initiation does not represent the failure of the structure therefore progressive failure analysis is required. Therefore, the various damage modes and their interactions must be accounted for to accurately determine the maximum load-carrying capacity of a structure [22]. Commercial finite element codes have proven to be versatile in modeling the structural behavior of complex geometries. Integration of damage models with finite element codes has improved the predictive capability of structural simulation. The computational methods that are currently used widely are based on fracture mechanics. The energy release rate is computed and compared with a critical energy release rate of the material to predict crack propagation. These methods are divided into continuum and discontinuous approaches [22].

2.2.1 Continuum Damage Approach

The continuum damage mechanics approach involves cohesive cracks that are smeared over the domain of an element. The damage is initiated based on a particular failure criterion such as the maximum principal stress criterion or other interactive criterion. The propagation of damage is modeled as the reduction of stiffness by including a damage variable in the constitutive relation of the material. For example, Hooke's law is expressed in the tensor notation as,

$$\sigma = \mathbf{D}\epsilon \tag{2.1}$$

Where σ and ϵ are the stress and strain tensors, $\mathbf{D}$ is the material stiffness or elastic matrix which is a function of the material's elastic modulus and Poisson ratio. To account for damage, the equation is modified to account for isotropic stiffness reduction in the presence of a crack,

$$\sigma = (1-\omega)\mathbf{D}\epsilon \tag{2.2}$$

Where ω represents a damage variable ranging from 0 to 1. Any value above 0 indicates the onset and propagation of damage, while 1 signifies complete material failure. This method has been used extensively for damage models of composite laminates in literature [23],[24]. In [23], Maimi et al developed a constitutive relation for composites where three damage variables account for the failure of the constituents of the material. This is achieved by defining a scalar-valued function based on the complementary free energy,

$$\begin{aligned} G = &\frac{\sigma_{11}^2}{2\left(1-\mathrm{d}_1\right)E_1} + \frac{\sigma_{22}^2}{2\left(1-\mathrm{d}_2\right)E_2} - \frac{\nu_{12}}{E_1}\sigma_{11}\sigma_{22} + \frac{\sigma_{12}^2}{2\left(1-\mathrm{d}_6\right)G_{12}} + \left(\alpha_{11}\sigma_{11}+\alpha_{22}\sigma_{22}\right)\Delta T \\ &+ \left(\beta_{11}\sigma_{11}+\beta_{22}\sigma_{22}\right)\Delta M \end{aligned} \tag{2.3}$$

Where d_1, d_2 and d_6 are the damage variables corresponding to fiber failure, matrix failure, and transfer or longitudinal cracks. Since the damage process is thermodynamically irreversible, the energy dissipated due to damage onset and propagation must be positive. This leads to,

$$\dot{G} - \dot{\sigma} : \varepsilon \geqslant 0 \tag{2.4}$$

The expansion of the above equation results in,

$$\varepsilon = \frac{\partial G}{\partial \sigma} = \mathbf{H} : \sigma + \alpha\Delta T + \beta\Delta M \tag{2.5}$$

Where is $\mathbf{H}$ is called the laminate compliance tensor which relates the strain to the stress,

$$\mathbf{H} = \frac{\partial^2 G}{\partial \sigma^2} = \begin{bmatrix} \frac{1}{(1-\mathrm{d}_1)E_1} & -\frac{\nu_{21}}{E_2} & 0 \\ -\frac{\nu_{12}}{E_1} & \frac{1}{(1-\mathrm{d}_2)E_2} & 0 \\ 0 & 0 & \frac{1}{(1-\mathrm{d}_6)G_{12}} \end{bmatrix} \tag{2.6}$$

The damage variables within this tensor are zero within the elastic domain and reach a value of 1 at complete failure, mirroring the behavior observed in isotropic materials. The initiation of damage and the onset of material softening are determined based on composite failure criteria, such as LaRC03-04. As the material continues to be loaded, the damage variable evolves, ensuring that the energy associated with this damage remains non-negative, and the total energy dissipated is equal to the fracture energy specific to the failure mode. Moreover, the effect of crack closure under load reversal on the evolution of the damage variables was also considered in this methodology.

Furtado et al extended this method in [24] to incorporate the effects of stress through the thickness on longitudinal compressive strength and fracture energy. The damage model developed was utilized to simulate the initiation of damage and failure in composite coupons consisting of three aerospace-grade carbon epoxy laminates. The numerical simulations yielded results that exhibited a strong correlation with experimental data. It is worth noting that these methods do not necessarily represent a crack in the geometry; rather, the damage is localized in a row of elements. The damage propagates along these mesh lines, therefore accurate results can be obtained only if the mesh is aligned along the crack path. Mesh dependency is also a major drawback in CDM, where an increase in mesh density leads to energy dissipation tending toward zero in each element [22]. This is resolved by determining the softening slopes as a function of the fracture energy and the characteristic element length as proposed by Bazant et al in [25]. Furthermore, the damage modes modeled using this method are often limited to intralaminar failures. To account for intralaminar damage, discontinuous methods are used. For instance, cohesive elements were used to model delamination in [24].

2.2.2 Discontinuous Approach

In this method, the discontinuity in the material such as cracks, voids, or other non-conformities is modeled by accounting for the separation or jump in the displacement field across the discontinuous boundaries. Such methods are suitable for modeling composite failures such as delamination and skin-stiffener separation. The discontinuous methods that are commonly used in finite element codes are the Cohesive Zone Models (CZM), Extended Finite Elements (XFEM) and, Virtual Crack Closure Technique. This section provides an overview of these methods.

Virtual Crack Closure Technique (VCCT)

VCCT is based on the assumption that the energy dissipated during a crack's advancement by a certain length is equal to the work required to close the crack of the same length [26]. This method is computationally efficient since it depends on the finite element solution and computing the energy can be considered a post-processing step. The energy is determined based on nodal forces at the crack tip and the nodal separations in the wake of the crack as shown in Figure 2.5. The crack is assumed to grow self-similarly and the energy release rates corresponding to the crack opening modes are determined using Equation 2.7.

$$\begin{array}{ll} G_I = \frac{1}{2\Delta a} F_{Yi} \cdot \Delta \nu_{k,j} & \Delta \nu_{k,j} = \nu_k - \nu_j \\ G_{II} = \frac{1}{2\Delta a} F_{Xi} \cdot \Delta u_{k,j} & \Delta u_{k,j} = u_k - u_j \end{array} \tag{2.7}$$

Where, F_x and F_y are the nodal forces, Δa is the length of the element such that $\Delta a \cdot 1$ is the area of the crack. $\Delta \nu_{k,j}$ and $\Delta u_{k,j}$ are the differences in the displacements between the nodes k and j present in the wake of the crack.

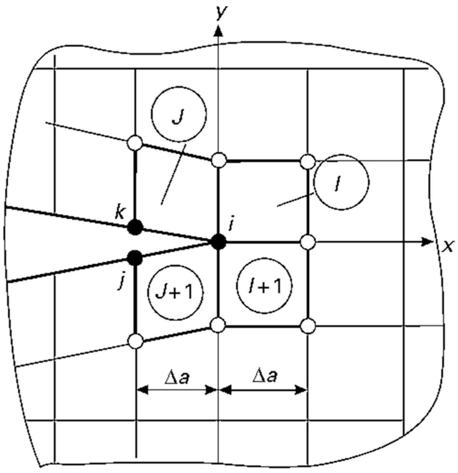

Figure 2.5: VCCT in 2-dimensions [3]

The above expression is suitable for crack growth analysis in the plane strain configuration where the energy release rate corresponding to mode III crack opening can be ignored. However, delaminations often occur in the plane of the laminate and are highly dependent on mixed mode ratios [26]. In 3-dimensions, the energy release rate corresponding to Mode III is found using an expression similar to Equation 2.7,

$$\begin{array}{ll} G_I = \frac{1}{2\Delta A} F_{Yi} \cdot \Delta \nu_{k,j} & \Delta \nu_{k,j} = \nu_k - \nu_j \\ G_{II} = \frac{1}{2\Delta A} F_{Xi} \cdot \Delta u_{k,j} & \Delta u_{k,j} = u_k - u_j \\ G_{III} = \frac{1}{2\Delta A} F_{zi} \cdot \Delta w_{k,j} & \Delta w_{k,j} = w_k - w_j \end{array} \tag{2.8}$$

Here ΔA is the area of the crack. The total strain energy release rate is computed by,

$$G_T = G_I + G_{II} + G_{III} \tag{2.9}$$

The critical strain energy release rate determines the onset of delamination. In [26] the maximum of G_T is determined in a laminate with a pre-crack. Failure onset is assumed to occur when the maximum G_T is equal to or greater than the critical SERR. This method is suitable for analysis where a stationary crack is modeled. However, delamination is progressive damage and the structure can handle higher loads. Therefore, to model delamination propagation the total SERR is often compared with a critical SERR determined using the BK criterion as shown in [15][27]. The ratio of the total SERR and critical SERR must be 1 for the delamination to propagate as given by,

$$\frac{(G_I + G_{II} + G_{III})}{(G_{IC} + (G_{IIC} - G_{IC}) \left[(G_{II} + G_{III} / (G_I + G_{II} + G_{III} \right]^{\eta})} = 1 \tag{2.10}$$

Cohesive Zone Model

Despite the computational efficiency of VCCT, one drawback of the method is that the model requires the pre-crack to be defined to determine the ERR. In some cases, deciding on the crack front of the delamination can be challenging, and the crack growth may not be self-similar, meaning the shape of the delamination front may change during loading. One solution to alleviate this problem is the use of interface or decohesion elements [5][6][4]. These elements can be placed in potential crack paths to model crack onset and propagation. For instance, cohesive elements can be placed between plies in a finite element model of a composite laminate to model delamination. All these models are developed based on the concept of cohesive zone or process zone where a softening zone exists at the crack tip.

The Linear Elastic Fracture Mechanics (LEFM) theory predicts infinite stresses at the crack tip, but such stress singularities are not physically realistic for any material. Therefore alternate models are required to predict the stress state at the crack tip that can accurately determine crack propagation. In the case of metals, elasto-plastic models are used, where it is assumed that the yield strength limits the stress near the crack tip. Further loading of the cracked material results in a region with plastic deformation at the crack tip, as proposed by Dugdale in [28]. For brittle materials like polymers or resins, where the extent of plastic deformation is not as pronounced as in metals, Barenblatt proposed that the stress is limited by the material's tensile strength [6]. Dugdale in 1960 determined the ratio of applied load and yield stress such that metal yielding can be avoided in the cracked plate. However, these methods do not allow crack growth and, hence, cannot be used to model propagating cracks. The cohesive zone theory used for the interface or decohesion elements is based on the strength of materials approach, where the onset of damage at the crack tip is determined by the material strength. The evolution or growth of the crack is determined by the fracture energy approach. This concept was used by Mi et al in [4], as shown in Figure Figure 2.6, to develop a plane strain interface element which was used to model mixed-mode delamination. Here, stress at the tip of the cohesive zone or the process zone is maximum and is limited by the tensile strength and the stress in the wake of this tip reduces to a zero where the material has completely failed. This concept has been used often to develop damage law for cohesive or interface elements.

Camanaho et al implemented the cohesive zone theory using an 8-noded 'zero-thickness' element which was used to represent the ply interface in composite materials in [5]. In this work, a constitutive relation is established between the stress and the nodal separation. The nodal separation or displacement discontinuity represents the crack in the model. This element developed in [5] is similar to the cohesive elements implemented in ABAQUS. The implementation begins with defining the nodal displacement fields using the following expression:

$$\left.\begin{aligned} u_i^+ &= N_k u_{ki}^+, k \in \{\text{ top nodes }\} \\ u_i^- &= N_k u_{ki}^-, k \in \{\text{bottom nodes}\} \end{aligned}\right\} \tag{2.11}$$

Where i is the direction of the displacement in the coordinate system used and k represents the location of the nodes. The top nodes and bottom nodes can be observed in Figure 2.7. The top and bottom surfaces of these elements are connected to the surfaces of the solid elements that are adjacent to the cohesive elements. The displacement of the solid elements results in the displacement and hence the separation of the nodes in the cohesive elements. This separation or relative displacement is expressed by,

$$\Delta_i = u_i^+ - u_i^- \tag{2.12}$$

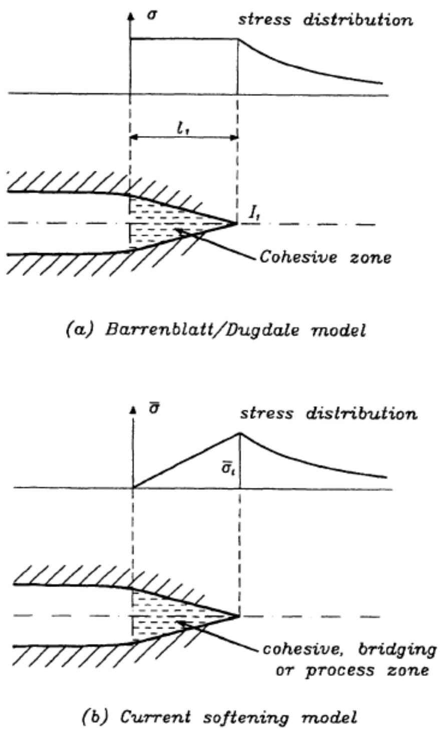

Figure 2.6: Stress at the crack tip [4]

Therefore, the relative displacement or the separation field can be expressed as,

$$\Delta_i = \bar{N}_k u_{ki} \tag{2.13}$$

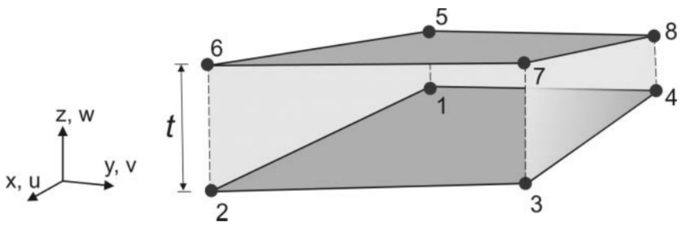

Figure 2.7: Decohesion Element depicted in [5]

Where,

$$\bar{N}_k = \begin{cases} N_k, k \in \{\text{ top nodes }\} \\ -N_k, k \in \{\text{bottom nodes}\} \end{cases} \tag{2.14}$$

The separation in Equation 2.13 is expressed in the global coordinates. However, the displacement field must be transformed into local coordinates for a general element in a discretized model. This transformation is carried out by defining direction cosines that are used to construct the transformation matrix. The transformed displacement field is now denoted as δ_r. The constitutive relation between the nodal tractions and separation is expressed by,

$$\tau_s = \bar{\delta}_{sr} D_{sr} \delta_r \tag{2.15}$$

Where δ_{sr} is the Kronecker delta, used to set the non-diagonal components of the stiffness tensor D_{sr} to zero. These diagonal terms are referred to as penalty stiffness K, expressed as a function of the material's elastic modulus and thickness of the interface. This relation can be expressed in the matrix form as shown in the ABAQUS documentation [17],

$$\mathbf{t} = \left\{ \begin{array}{c} t_n \\ t_s \\ t_t \end{array} \right\} = \left[\begin{array}{ccc} K_{nn} & K_{ns} & K_{nt} \\ K_{ns} & K_{ss} & K_{st} \\ K_{nt} & K_{st} & K_{tt} \end{array} \right] \left\{ \begin{array}{c} \varepsilon_n \\ \varepsilon_s \\ \varepsilon_t \end{array} \right\} = \mathbf{K}\varepsilon. \tag{2.16}$$

Where,

$$\varepsilon_n = \frac{\delta_n}{T_o}, \varepsilon_s = \frac{\delta_s}{T_o}, \varepsilon_t = \frac{\delta_t}{T_o}.$$

Here, the tractions are related to strains through a coupled stiffness matrix. The user is free to choose whether the traction-separation behavior is coupled or uncoupled. Uncoupled behavior would set the off-diagonal terms to zero. In the strain expression, ABAQUS sets T_o to 1 by default to ensure the strain equals the relative displacement. This constitutive relation is used to determine the internal force vector and thus the tangent stiffness matrix of the cohesive element as shown in the following equations [22],

$$\mathbf{f}^{\text{int}} = \int_{\Gamma_i} \overline{\mathbf{N}}^T \mathbf{t} \mathrm{d}\Gamma \tag{2.17}$$

$$\begin{gathered} \mathbf{K} = \int_{\Gamma_i} \overline{\mathbf{N}}^T \mathbf{D} \mathbf{N} \mathrm{d}\Gamma \\ \mathbf{D} = \frac{\partial \mathbf{t}}{\partial \mathbf{u}} \end{gathered} \tag{2.18}$$

The subsequent step in defining the constitutive behavior of the cohesive element is to implement the damage model. This consists of specifying the damage initiation criterion and damage evolution parameters. The damage initiation is a strength-based criterion as mentioned earlier. ABAQUS allows the user to choose among the following failure criteria:

Maximum Nominal stress criterion :	$max\left\{\frac{\langle t_n \rangle}{t_n^\circ}, \frac{t_s}{t_s^\circ}, \frac{t_t}{t_t^\circ}\right\} = 1$
Maximum nominal strain criterion :	$max\left\{\frac{\langle \epsilon_n \rangle}{\epsilon_n^\circ}, \frac{\epsilon_s}{\epsilon_s^\circ}, \frac{\epsilon_t}{\epsilon_t^\circ}\right\} = 1$
Quadratic nominal stress criterion :	$\left(\frac{\langle t_n \rangle}{t_n^\circ}\right)^2 + \left(\frac{t_s}{t_s^\circ}\right)^2 + \left(\frac{t_t}{t_t^\circ}\right)^2 = 1$
Quadratic nominal strain criterion :	$\left(\frac{\langle \epsilon_n \rangle}{\epsilon_n^\circ}\right)^2 + \left(\frac{\epsilon_s}{\epsilon_s^\circ}\right)^2 + \left(\frac{\epsilon_t}{\epsilon_t^\circ}\right)^2 = 1$

Table 2.1: Damage initiation criterion in ABAQUS [17]

For the damage evolution, the fracture energy in modes I, II, and III need to be specified. A constitutive relation for pure mode crack propagation typically looks like the curve in

Figure 2.8. The linear response of the element is governed by the penalty stiffness. The stiffness degradation begins when the traction in the element satisfies the damage initiation criterion. The area under the curve in the constitutive relation shown is equal to the fracture energy as shown in Equation 2.19. This equation is used to determine the maximum separation that results in complete failure.

$$\begin{aligned}\int_0^{\delta_3^f} \tau_3 d\delta_3 = G_{IC}, \delta_3^f = \frac{G_{IC}}{2\tau_3^{max}} \\ \int_0^{\delta_2^f} \tau_2 d\delta_2 = G_{IIC}, \delta_2^f = \frac{G_{IIC}}{2\tau_2^{max}} \\ \int_0^{\delta_1^f} \tau_1 d\delta_1 = G_{IIIC}, \delta_1^f = \frac{G_{IIIC}}{2\tau_1^{max}}\end{aligned} \tag{2.19}$$

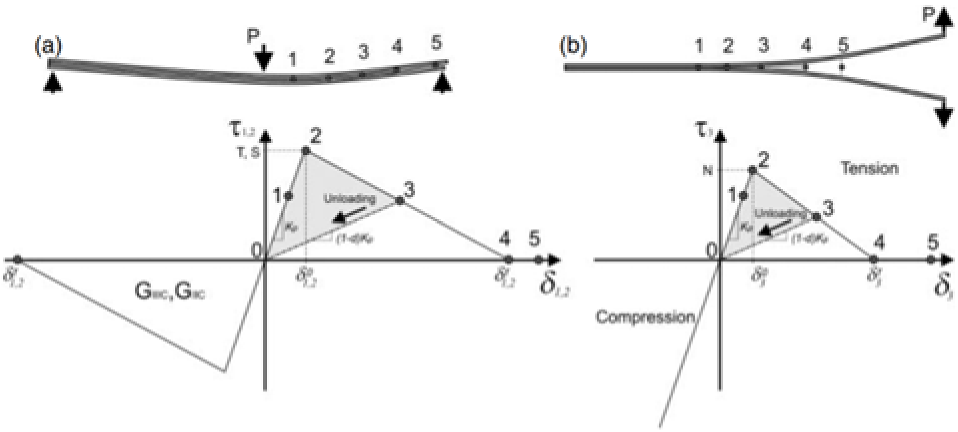

Figure 2.8: Constitutive equations for Pure Mode crack propagation [5]

Having established the limits of the displacements, the softening behavior of the cohesive element is determined using the following expression. Here, δ_i^{max} is the maximum separation that occurs in the loading history of the element. This quantity ensures the irreversibility of the damage in the element. In the case of unloading, the separation δ_i follows the second degraded stiffness as can be seen in the Figure 2.8.

$$\tau_i = \begin{cases} K\delta_i, \delta_i^{max} \leq \delta_i^{\circ} \\ (1-d_i)K\delta_i, \delta_i^{\circ} < \delta_i^{max} < \delta_i^f \\ 0, \delta_i^{max} \geq \delta_i^f \end{cases} \tag{2.20}$$

Delamination propagation in composite structures has a mixed-mode characteristic. Therefore, the constitutive formulation in [5] is extended to account for the proportion of displacement in the normal and shear directions [17]. In this formulation, an effective nodal separation is computed as a norm of the separations in the three directions.

$$\delta_m = \sqrt{\delta_1^2 + \delta_2^2 + \rangle\delta_3^2\rangle}\delta_{shear} = \sqrt{\delta_1^2 + \delta_2^2} \tag{2.21}$$

In the mixed-mode constitutive law, a strength-based damage initiation criterion such as the quadratic criterion is used to deal with the interaction of the normal and shear tractions. The displacement corresponding to the onset of damage is found as a function of the mode-mix ratio. Mode mix ratio is the proportion of shear displacement and the normal displacement denoted by β,

$$\beta = \delta_{shear}\delta_3 \tag{2.22}$$

For mixed-mode loading the dependence of the fracture toughness on mode ratio must be accounted for in the formulation of decohesion elements. Under Mixed-modes I and II, the fracture surfaces reveal complex crack growth mechanisms compared to pure mode crack propagation. Therefore, interactive failure criteria were developed that are a function of the pure mode fracture energies. Examples of those include the Power Law and the BK Criterion.

$$\left(\frac{G_I}{G_{IC}}\right)^{\alpha} + \left(\frac{G_{II}}{G_{IIC}}\right)^{\alpha} = 1 \tag{2.23}$$

$$\begin{aligned} G_{IC} + (G_{IIC} - G_{IC})\left(\frac{G_{II}}{G_T}\right)^{\eta} &= G_C \\ G_T &= G_I + G_{II} \end{aligned} \tag{2.24}$$

The failure criterion is used to determine the critical fracture energy, or the area under the constitutive curve, to determine the final relative displacement that leads to the complete failure of the cohesive element under mixed-mode conditions. This is done by determining the energy release rates corresponding to the normal and shear displacements of the element using,

$$G_I = \frac{K\delta_m^{3f}\delta_m^{3\circ}}{2} G_{shear} = \frac{K\delta_m^{shearf}\delta_m^{shear\circ}}{2} \tag{2.25}$$

Where δ_m^{3f},$\delta_m^{3\circ}$,δ_m^{shearf} and $\delta_m^{shear\circ}$ are determined from,

$$\delta_m^{3f} = \delta^{3f}/\sqrt{1+\beta^2}$$

The final displacement corresponding to the mixed-mode cohesive law is determined to establish the relative mixed-mode displacement that leads to the complete failure of the element. The final constitutive relation between the tractions and relative mixed-mode displacement is given by,

$$\delta_m^f = \begin{cases} \frac{2}{K\delta_m^\circ}\left[G_{IC} + (G_{IIC} - G_{IC})\left(\frac{\beta^2}{1+\beta^2}\right)^{\eta}\right], \delta_3 > 0 \\ \sqrt{(\delta_1^f)^2 + (\delta_2^f)^2}, \delta_3 \leq 0 \end{cases} \tag{2.26}$$

Figure 2.9 shows the bilinear softening law for mixed-mode loading conditions. The shaded regions projected on the Mode I and shear mode planes represent the fracture energies corresponding to the normal and shear m displacements when the mixed mode ratio is accounted for.

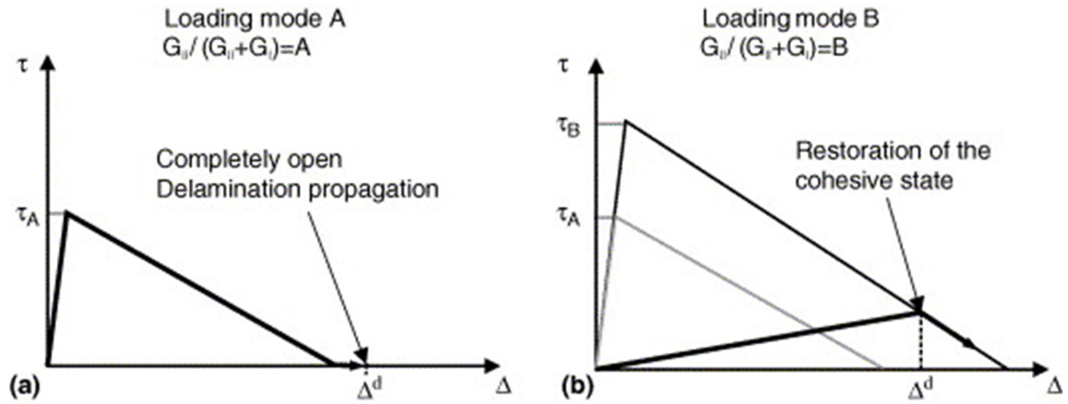

Figure 2.10: Restoration of cohesive state taken from [6]

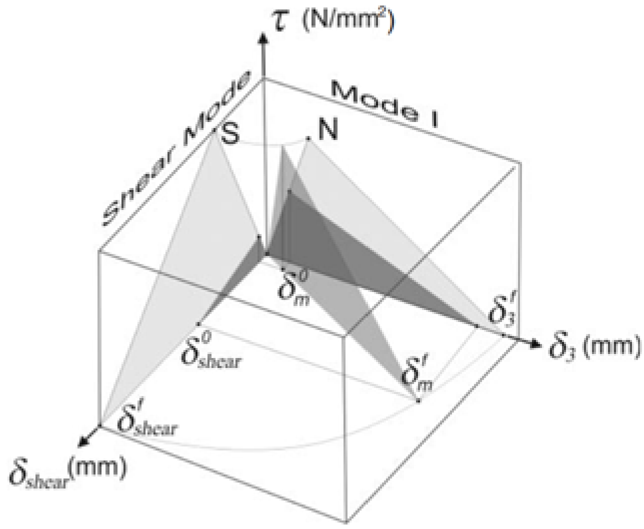

Figure 2.9: Traction-Separation law for mixed-mode loading conditions

In the above formulation by Camanho et al [5], the stiffness degradation followed a bilinear softening method. However, ABAQUS offers other damage evolution models such as exponential softening where the damage variable is computed as an exponential function of the relative displacements. Furthermore, ABAQUS also allows specifying the relative displacements and the corresponding damage variable in a tabular form for a given mode-mix ratio.

Despite the advantages of the cohesive element method over VCCT, researchers have identified some drawbacks and proposed potential solutions. Turon et al [6] noted that the cohesive state is reinstated when the mixed-mode ratio changes during delamination propagation. Figure 2.10 displays this phenomenon, where the mixed-mode ratio in the initial loading case is denoted as "A," resulting in complete failure due to effective displacement. However, for loading mode "B," the corresponding mixed-mode fracture energy is larger, causing a larger relative displacement and complete failure. Therefore, the relative displacement signified complete failure in mode "A" now only indicates a damaged state in mode "B".

The authors proposed a damage initiation criterion based on the BK damage propagation criteria. This ensures that the evolution of damage is consistent with thermodynamic principles when the loading conditions change during damage propagation.

$$\left(\tau^0\right)^2 = \left(\tau_3^0\right)^2 + \left(\left(\tau_{shear}^0\right)^2 - \left(\tau_3^0\right)^2\right) B^\eta \tag{2.27}$$

In a subsequent study, the authors found that the interfacial shear strength impacts the global response of specimens under mixed-mode loading conditions. However, pure-mode delaminations are not affected by interlaminar strengths [29]. In a simulation of the mixed-mode bending test, varying interlaminar shear strength resulted in inaccurate energy dissipation at a particular integration point ahead of the crack tip. The local mixed mode ratio also varied with changes in relative displacement at the integration points. This was a consequence of the damage initiation and propagation criterion being a function of the mixed-mode ratio. Variations in the mixed-mode ratios during damage growth altered the strength and fracture energy. Therefore, it was necessary to ensure that the rate of change of the damage variable remained non-negative. The authors proposed a closed-form relation between interlaminar strengths and the corresponding fracture energies shown in Equation 2.28. Subsequent simulations of experiments, where highly mixed mode conditions are required for damage propagation, revealed that the relation in Equation 2.28 can significantly reduce the effect of interlaminar strengths. The global response of these experiments also correlated well with solutions obtained from LEFM.

$$\tau_{sh}^0 = \tau_3^0 \sqrt{\frac{G_{IIc}}{G_{Ic}}} \tag{2.28}$$

Another issue with cohesive elements is the requirement of extremely fine mesh near the process zone of a crack. One solution was proposed in [30]. The cohesive zone length of a material is determined by,

$$l_{cz} = ME\frac{G_c}{(\tau^\circ)^2} \tag{2.29}$$

Where E denotes the material's Young's modulus, G_c is the fracture energy of the material and τ° is the interlaminar strength of the material. M is a cohesive zone model-dependent parameter which is often equal to 0.88 [30]. It can be observed that the cohesive zone length has an inverse quadratic relation with the interlaminar strength. For simulations, where a strong dependency on fracture energy exists, the cohesive zone length can be numerically increased by decreasing the interlaminar strength. The strength can be determined using the following relation,

$$\begin{aligned} \tau^\circ &= \sqrt{M\frac{EG_c}{N_e l_e}} \\ l_{cz} &= N_e l_e \end{aligned} \tag{2.30}$$

Where N_e represents the number of desired elements in the process zone and l_e is the length of the element. The findings in [30] indicate that accurate results can be achieved in simulations using lower interlaminar strengths and coarse meshes. However, stress concentrations in the bulk elements near the crack tip could be inaccurate.

Extended Finite Element Method (XFEM)

It is clear from the descriptions of CZM and VCCT that modeling the cracks or discontinuities requires the mesh to conform to the crack geometry, which leads to a lack of mesh objectivity. This issue can be addressed by using the extended finite element method, where cracks are modeled by enriching the displacement field. This method originated from the partition-of-unity finite element method introduced by Melenk and Bubská in [31]. The method allows beforehand to include information about the displacement fields, such as displacement discontinuity. Moës and Belytschko further extended this approach by incorporating discontinuity in the displacement approximation and crack-tip asymptotic fields based on the partition of unity method [32]. Including the asymptotic stress field enables the modeling of crack tip singularities and the determination of stress intensity based on LEFM. This displacement field is enriched using a Heaviside enrichment function.

$$u = \sum_{i=1}^{N} N_I(x)[u_I + H(x)a_I \sum_{\alpha=I}^{4} F\alpha(x)b_I^{\alpha}] \tag{2.31}$$

The first term $N_I(x)$ is the shape function and u_I are the degrees of freedom. $H(x)$ is the Heaviside function used to represent the discontinuity across the crack surfaces and a_I consists of the enriched degrees of freedom. The third term $F_\alpha(x)$ is the crack tip function.

In the following work, the authors modified the method and included cohesive traction separation laws for crack surfaces [32]. In this method, the stress singularity at the crack tip vanishes as shown in the previous section. The element is enriched when the failure criterion is satisfied in an element. The separation of crack surfaces determines the level of damage which is a function of the fracture energy.

Another methodology in XFEM is the phantom node method which is derived from Hansbo's work [33]. In this method, the nodes of the enriched element and 'phantom' nodes are tied to each other before damage initiation. After damage initiation, the element is divided into two subelements by the crack releasing the tie between the phantom node and the original node, as shown in Figure 2.11. The integrating domain is reduced to the area from the original nodes up to the crack surface. The new cracked domains, annotated by Ω_p^- and Ω_p^+, are created. In ABAQUS, the level set function is used to determine the crack position and geometry. The level set function consists of two signed distance functions per node, where one function defines the plane normal to the crack plane and the other function defines the crack front [17]. Details regarding other developments related to XFEM is covered in the following section.

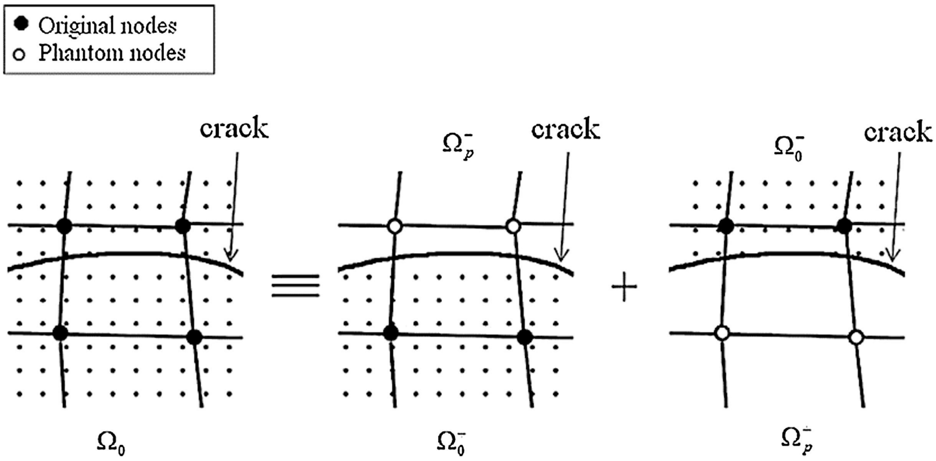

Figure 2.11: Treatment of cracks using Phantom Node Method [3]

2.2.3 Application of damage modeling techniques

The previous section dealt with the various methods that are used to model damage using FEM. It was discussed earlier that there are several types of damage in composite materials and it is essential to account for their interaction while modeling damage. Several efforts have been taken to validate the ability of the above modeling techniques to capture damage growth in the composite materials. However, utilizing only of the methods is insufficient to capture all the types of damage modes.

In [5], simulations of DCB, ENF, and MMB were carried out to validate the decohesion elements that were developed to model delamination. The results of the simulation correlated closely with experimental results and the error for mixed-mode delaminations was within 8%. In the subsequent work by Turon et al [6], where the damage initiation criterion was modified based on BK criterion, a simulation of skin-flange debonding was carried out. A skin and tapered flange model was created with decohesion elements placed at the interface with no pre-cracks in the model as shown in Figure 2.12.

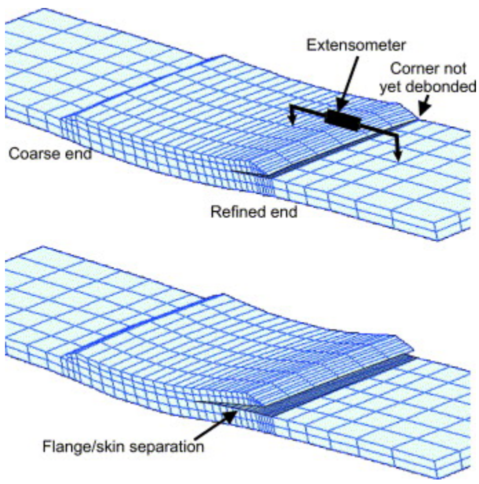

Figure 2.12: Skin Stiffener debonding simulation taken from [6]

Apart from delamination, cohesive elements have also been used to model matrix cracks in some cases. Pernice et al used interface elements, with cohesive traction separation behavior, at potential matrix crack sites in an OHT simulation in [2]. In Figure 2.13 the cohesive elements are aligned along the fiber direction in each ply since the matrix cracks run parallel to the fiber.

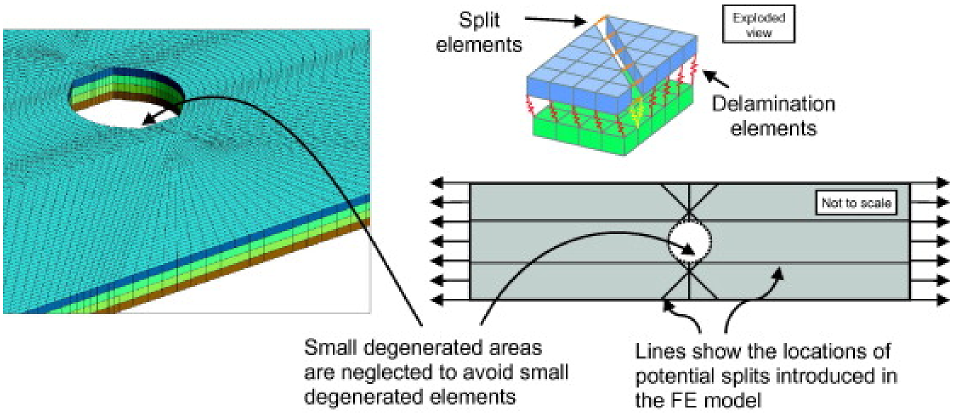

Figure 2.13: Interface elements used for matrix cracks and delaminations in [2]

The matrix cracks predicted by the interface elements can be seen in Figure 2.14. The simulation predicts the asymmetric ply splits in the 0° ply for the small holes and symmetric ply splits for the larger hole diameter. This result correlates well with the X-ray image obtained from the interrupted OHT tests. The authors also present results from simulations for ply-scaled and sub-laminate-scaled specimens to demonstrate the effect of the layup on the failure mode. The model was able to predict delamination-type failure for ply-scaled specimens where delamination propagates across the length of the coupon at the -45/0 interface. Additionally, the model also captured delamination being restricted in the sublaminate scaled specimen proving the capability of cohesive elements to model sufficient interaction between matrix cracks and delaminations.

However, in this study, the potential crack paths were determined based on experimental observations. This approach is not feasible for a general case where the crack paths are not predetermined. For such cases, CDM has been utilized to predict damage initiation and propagation. Furtado et al [24] developed a user material subroutine in ABAQUS based on the LaRC03-04 failure criterion to predict intralaminar damage while cohesive elements were used to model delamination. In-situ strengths were determined based on ply location and thickness in order to improve the accuracy of the prediction. In [34] Tijs et al modeled ply failure using CDM and delamination contact-based cohesive behavior in ABAQUS for virtual testing of OHT coupons and lap shear specimens. A high-fidelity model was developed, which consisted of the mesh in each ply aligned along the fiber direction. Shi et al [35] used CDM with cohesive elements to model the impact response of a cross-ply laminate. The CDM again implemented through a VUMAT in ABAQUS, showed a good correlation with experimental results at high energy impact load.

Although CDM combined with cohesive elements correlated well with experimental observations, whether this method can capture complex crack interactions is unclear. Meer argues in [22] that homogenization of material properties in mesoscale models affects the global re-

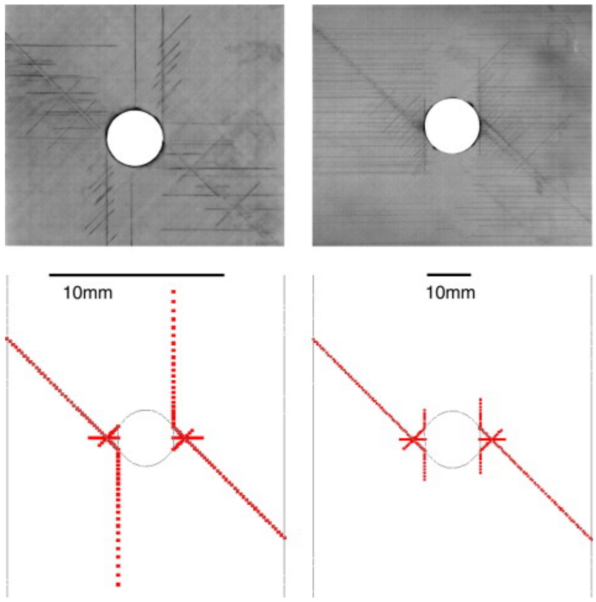

Figure 2.14: Matrix cracks in OHT predicted by interface elements [2]

sponse of a model despite the correct local response. The author cites one of his previous works where a 10° ply under tension was simulated using CDM to predict the in-plane shear strength. The simulation predicted the location of damage initiation in the ply, however, the crack propagation direction and global response did not correlate with experimental observation. The crack propagated transverse to the ply direction, resulting in unrealistic transverse displacement. This was due to the inherent characteristic of the CDM method where the crack propagation direction is only predicted based on stress concentration. This error can be alleviated if the mesh is aligned along the fiber direction as done in [34].

In [36], the size effect of translaminar fracture energy on open-hole tensile strength using CDM and CZM was studied. First the importance of modeling delamination to accurately predict the strength of a notched laminate was emphasized. It was shown that using shell elements such as S4R in ABAQUS to represent the entire laminate might lead to overprediction of the notched strength since the failure mechanism consists of significant delaminations. Modeling each ply using continuum shell elements and a cohesive interface resulted in a mesh-objective outcome and good correlation with experimental observations. The simulations conducted to study the behavior of ply-scaled and sublimate-scaled specimens also displayed excellent correlation with experimental results. However, the simulation results of in-plane scaling for ply-scaled specimens deviated from experiments. The ply-scaled specimens with in-plane scaling predominantly fail in the pull-out mode, characterized by significant delaminations before the zero-degree plies fail. The author attributes this error to the CDM model's inability to accurately represent the stress concentration at the matrix crack tip that induces delamination. Cracks predicted by the CDM are smeared over the volume of the element, preventing the model from capturing the stress concentration at the matrix crack tip. This can be achieved to a certain extent by discrete representation of matrix cracks in the element.

XFEM has been widely used by many researchers to model matrix cracks in a discrete manner. van Dongen et al [7] proposed and tested a blended approach where XFEM was used to

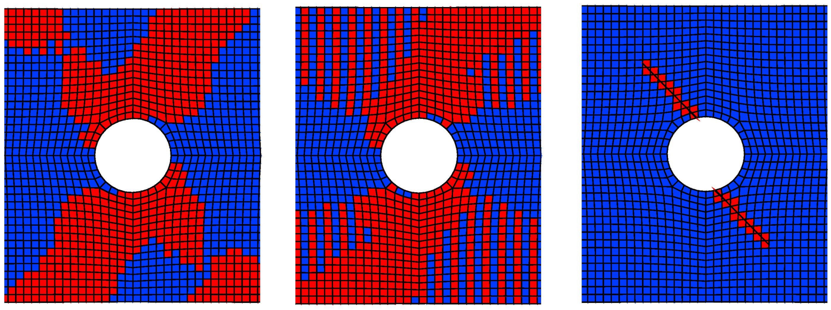

(a) DM1 (b) DM2 (c) DM3

Figure 2.15: Matrix cracking in $45°$ using three approaces [7]

determine matrix cracks, cohesive elements for delamination, and CDM for fiber failure. The approach was used in a numerical simulation of OHT and the results were validated using experimental results. Two other numerical approaches were also carried out for comparison: one solely used CDM for ply failures with no delamination and the second used CDM along with cohesive elements at ply interfaces. Figure 2.15 shows the failure patterns predicted by the three approaches in a $45°$ ply in the numerical model of the OHT specimen. DM1 and DM2 show the matrix crack predicted by the CDM subroutines while DM3 shows the discrete crack modelled using XFEM. The XFEM crack grows parallel to the fiber direction. The author points out that the limitation of the XFEM implementation in ABAQUS does not allow for predicting secondary matrix cracks that are observed in experiments. Nevertheless, the accuracy of the failure pattern achieved is better for the XFEM model. This is also justified by the strain contour plots compared with the DIC result presented in [7].

Wang et al [8] used the cohesive segments-based XFEM to model matrix cracks while accounting for matrix plasticity and hydrostatic sensitivity of the yield stress. The matrix crack was predicted using the LaRC05 criterion using a user damage initiation subroutine (UDMGINI). The LaRC05 criterion allows the determination of the fracture plane, however, the orientation of the plane needs to be numerically determined. The authors developed a modified Golden Section search algorithm, abbreviated as CLGSS, to find the orientation that maximizes the failure criterion. The search algorithm was used to predict the failure envelope for the composite material subjected to transverse and shear stresses. The strength predictions from the literature were comparable to the failure envelope obtained using the above approach as seen in Figure 2.16. The authors simulated the Iosepescu tests, which were validated using the experimental results. This study indicates that an accurate response of composite materials can be obtained using XFEM when shear non-linearity is also included in the constitutive model. Although only unidirectional laminates were tested, the authors conclude that the above approach can be used in matrix failure in multidirectional composite laminates.

In [9], the modified Selection Range Golden Section Search (SRGSS) algorithm was used to determine the matrix crack orientation using the Puck failure criterion. XFEM was used to model matrix cracks in bulk elements as well as the failure of the resin-rich ply interfaces. The interface elements were also enriched using XFEM in ABAQUS, however, the crack orientation was controlled using the UDMGINI criterion. The matrix crack orientation determined using the modified SRGSS algorithm was passed on to the UDMGINI subroutine to model the

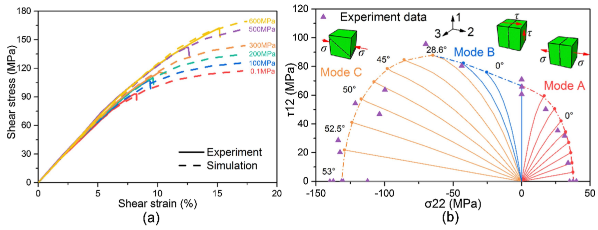

Figure 2.16: Shear response and failure envelope [8]

matrix crack in the bulk elements of the ply. The algorithm and the subroutine were first tested in a DCB simulation and the results obtained closely aligned with a simulation that used cohesive elements. A simulation of a cross-ply laminate under impact loading was carried out. In the experiments, a crack was initiated in the 90° ply block approximately 20mm from the impact location after which it propagated to the adjacent 90/0 interface resulting in a delamination. The simulation predicted the location of crack initiation, propagation towards the interface, and the subsequent delamination as seen in Figure 2.17.

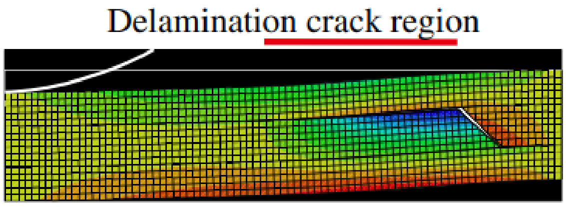

Figure 2.17: Crack propagation under impact load [9]

A similar approach can be noticed in the work by Zhao et al [10]. XFEM was used to simulate delamination and matrix cracks in unidirectional and cross-ply laminates using ABAQUS. A crack-leading algorithm was implemented in a damage initiation subroutine (UDMGINI) to predict the onset and orientation of the crack. The algorithm ensures the XFEM crack runs parallel to the fiber direction at the 0/0 interface. At the 0/90 interface, the crack propagates as a delamination between the plies when the principal stress orientation in the interface, θ is less than 90° as seen in Figure 2.18. When the principal stress orientation is greater than 90° the crack is allowed to kink into the 90° plies if it satisfies the failure criterion. The authors employed this method in a 2D simulation using plane strain elements. The algorithm was successful in predicting the migration of the crack into the transverse plies at a location very close to that observed in experiments Figure 2.19.

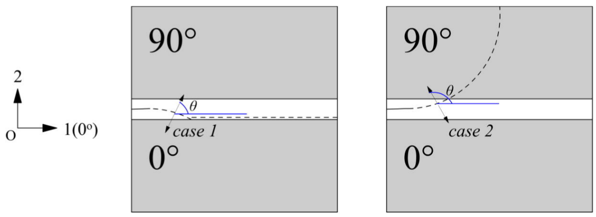

Figure 2.18: Crack propagation in multi-direction laminates [10]

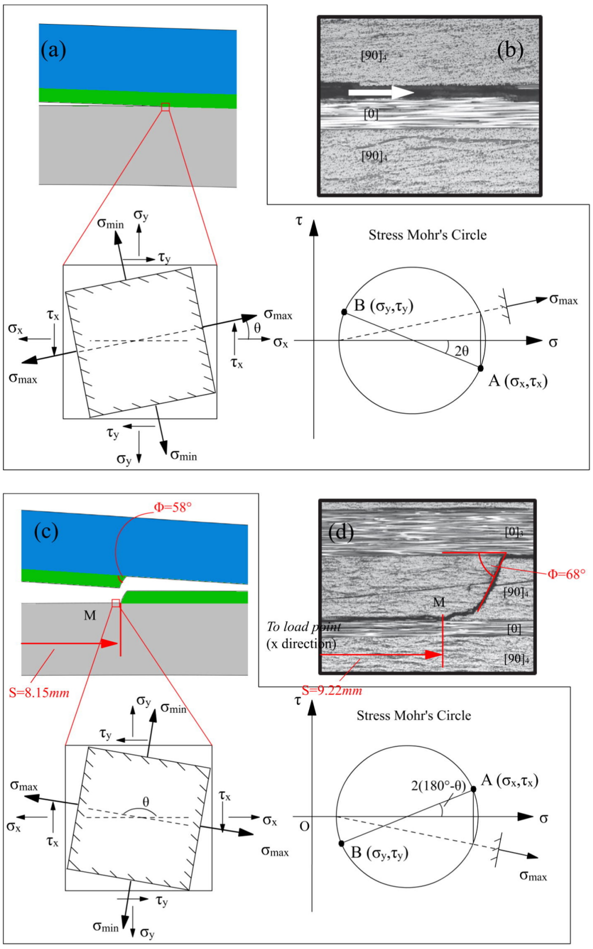

Figure 2.19: Crack migration predicted by crack leading algorithm [10]

In the above studies, XFEM has not only been used to capture delamination and matrix cracking but also their interaction. This is achieved by enriching solid elements that are positioned at ply interfaces to allow crack propagation beyond the boundaries of the ply elements. However, this approach only allows modeling the initiation and propagation of a single crack. It may often be necessary to capture the effects of secondary cracks in the material for a more accurate representation of the failure process. Given the limitation that only a single crack can propagate in an enriched region in ABAQUS, dealing with multiple cracks can be non-trivial. Petrov et al defined multiple enriched regions in a cross-ply laminate to study the capability of XFEM to capture matrix cracking under transverse tensile loading [37]. In this study, a statistical distribution of the transverse strength was used across the domain to allow crack initiating at the weakest enriched region. Additionally, the sensitivity of element size, enrichment spacing, strength, and fracture energy were studied. The influence of delamination in the numerical model was also studied by using cohesive contact at the 90/0 interface. It was observed that allowing delamination in the numerical simulation resulted in lower crack density at the same applied strain. However, at low strains, the difference in crack density was only 10% which may seem insignificant. However, the authors claim that reducing the fracture energy of the cohesive interface might show a significant difference in the crack density. Nevertheless, the slowing down of transverse cracks due to delamination and the subsequent increase in transverse strength can be obtained by modeling a cohesive interface in the numerical model.

The combined approach of XFEM and cohesive elements to model transverse cracks and delaminations was also used to study the in-situ effects on transverse strength in cross-ply laminates. [38]. The authors demonstrated that a fine mesh through the thickness of the 90° ply can predict the in-situ strength of thick and thin plies without including cohesive elements. In the analysis of composite laminates, it is not always practical to have a fine discretization in the thickness direction. A single row of elements can be used for the transverse ply only if delamination is allowed in the model. Thus, a single row of elements along with a cohesive interface accurately predicted the in-situ effect for thin plies while the results deviated for thick plies. This is because thick-ply in-situ strength depends on the crack propagation through the thickness which requires finer resolution in the thickness direction. However, this study concluded that the combined approach of XFEM and cohesive elements can be used reliably for the damage modeling of composite laminates especially for thin plies. This was also justified by the crack density predictions obtained from the XFEM-cohesive interface models. The crack-density saturation observed in experiments was over-predicted by 30% which is attributed to the choice of the cohesive parameters.

In the case of composites under out-of-plane loading conditions, such as impact or crack-migration test, the authors in [10] and [9] avoided the use of cohesive elements at ply interfaces. The objective of employing a damage initiation subroutine was to capture the energetically favorable conditions that drive a crack to propagate in the direction perpendicular to the principal stress. Zhao et al point out that traditional cohesive elements are incapable of capturing the displacement discontinuity that arises in the adjacent solid elements without modifying the cohesive element formulation. Fang et al developed an augmented cohesive element (A-CE) using the phantom node method as a solution to this shortcoming [11]. The A-CEs are used in combination with augmented finite elements (A-FE). The displacement field of the A-FEs is augmented to represent displacement discontinuity. 'Ghost nodes' are connected to the original nodes of the element before the damage initiation. When the damage initiates, the elements split into two mathematical elements (ME), as depicted in Figure 2.20. The displacement field is described using two sets of original nodes and two sets of ghost nodes. The stiffness matrix for these elements is determined using a subdomain integration scheme similar to the PNM. When a crack within one of the A-FEs reaches the A-CE's edge, the A-CEs are augmented and split into two MEs. After the splitting, the A-CEs are treated the same as a standard cohesive element. The A-CE integration is carried out at two Gaussian points within the sub-element.

The element integration performed over the sub-domain in the phantom node method could result in erroneous results. The floating node method overcomes this issue as shown in [39]. In the PNM, the phantom nodes and real nodes share the same nodal coordinates during the analysis until a discontinuity allows them to separate. However, the floating nodes in FNM are not tied to standard finite element nodes that is they do not share the same nodal coordinates as the real nodes. When a discontinuity arises in the displacement field, the floating nodes are assigned to a geometrical entity of the element. In two-dimensional cases, the floating node is assigned to an edge, and in three dimensions, it may be a surface or an edge. The coordinates of the crack nodes are determined from a failure criterion. Once the floating nodes are assigned to a geometrical entity, the new element consists of a set of original nodes and a set of new nodes with the crack coordinates. Unlike PNM, a new Jacobian matrix

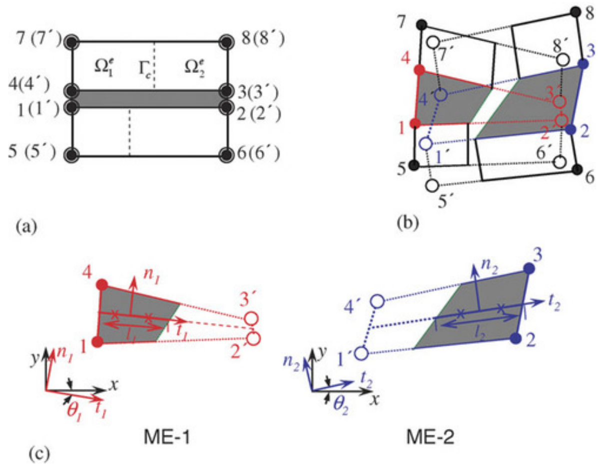

Figure 2.20: Augmenting the cohesive element [11]

and B-matrix are determined for the sub-element which results in a new set of integrands for the stiffness matrix. The integration domain is obtained by transforming the entire sub-element into the isoparametric space and the crack surface is also accurately represented after transformation. However, PNM uses the same isoparametric space for the element before and after the initiation of a discontinuity requiring the use of subdomain integration. Cohesive cracks can be represented using the floating node method. The constitutive traction-separation law can be applied using the nodal displacements that are present on the crack face of the two subelements. For further details regarding the implementation of the above method and comparison of FNM with PNM, XFEM, or remeshing, the reader is referred to [39].

The FNM was used to model crack migration in cross-ply laminates by combining the technique with VCCT to determine crack propagation [40]. The crack migration simulations were carried out in 2D using plane strain formulation. The method was able to predict the crack migration location and the global response accurately for various load cases. In [12] the capability of including cohesive cracks at arbitrary locations using FNM was used to construct three-dimensional laminate elements. The sub-elements represent the different plies and the resin-rich interlaminar regions. The interlaminar regions are treated like standard cohesive elements when the adjacent ply element does not contain any matrix cracks. In the presence of matrix cracks, the edges of the cohesive element are assigned floating nodes and the element splits into two as shown in Figure 2.21. This methodology was used to model crack migration in the angle ply laminates in [12]. Quadratic stress criterion was used to predict delamination and matrix cracking. The model predicted crack kinking and migrations at different locations across the laminate width as observed in the experiments from [2]. The matrix cracks were modeled vertically through the 90° which might be the reason behind the over-prediction of the peak load in one of the load cases. The author also demonstrates that using standard cohesive elements in the simulation failed to predict crack migration. However, the quadratic failure criterion used for matrix cracks does not model inclined matrix cracks observed in the experiments. The orientation of the matrix crack is essential to capture accurate energy dissipation. It could be possible that nucleation of inclined matrix cracks could result in an energetically favorable path and thus result in migration despite the use of standard cohesive

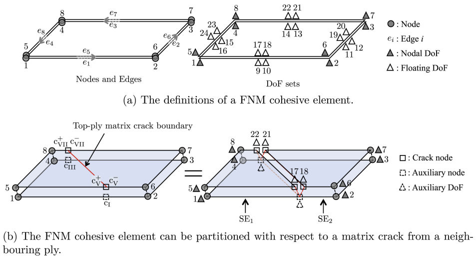

(a) The definitions of a FNM cohesive element.

(b) The FNM cohesive element can be partitioned with respect to a matrix crack from a neighbouring ply.

Figure 2.21: Cohesive Element split by floating nodes [12]

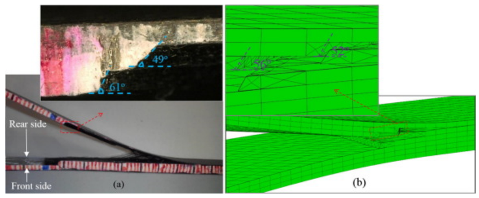

Figure 2.22: Crack migration in DCB specimen [13]

elements.

Other approaches also include modeling the interaction of matrix cracks and delamination by enriching cohesive elements with enrichment functions [41][13]. Hu et al enriched 3D elements using a shift-basis enrichment method. The method was also applied to enrich the displacement fields for the cohesive elements. This allowed the cohesive elements to capture the displacement discontinuity in the abutting solid elements. Additionally, the authors employed a zig-zag cohesive law to improve the convergence of the simulation. The method was used to simulate the DCB of a multidirectional composite laminate. Crack migrations observed in experiments were also predicted by the model as seen in Figure 2.22. This study utilized the 3D Hashin failure criterion to model inclined matrix cracks. However, the results indicate slight deviations in the force response predictions when validated against experimental data.

Enriching cohesive elements in commercial finite element packages like ABAQUS requires the development of user elements subroutines which must undergo extensive validation before it can be applied to structural simulations. However, Van der Meer demonstrated that when solid elements are enriched using the phantom node method, using cohesive elements without any modifications can be acceptable [22]. The author states that the displacement inaccuracies in the cohesive elements when a ply element cracks are often limited to the element's interior region. Using unadapted interface elements can be accepted since sub-element level accuracy is not usually sought after and the errors may be minimized upon mesh refinement. Since the relative displacement of the phantom nodes represents the displacement of the actual material points, this information is often available at the cohesive element nodes as well. Therefore, using nodal integration for cohesive elements can ensure a better approximation than Gaussian integration schemes. However, the author demonstrated the interaction between matrix cracks and delamination in a composite laminate subjected to in-plane loading conditions. The capability of this method to predict stronger interactions such as crack migration could require further investigation.

XFEM and CZM have been used to model matrix cracking and delamination without any modifications to the formulations available in ABAQUS. Baran et al used the XFEM-CZM method in ABAQUS to model the crack initiation and propagation in the thermoplastic butt-joint section subjected to a three-point bending test [42]. A cohesive surface was used to predict delamination at the interface of the laminate and the filler material as shown in Figure 2.23. XFEM-VCCT technique which works based on the line elastic fracture mechanics method to predict crack propagation was used to model the brittle cracking of the thermoplastic filler material.

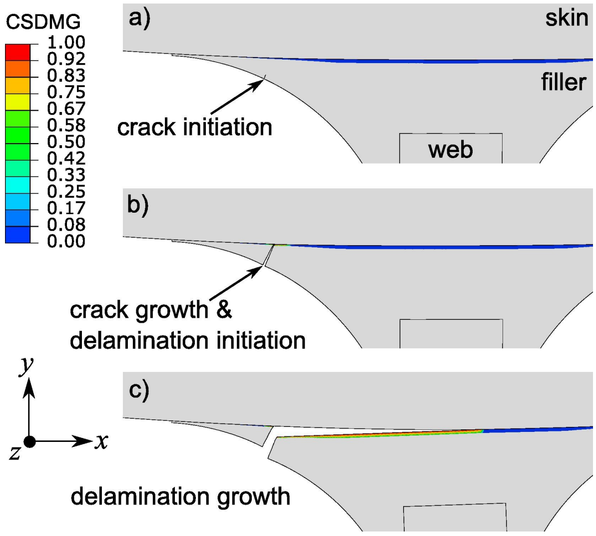

Figure 2.23: Delamination at butt-joint interface

Grogan et al used XFEM to model micro-cracking in the matrix and surface-based cohesive behavior for delamination [43]. The authors aimed to predict the formation of crack networks that will result in gas leakage in composite structures operating in cryogenic conditions. The FE model accounted for defects and statistical distribution of strength across the laminate to obtain a more realistic prediction from the simulation. XFEM was used for transversal intra-laminar cracks, and surface-based CZM was used for the interaction between adjacent plies and cracks using pre-defined delamination surfaces. The model also accounts for the size effect, where a larger element has a higher probability of failure than a smaller element. Permeability is predicted based on overlapping areas between cracks in adjacent plies and crack displacements. The numerical results reveal delaminations near matrix crack tips. The orientation of the matrix crack is vertical within the ply. The cracks formed in the model are used to quantify the permeability of the laminate. The results predicted by the numerical model are compared with experimental data and show reasonable agreement.

2.3 Skin-stiffener Failure and Simulations

The studies presented so far demonstrated the capability of using computational fracture mechanics techniques to predict complex failure mechanisms observed in composite laminate at a coupon or sub-structural level. It has been observed that to accurately predict damage interactions, the resolution of the stress states in a composite laminate needs to be sufficiently high which usually requires a meso-scale model of the composite laminate. However, finite element models of aeronautical structures use low-fidelity modeling techniques to predict structural response. The mesoscale modeling approach to a composite structure would require extremely high computational power. Moreover, damage simulations introduce an additional layer of complexity through material non-linearity which adds to convergence difficulties if the Newton-Raphson method is used as a solution approach. With the growing demand for damage-tolerant structures, performing damage simulations on such large geometries has become vital to minimize the number of experimental campaigns. Nevertheless, efforts have

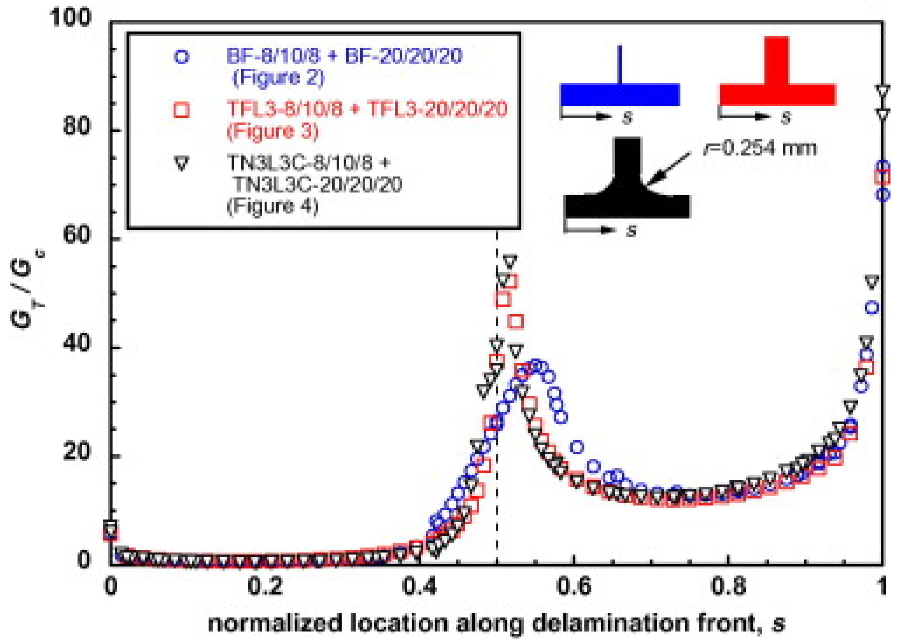

Figure 2.24: Comparison between the three levels of local high-fidelity models [14]

been made to develop and test structural modeling techniques that can take advantage of low-fidelity methods while utilizing the advanced damage modeling techniques presented in the previous section. Following are some examples where damage simulations are carried out on skin-stiffener structures.

Krueger et al used VCCT to predict skin-stiffener separation in a T-stiffened panel subjected to shear loads [14]. The simulations used a global local approach to verify if the accuracy of failure prediction improves with increasing the model fidelity. The global model of the stiffened panel was discretized using shell elements in ABAQUS whereas the local high-fidelity model consisted of various approaches. In the baseline case, the skin and stiffener foot were meshed using solid elements. Two following cases were analyzed - one where the web was also modeled using 3D brick elements per ply and the second where the stiffener transition and noodle region were meshed using 3D elements. Shell-to-solid coupling was used to connect the solid regions to the shell regions in ABAQUS. Further mesh refinement was done for the skin and stiffener foot near the locations where failure was expected. Further details of this can be found in the cited reference. The objective of the simulation was to assess the influence of fidelity on the damage onset prediction. VCCT equations were used to determine the total energy release rate (G_T) at the nodes near the crack front while the critical energy release rate (G_C) was determined using the BK criterion. Damage onset was predicted if the ratio of G_T/G_C was greater than 1. This failure index was plotted for the three modeling approaches with the normalized distance along the stiffener foot in the x-axis, Figure 2.24. The results indicate a significant difference in the failure index predicted. The authors attribute this to the difference in local stiffness arising from local mesh refinement and solid elements used in these sections. Although there is no test data supporting the simulation results, this work highlights the local high-fidelity models of simulation results and claims that the accuracy of simulations could be improved using such modeling techniques.

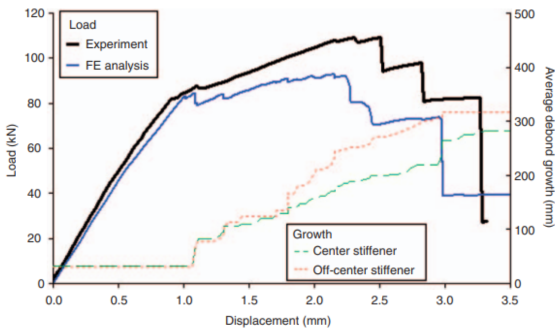

Figure 2.25: Comparison of the load-displacement by FE with experimental response [15]

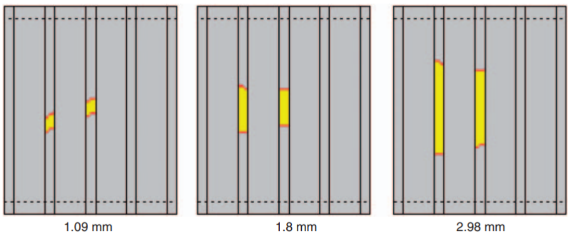

Figure 2.26: Skin-stiffener separation predicted by VCCT [15]

Orifici et al carried out simulations on damaged and undamaged multi-stringer panels to predict damage initiation and growth [15]. For the intact blade-stiffened panels, a global-local approach was used to identify the critical section using the degenerate Tsai interlaminar failure criterion. In the global-local methodology, the global displacements were transferred from the shell model to the local 3D model. The Hashin damage criterion was used to predict damage onset in the plies and the property degradation method was used for progressive damage analysis. In the case of the damaged panel, VCCT was used to model debond propagation at the skin-stiffener interface using the user-defined MPC. The VCCT was modified to obtain a better approximation of the energy release rates. For testing, the damage in the manufactured panel was introduced through cyclic displacement controlled loading which corresponded to 95% of the collapse load. The damaged panel was loaded statically until complete failure. FE simulations closely predicted the failure process although the peak load deviated from experiments as seen in Figure 2.25. Apart from the debond growth, shown in Figure 2.26, matrix, and fiber damage were also predicted in the panel. Matrix crack was mostly present in the outer 90° ply of the skin close to the debond crack front. Fiber failure was first predicted in the outer blade stiffeners of the panel which led to a load drop by 10kN while the fiber failure in the 0° ply in the central stiffener resulted in the load dropping by 30kN. The final fiber failure was preceded by the debond growth and matrix cracking.

Numerical simulations of two single stiffener carbon-expoy composite panels with different geometries and skin-stiffener debond areas were conducted using a modified VCCT technique (SMXB-SS) by Raimondo et al in [16]. Experiments were conducted until failure, in this case, skin-stiffener separation. For intra-laminar damage, the instantaneous damage model was implemented in a user material subroutine (USERMAT), where the elastic properties of the constituents were degraded by a certain factor. The Hashin failure criterion was used to determine the onset of damage and the stiffness degradation was done when the criterion was

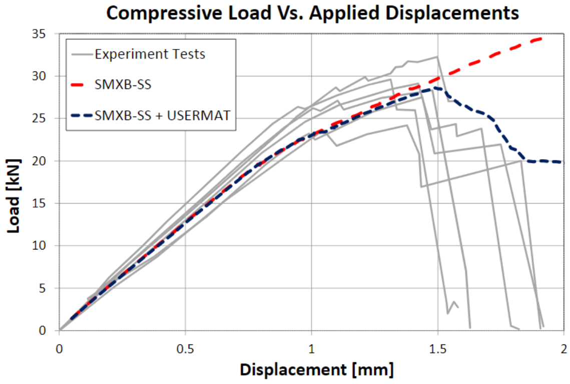

Figure 2.27: Influence of material damage in the constitutive model on the response of skin-stiffener [16]

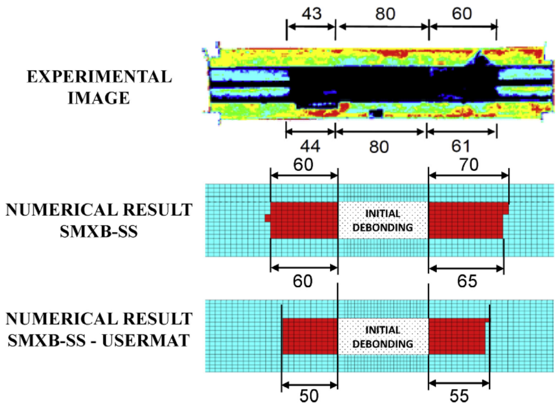

Figure 2.28: Difference in prediction of debond area [16]

satisfied. Two simulations were carried out for both configurations of the panel. The first simulation only modeled the debonding at the stiffener foot while the second included the material degradation model in the stiffener. The plot in Figure 2.27 shows that accounting for material damage in the stringer results in the stiffness drop in the global response. Since the material softening approach did not use any physically based method like CDM, the load drop was not captured. However, the debonded area predicted by the model which accounted for material degradation in the stiffener was smaller than the debonded area determined by the model which only used VCCT indicating the coupling between the different damage modes in the structure Figure 2.28.

Vescovini et al [44] used cohesive elements in a local model to predict debonding in a single-stiffener model. Shows how sub-modeling can yield pretty good results. Van Dooren et al [27] used VCCT to predict skin-stiffener separation and modeled the skin and stiffener using continuum shell elements. Good results were obtained although damage was restricted predominantly at the skin-stiffener interface. Meeks et al carried out experiments on skin-stiffener using the 7-point bending method. The authors reported matrix cracks in the outer ply which lead to the skin-stiffener separation [45]. Action et al implemented another global-local method to predict failure at the interface of the skin-stiffener in an omega-section stiffened panel [46]. CDM was used to predict ply failure in the local model and the elements were aligned along the fiber direction. Elements were selected to explicitly predict matrix cracks within the local section. Cohesive elements were used to model delamination. This model predicted the migration of cracks from the skin-stiffener interface to the ply interfaces within the skin.

Chapter 3

Methodology

3.1 Research Objective and Research Questions

Skin-stringer separation has been central to all the cited references presented in the previous section since the collapse of the structure was mostly a consequence of stable or unstable crack growth at this interface. This failure mode is highly researched and investigated when post-buckling of stiffened panels is considered [15]. Predicting damage in the vicinity of this interface would aid in the development of strategies to mitigate failure and improve structural performance. It has been observed that the skin-stiffener interface failure occurs due to stress concentrations arising at the interface as a consequence of differences in geometry as well as variations in bending properties. Imperfections and defects at this interface could compromise the integrity of the structure. At times damage in the outer ply of the skin or stringer has also resulted in significant differences in response of the structure. For instance, the experimental work by Meeks et al shows that the propagation of cracks at the skin-stiffener interface is influenced by matrix cracks in the outer ply of the skin [45]. Such observations and insight gained from previous studies call for approaches that can account for damage in the material surrounding the skin-stiffener interface.

In the context of numerical simulations, VCCT and CZM are commonly used to model the skin-stiffener separation. Various studies in the literature, including the references that have been cited, show that these methods can yield excellent correlations with experiments and are suitable for designing novel structures. Many studies account for damage in the skin and stiffener using ply degradation models or smeared crack methods like CDM. However, simulations at the coupon level show that using CDM with CZM can yield accurate results when there is almost no interaction between matrix cracks and delamination. When structural failure is preceded by delaminations at ply interfaces in the skin, it becomes necessary to include these damages in the numerical model to accurately predict the structural response. Such damage has been observed in the thermoplastic butt-joint skin-stiffener that was tested at TU Delft. C-scans of several single-stiffener panel specimens reveal delaminations at ply interfaces in the skin. Previously, the post-buckling of a multi-stringer panel manufactured using the thermoplastic butt-joint filler method was analyzed in [27] where the skin-stiffener separation was predicted using VCCT. Since the new single stiffener panel reveals additional damage in the structure, the numerical simulations need to account for intralaminar and interlaminar damage in the skin. This leads to the research objective of this thesis:

> *"Predict the delamination, skin-stiffener interface failure, and matrix cracks in a finite element model of the thermoplastic butt-joint single stiffener panel subjected to out-of-plane deformations using computational fracture mechanics methods"*

CZM has been the most common method used to model delamination in composite laminates. The combination of this technique with the extended finite element method (XFEM) has the capability of capturing the interaction of matrix crack with delamination. The coupled XFEM-CE approach has extensively been applied to simulate crack interactions at a coupon level. A similar approach to model progressive damage in composite stiffened panels has not been found in the literature. This provides an opportunity to explore the capabilities of this method to predict damage that would arise in a composite stiffened panel and document the advantages or shortcomings of this technique. To do this, the following research question has been formulated:

> *"How effectively can XFEM and cohesive elements capture the interactions of damage in a composite stiffened panel?"*

To effectively answer this research question, additional sub-questions have been formulated. First, a hypothesis is formulated based on the insight gained from the literature regarding the damage that is observed in the thermoplastic butt-joint

> *"The delamination observed in the ply interfaces of the skin in the thermoplastic butt-joint single stiffener panel is a result of the matrix cracks in the outer ply caused by stress concentrations at the crack front of the artificial defect"*

Based on this hypothesis, the Extended Finite Element Method (XFEM) has been selected for the discrete modeling of matrix cracks within the ply, necessitating a robust and accurate damage initiation criterion. A review of the latest version of ABAQUS revealed the implementation of the LaRC05 failure criterion. This criterion is compatible with three-dimensional elements and operates within the XFEM-cohesive segments framework. Notably, the LaRC05 criterion also enables numerical predictions of the orientation of matrix cracks. In light of these advancements, the following sub-questions have been formulated to guide the research:

1. How effective can matrix crack determined by LaRC05 be in predicting the interaction of matrix crack and delamination?

2. How accurate is this combination of XFEM with standard cohesive elements in predicting the interaction of matrix cracks and delamination?

3. How do numerical parameters influence the interaction of matrix cracks and delamination?

4. How do material parameters influence the interaction of matrix cracks and delamination?

5. To what extent does accounting for a discrete matrix crack and interlaminar failure in the skin influence the response of the stiffened panel?

Having established the questions necessary to evaluate the effectiveness of the XFEM-Cohesive Zone Model (CZM) in capturing damage interaction in the stiffened panel, the subsequent section outlines the methodological steps undertaken in this thesis to achieve the research objectives.

3.2 Research Plan

As stated in the hypothesis, the delaminations observed within the skin could result from the artificial crack migrating from the skin-stiffener interface through the matrix cracks in the outer ply of the skin. However, it is essential to verify whether the chosen numerical method, XFEM-CE, can accurately capture these crack interactions.

To accomplish this verification, simulations of the crack migration test described by Ratcliffe et al [1]. will be conducted. This test has been widely utilized in the literature to evaluate various methods developed for modeling the interaction between matrix cracks and delaminations in composite laminates. Although some studies suggest that standard cohesive elements may be ineffective in accurately capturing crack migration, this thesis must work within the limitations of the ABAQUS package.

Conducting this simulation will serve a dual purpose. First, it will help assess the capability of the XFEM-CE approach in predicting crack interactions. Second, it will verify whether the LaRC05 failure criterion can accurately predict the orientation of cracks as observed in experimental settings, thereby minimizing potential errors associated with the use of standard cohesive elements. Successful validation of these aspects will facilitate the answer to the first research question.

The second research question will be addressed by validating the results of the crack migration test simulations against experimental data and findings from existing literature. By comparing the simulation outcomes, particularly those obtained through the XFEM-CE approach in ABAQUS, with empirical results, a robust correlation can be established. Successful validation will further support the hypothesis that the XFEM-CE approach is capable of accurately capturing the intricate interactions between matrix cracks and delaminations.

To assess the influence of numerical and material parameters on crack migration predictions, a comprehensive approach will be employed involving mesh convergence studies and parametric analyses. The insights gained from these simulations will directly contribute to addressing the third and fourth research questions. These findings will serve as essential inputs for modeling crack propagation at a structural level. Specifically, a three-point bending model of the thermoplastic butt-joint skin-stringer will be developed, featuring an initial artificial crack that will be progressively extended during the loading process. By utilizing the XFEM-CE approach, we aim to investigate whether crack migration occurs within the panel under loading conditions.

The outcomes from this simulation will be contrasted with results from a separate simulation that does not incorporate XFEM. A noticeable absence of delamination within the skin in the latter scenario could provide compelling evidence that the matrix crack interactions and delamination are effectively captured by the proposed XFEM-CE methodology.

Chapter 4

Crack Migration Test - Modeling

The crack migration test, introduced in Chapter 2, serves as a crucial methodology for investigating the propensity of delamination to kink into adjacent off-axis plies, ultimately leading to matrix cracking and the formation of new delaminations at subsequent ply interfaces. Experiments conducted by Ratcliffe et al. [1] on cross-ply laminates and further studies by Pernice et al [2] on angle-ply laminates at angles of 60° and 75° have been instrumental in understanding this phenomenon. The primary objective of these tests is to identify the conditions that facilitate crack migration within composite laminates.

In this chapter, the approach taken to develop the numerical model for the cross-ply test specimen is presented. The selection of a cross-ply configuration is particularly relevant, as it is expected to exhibit only a single migration event. In contrast, laminates oriented at 60° or 75° are prone to multiple migration events due to the variation of stress across the width of the laminate. This focused investigation into a single migration event simplifies the analysis and allows for a clearer understanding of the mechanisms at play.

4.1 Finite Element Model Description

4.2 Test Specimen

The test specimen is a cross-ply laminate with a pre-crack between a zero-degree ply and a stack of 90° plies. Calmped at both ends, the laminate is loaded in the out-of-plane direction at a distance L from the clamping surface as shown in Figure 4.1. The width of the laminate is 12.7mm and the length of the specimen between the clamps is 115mm. The load is introduced through a piano hinge on the upper sub-laminate. The layup of the specimen is $[90_4/0_3/(90/0)_{2s}/0_3/90_4/T/90_4/0/0/(90/0)_{2s}/0/0/90_3/0/90]$ where the ply at the extreme right in the stacking sequence is the lowest ply of the laminate.

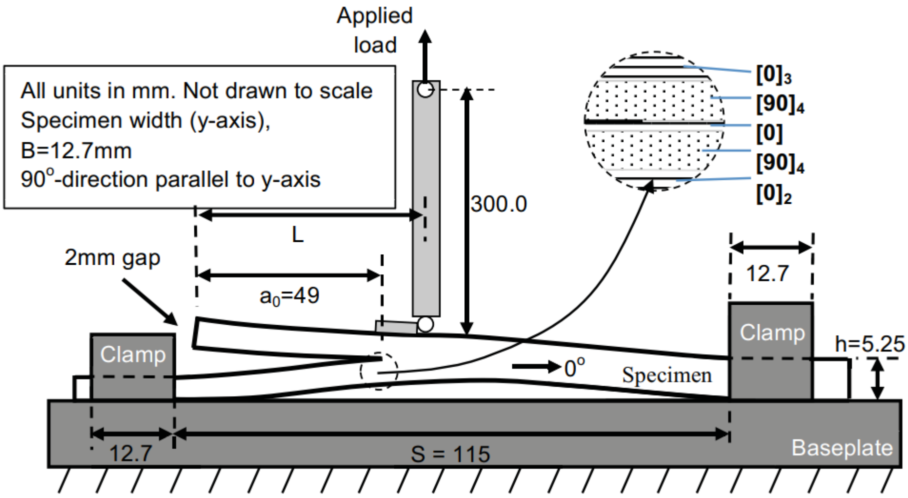

Figure 4.1: Crack Migration Test set-up

4.3 Modeling Approach

A mesoscale model is required to capture the sequence of damage and failure in the composite laminate. Since the damage propagates within the 90/0 interface and through the 90° ply block the stack of 90_4 and the 0° plies present above and below the 90° ply block respectively are modeled separately. These parts are meshed using hexahedral full integration elements (C3D8) with a single row of elements per ply. The plies in the top-sublaminate, consisting of $[90_4/0_3/(90/0)_{2s}]$, and the bottom sub-laminate consisting of $[0/(90/0)_{2s}/0/0/90_3/0/90]$ are modeled as two separate parts. The top and bottom sublaminate parts were discretized using solid elements and the stacking sequence was specified using the Composite Layup option [12].

Two additional parts were created for the cohesive interface and were meshed using the standard 8-node linear cohesive elements (COH3D8) in ABAQUS. A viscosity of 1e-6 was specified for these elements. The cohesive elements were placed between the $0/90_4$ and $90_4/0_3$ interfaces. The cohesive elements in the top 90/0 interface spanned the whole length while the bottom interface was shorter by 49mm due to the presence of the pre-crack. No cohesive elements were placed in the region of the pre-crack. All the parts were stacked in the assembly module and tie constraints were defined between the connected parts.

4.4 Material Properties and Failure Criterion

The test specimen was manufactured using IM7/8552 carbon-epoxy tapes in [1]. The material properties employed in the numerical simulation presented in [12] are adopted here. The material properties are specified in the following table Table 4.1, Table 4.3, and Table 4.2.

Property	Value	Units
E1	161	GPa
E2	11.38	GPa
E3	11.38	GPa
G12	5.17	GPa
G13	5.17	GPa
G23	3.98	GPa
μ_{12}	0.32	-
μ_{13}	0.32	-
μ_{23}	0.44	-

Table 4.1: Elastic Properties of IM7/8552

Table 4.2: Interlaminar Strength and Fracture Energies

Property	Value	Units
S_n	60	MPa
S_s	90	MPa
K_n, K_s	1.6x10^5	N/mm^3
G_{IC}	0.21	kJ/m^2
G_{IIC}	0.77	kJ/m^2

Table 4.3: Matrix Strength and Fracture Energies

Property	Value	Units
Y_t	60	MPa
S	90	MPa
G_{IC}	0.21	kJ/m^2
G_{IIC}	0.77	kJ/m^2

The LaRC05 failure criterion is ABAQUS is used in the current study to determine the damage initiation in the ply. The LaRC05 failure criterion accounts for four damage initiation mechanisms - Matrix Cracking, Fiber tension, Fiber Kinking, and Fiber splitting [17]. Fiber kinking and fiber splitting failure criteria are determined in the fiber misaligned frame when the fiber is under compression. Fiber tension is satisfied when the tensile stress in the fiber direction exceeds the ply tensile strength. The matrix cracking criterion, which is relevant to the current study is determined using the following expression:

$$F_m^{crack} = \sqrt{\left(\frac{\tau_T}{S_T - \eta_T \sigma_N}\right)^2 + \left(\frac{\tau_L}{S_L - \eta_L \sigma_N}\right)^2 + \left(\frac{\langle \sigma_N \rangle_+}{Y_T}\right)^2} \tag{4.1}$$

Where S_L and S_T are the shear strengths of the matrix and Y_T is the transverse tensile strength of the matrix. σ_N, τ_T, and τ_L are the normal and shear stresses on the fracture plane of the matrix which is oriented perpendicular to the local 2-3 plane of the ply since the matrix crack runs parallel to the fiber. The stresses acting on this plane are determined from the 3D stress state of the element using the following expressions:

$$\sigma_N = \sigma_{22} cos^2\alpha + \sigma_{33} sin^2\alpha + \sigma_{23} sin(2\alpha)$$
$$\tau_T = \frac{1}{2}(\sigma_3 3 - \sigma_2 2) sin(2\alpha) + \sigma_{23} cos(2\alpha)$$
$$\tau_L = \sigma_{12} cos(\alpha) + \sigma_{31} sin(\alpha)$$

The angle α is the orientation of the critical plane and is determined numerically such that it maximizes the failure criterion F_m^{crack}. This method allows the prediction of inclined matrix cracks when the element is enriched using XFEM. The crack appears at the angle determined using the above method when the failure criterion is satisfied.

Damage initiation for delamination is determined using the quadratic nominal stress criterion in ABAQUS using the following expression:

$$\left(\frac{\langle t_n \rangle}{t_n^\circ}\right)^2 + \left(\frac{t_s}{t_s^\circ}\right)^2 + \left(\frac{t_t}{t_t^\circ}\right)^2 = 1$$

Where, t_n, t_s, and t_t are the cohesive tractions in the normal and tangential directions respectively. The cohesive strengths in the normal directions are represented by t_n° and the shear strengths by t_s° and t_t°.

The damage evolution for both delamination and matrix cracking is defined using the mixed-mode power law since this method showed a good correlation with experiments in [12]. The Power law failure criterion is given by,

$$\left(\frac{G_n}{G_n^C}\right)^\alpha + \left(\frac{G_s}{G_s^C}\right)^\alpha + \left(\frac{G_t}{G_t^C}\right)^\alpha = 1$$

Where, G_n^C, G_s^C, and G_t^C are the fracture energies determined for the cohesive interface in mode I, mode II, and mode III. G_n, G_s, and G_t denote the work done by the tractions in the normal and shear modes respectively. Failure occurs when the total work done by the reactions (G_T) is equal to the mixed-mode critical fracture energy (G_C). This occurs when the above expression is satisfied.

4.5 Non-Linear Solution Method

Modeling cohesive cracks is a highly non-linear problem that is prone to convergence issues. ABAQUS uses the Full Newton-Raphson procedure by default to find the root of the equilibrium equations. The full Newton-Raphson is a robust method that provides quadratic convergence when the initial guess is within the radius of convergence, otherwise results in divergence. Techniques such as line search or quasi-Newton approach can be employed in ABAQUS to avoid non-convergence of the results. The quasi-Newton solution method minimizes the cost of computing the inverse of the tangent stiffness matrix or the Jacobian matrix for every iteration. This method employs the BFGS algorithm to approximate the Jacobian. ABAQUS does not update the Jacobian in every iteration, rather the matrix is updated after 8 iterations or when the increment is reattempted due to non-convergence, thus reducing the computational effort. This method is suitable when the tangent stiffness matrix does not remain positive definite, which may occur during post-buckling or damage simulations.

However, the full Newton-Raphson method can yield converged results if the default solution control parameters are modified. The relevant parameters used in ABAQUS are listed below:

1. I_0: This is the iteration after which ABAQUS checks whether the residual is increasing after two iterations. By default, the fourth iteration (I_0 =4) is after which the check is

made. If the residual increase is found, the increment is attempted again with a smaller increment size.

2. I_R: The iteration after which logarithmic convergence is checked for every iteration. The default iteration number is 8, that is the check is performed from the ninth iteration onwards.

3. I_C: This is the maximum number of Newton-Raphson iterations allowed within an increment. If convergence is not achieved, the increment is repeated with a smaller increment size. The default is 16 iterations.

4. I_L: If the number of increments exceeds this limit, the size of the next increment is reduced. By default, this limit is 10.

5. I_G: If two consecutive increments converged with fewer increments than I_G, then the subsequent increment uses a larger increment size. By default, if less than or equal to 4 iterations are required for two consecutive iterations, the next increment size is increased.

6. I_A: Maximum number of cut-backs allowed for an increment. The default is 5

In the current study, the above values are modified as shown below:

```
TIME INCREMENTATION CONTROL PARAMETERS:
*** FIRST EQUILIBRIUM ITERATION FOR CONSECUTIVE DIVERGENCE CHECK          24
*** EQUILIBRIUM ITERATION AT WHICH LOG. CONVERGENCE RATE CHECK BEGINS     28
    EQUILIBRIUM ITERATION AFTER WHICH ALTERNATE RESIDUAL IS USED           9
*** MAXIMUM EQUILIBRIUM ITERATIONS ALLOWED                                26
*** EQUILIBRIUM ITERATION COUNT FOR CUT-BACK IN NEXT INCREMENT            22
*** MAXIMUM EQUILIB. ITERS IN TWO INCREMENTS FOR TIME INCREMENT INCREASE  24
    MAXIMUM ITERATIONS FOR SEVERE DISCONTINUITIES                         12
*** MAXIMUM ATTEMPTS ALLOWED IN AN INCREMENT                              25
```

Figure 4.2: Modified parameters are highlighted with asterisk

Furthermore, the tolerances related to the norm of the residuals (R_n^α) and displacement corrections can also be modified to improve the convergence rate. The default values are 0.5% and 1% respectively. However, these values are not modified in the present study.

4.6 Loads and Boundary Conditions

The clamps in the test specimen are used to restrict the longitudinal and vertical displacement of the test specimen. In the finite element model, partitions were created on the top and bottom sub-laminates to constrain all degrees of freedom to simulate the clamped boundary condition, that is $U_1 = U_2 = U_3 = 0$. Note that the longitudinal direction of the laminate, that is the fiber direction is aligned along the Z-axis in ABAQUS, therefore U_3 represents the displacements along the longitudinal direction. A more accurate representation of this boundary condition can be obtained by modeling the clamps and defining contact with friction

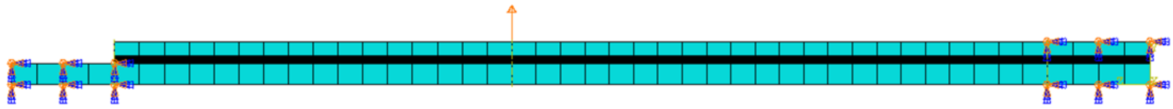

Figure 4.3: Load applied at L/a_0=1

between the clamp and laminate surfaces. However, this would increase the computational time, therefore, this has been ignored in the present study.

The out-of-plane load has been applied on a set of nodes on the top laminate. These nodes are located at a distance (L) which is equal to the pre-crack length (a_0) as shown in Figure 4.1. A displacement-controlled load of 1.5 mm is applied to these nodes since crack migration, if predicted accurately, would occur much earlier as observed in the literature.

4.7 XFEM Enrichment

Since the crack migration phenomenon is observed due to the presence of matrix cracking in the stack of 90° plies, the elements in this part are enriched with XFEM in ABAQUS. This is done in the interaction module of ABAQUS. The default XFEM enrichment in ABAQUS only allows one crack to initiate and propagate within the enriched region. However, this default setting leads to severe convergence difficulties due to the presence of secondary matrix cracks that initiate when the delamination propagates in the lower 90/0 interface. This issue was overcome by modifying the keywords to account for multiple cracks in the enriched region. This is shown below:

Default method:
*Enrichment Activation, name=Crack-name, activate=ON

Modified keyword:
*Enrichment Activation, name=Crack-name, activate=MULTICRACKS

The above keyword allows XFEM in ABAQUS to handle multiple cracks and is useful for composite plies since secondary cracks are commonly observed. Using this keyword also alleviates the need to partition the domain into multiple enriched regions.

4.8 Mesh

As mentioned earlier, the top and bottom laminates were modeled using solid elements with one row of elements for the entire layup. The mesh was refined near the crack tip and coarse mesh was used near the clamped ends. An element size of 1mm was present close to the crack tip while the element size at the clamped end was 3mm.

The solid elements for the three parts $90_4, 0_3$ and 0 were meshed with uniform element sizes. Initially, a mesh convergence study is performed to determine a suitable mesh size for these parts. One layer of elements is used for each ply in these parts, hence, the thickness of the elements is equal to the ply thickness, which is 0.12mm. To obtain the best results using solid elements, the aspect ratio would need to be 1 which is not feasible in this simulation. The element sizes that were checked for mesh convergence were 0.4, 0.5, 0.6, and 0.7mm. For all these cases, the aspect ratio of the elements is less than 10, which is within the acceptable limit. Element sizes smaller than 0.4 was also checked but were aborted due to significantly high computational time (70 hours with 20 cores)for much lower applied displacements (1.3mm).

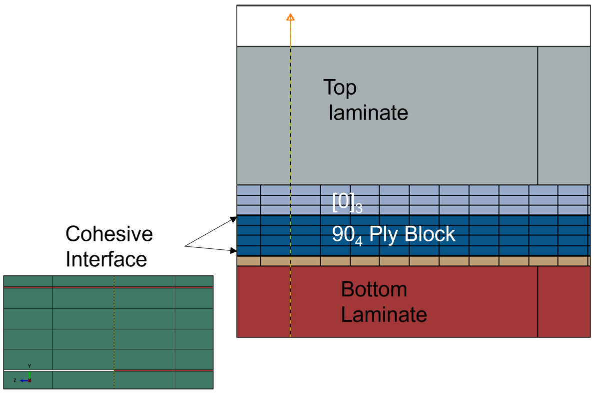

Figure 4.4: Mesh and stacking of Crack Migration model

For delamination, the length of the cohesive element is a crucial parameter due to the high mesh dependency. A guideline that is commonly followed is to place 3-5 cohesive elements within the cohesive zone. Therefore, the length of the cohesive zone for IM7/8552 was calculated using the following expression:

$$l_{cz} = M\frac{E_{33}G_{IC}}{t_n^2} \tag{4.2}$$

Where E_{33} is the out-of-plane elastic modulus of the interface material. This is assumed to be the same as the transverse elastic modulus of the ply E_2. The mode I fracture energy and cohesive strength in the normal direction of the interface material is denoted by G_{IC} and t_n. The parameter M is a constant that takes different values across literature. Here, M is assigned 0.88 based on the work by Turon et al [29]. Substituting these values in the above expression results in a cohesive zone length of 0.56mm. This would require a very fine mesh with approximately 0.18mm element size if 3 elements are used in the cohesive zone. Therefore, a fine cohesive element mesh with 0.18mm was used for the mesh convergence study of the ply solid elements.

4.9 Study on the Effect of Cohesive Zone Length

The cohesive mesh used in the mesh convergence for the solid elements required a very large computational time due to the high number of degrees of freedom. It was shown in [30] that cohesive zone length may be adapted by reducing the normal strength of the interface material. This would allow using a coarser mesh for the cohesive interface. The interface strength is found using,

$$\sigma_N = \sqrt{M\frac{E_{33}G_{IC}}{N_e l_e}} \tag{4.3}$$

Where, N_e is the desired number of elements in the cohesive zone, which is often 3, and l_e is the element length. This method applies only to strength-insensitive cases as demonstrated by Lu et al in [47]. The approach is limited to cases where the laminate consists of any high-stress gradients due to the presence of crack tips or stress concentration. Since a pre-crack is present in the migration test specimen, the following parameter studies are done only by adapting the strengths of the cohesive elements with increasing element lengths. This parametric study was used to study the effect of interface cohesive zone length on the peak load and migration location if predicted. Insensitivity to either of these parameters would allow the use of a coarse cohesive mesh with smaller initiation strengths.

Cohesive zone length and strength for $N_e = 3$			
Desire element size l_e (mm)	0.19	0.25	0.50
New strength – normal (MPa)	59.72	52.06	36.81
New strength – shear (MPa)	77.10	67.21	52.06
LCZ – New (mm)	0.57	0.75	1.50

Table 4.4: Parameter study based on l_{cz}

In the parametric study outlined above, the ply properties were maintained without modification, retaining the transverse strength and fracture energies presented in Table 4.1. This approach was taken even as the delamination cohesive zone length was adapted. However, it is important to note that the cohesive segments employed in the XFEM framework could also be influenced by the cohesive zone length, necessitating careful consideration of this parameter.

Refining the mesh for cohesive elements was found to be infeasible due to the significantly increased computational time associated with such modifications. Interestingly, strength insensitivity was observed for delaminations when stress concentrations were present. Given this observation, it can be hypothesized that a similar insensitivity may also apply to the matrix during the modeling of migration events. Therefore, adjusting the cohesive zone length for the matrix is regarded as a viable alternative, particularly if the current methodology does not successfully predict migration.

To facilitate this adjustment, the previously discussed expression will be utilized to determine the matrix strength, allowing for the adaptation of the cohesive zone length associated with matrix behavior. This approach aims to enhance the model's ability to capture the complexities of crack migration and the interactions between different damage modes in the composite structure.

In summary, while maintaining the original ply properties provides a baseline for comparison, the exploration of cohesive zone length adjustments for both delaminations and matrix cracks represents a critical step in optimizing the XFEM-CZM approach. The following chapter will present the results of these simulations, highlighting the effectiveness of the chosen methodologies and the insights gained from the parametric study.

Chapter 5

Crack Migration Test - Results

In the first section of this chapter, the results obtained from the mesh convergence study will be presented. The element length that satisfies the convergence criteria will be used in the parametric study to evaluate the influence of the cohesive zone length on the migration phenomenon. The objective is to determine if the modified cohesive zone length affects the crack migration location (Δ). A low sensitivity of this parameter would indicate that a coarser cohesive mesh may be used, allowing faster simulations with minimum loss of accuracy in strength-insensitive cases. The subsequent section will present the effect of matrix cohesive length on the migration phenomenon. Since the cohesive length of the material is extremely small, placing three solid elements in the cohesive zone requires a fine mesh to capture cohesive cracks using XFEM. Assuming that the matrix crack that leads to migration is also strength insensitive, the matrix strength is modified to assess whether the prediction differs from the earlier cases. The fracture energies used in all these simulations are the same for the matrix and delamination. However, some studies in the literature have indicated that the orientation of the adjacent ply influences the fracture energy at ply interfaces. The penultimate section will present the influence of different fracture energies of the matrix and delamination to assess its effect on the migration location. The final section is dedicated to the discussion related to the results obtained.

5.1 Mesh Convergence of Solid Elements

The 90° ply block and the zero-plies are meshed using 0.4, 0.5, 0.6, and 0.7mm solid elements with a single row of elements per ply. Since the cohesive elements are generated using a separate part in ABAQUS, a refined cohesive mesh with an element length of 0.18mm is used ensuring three cohesive elements are present in the cohesive zone of the material. The mesh convergence for the solid elements is done based on the convergence of the peak load. The peak load plotted as a function of the element length is shown in (Figure 5.1).

Le (mm)	Peak Load (N)	Relative change	Difference between reference current method
0.7	218.819	0%	4.35%
0.6	196.107	10.38%	6.48%
0.5	194.833	0.65%	7.09%
0.4	194.305	0.27%	7.34%

Table 5.1: Comparison of peak load obtained with different solid element lengths

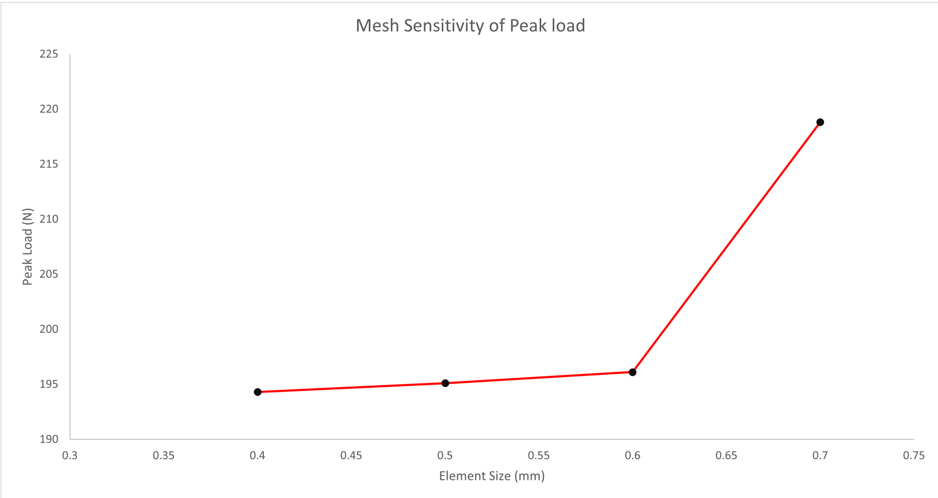

Figure 5.1: Peak Load variation with decreasing element size

The peak force in comparison with the peak load predicted in [40] using the floating node method (FNM) is presented in the following table. The peak obtained from the FNM simulation in the reference is around 209.7N.

The peak load of 0.7mm is the highest but has the least deviation from the reference result. The highest deviation of 7.34% is observed for 0.4mm element size. However, the peak load appears to converge to a lower value with increasing mesh density. The highest relative difference is observed when the element size is changed from 0.7 to 0.6mm. The least relative change of 0.25% is obtained when the element length is reduced to 0.4mm from 0.5mm, indicating that refining the mesh after 0.5mm may not significantly change the peak load. The peak load predicted by the models with fine mesh could be attributed to the difference in the boundary conditions between the reference methodology in [40] and the current method. The reference method modeled contact between the laminate and the clamps which predicts the deflection of the specimen more accurately. However, the following simulations were carried out with the nodal displacements in the clamped region being constrained in all directions.

5.2 Effect of Interface Cohesive Length

The above simulations were carried out using the properties from [36] with a cohesive element length of 0.18mm which is computationally expensive. A coarse cohesive mesh can be used to reduce the computational effort but it is necessary to ensure the presence of 3 to 5 cohesive elements in the cohesive zone. A coarse mesh would also result in the over-prediction of the peak load and an inaccurate post-peak response. This issue could be alleviated by adapting the cohesive zone and reducing the initiation strength for delamination. The delamination at the first interface will largely depend on the fracture energy rather than the strength due to the presence of the pre-crack as shown in [47]. Therefore, the strengths of the cohesive elements will be changed while the matrix strength used will remain the same as the original values. Three cohesive zone lengths of 0.57mm, 0.75mm, and, 1.5mm were selected. Placing three elements in each cohesive zone results in element lengths of 0.19mm, 0.25mm, and 0.5mm respectively. The first cohesive zone length is approximately the same as the original case. For the second cohesive zone length, two cohesive elements of 0.25mm will be present per solid element of 0.5mm while one cohesive element of 0.5mm per solid element will be present for the third case.

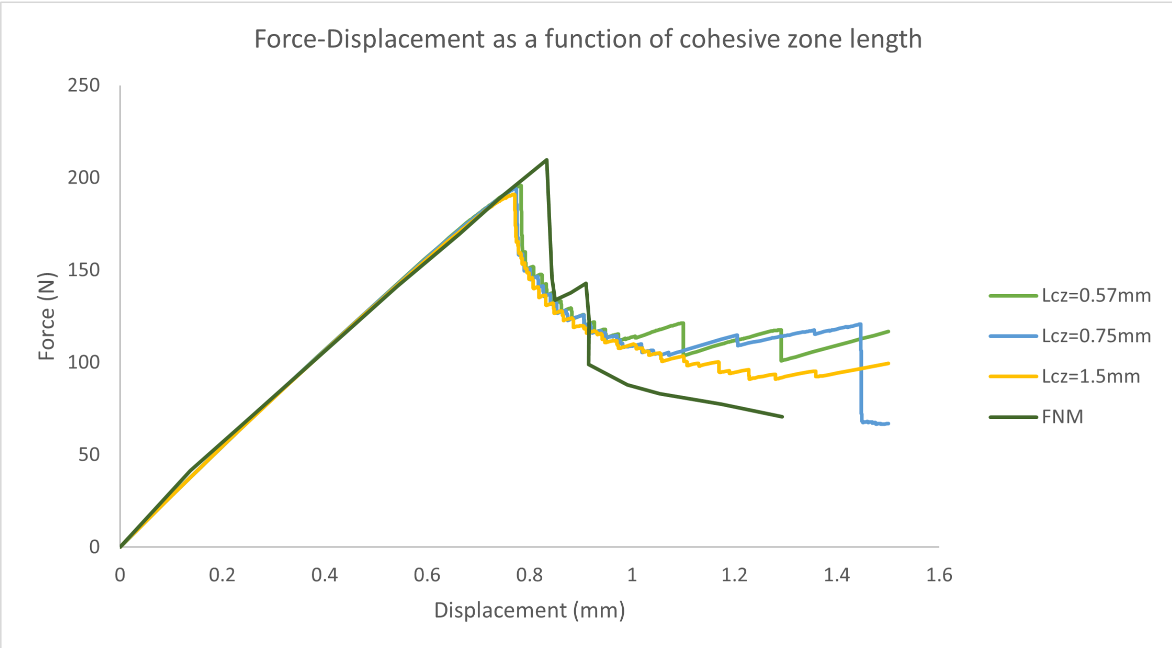

Figure 5.2: Load response curve plotted for varying delamination cohesive zone length

The plot in Figure 5.2 shows the force response for each case and the difference between the peak force is minimal due to the strength insensitivity of the initial delamination. The post-peak response is similar until the displacement is approximately 1mm after which a stable increase in the reaction force followed by an unstable drop in the load is observed for both cohesive zone lengths of 0.57mm and 0.75mm. The phenomenon occurs repeatedly for the 0.57mm case. However, for the 0.75mm cohesive length, an unstable load drop is observed after a displacement of 1.4mm. The load response after the unstable drop in the load appears to coincide with the FNM curve. The two unstable load drops observed in the FNM curve correspond to the delaminations observed at the two interfaces. Similar force response characteristics are observed for the 0.75mm cohesive zone, however, the second unstable drop in load is delayed when compared with the FNM curve. Since the second unstable response corresponds to the migration event, this indicates that the migration is significantly delayed.

The load response for 1.5mm deviates from the other two cases showing no distinct load drops or stable increase in the load.

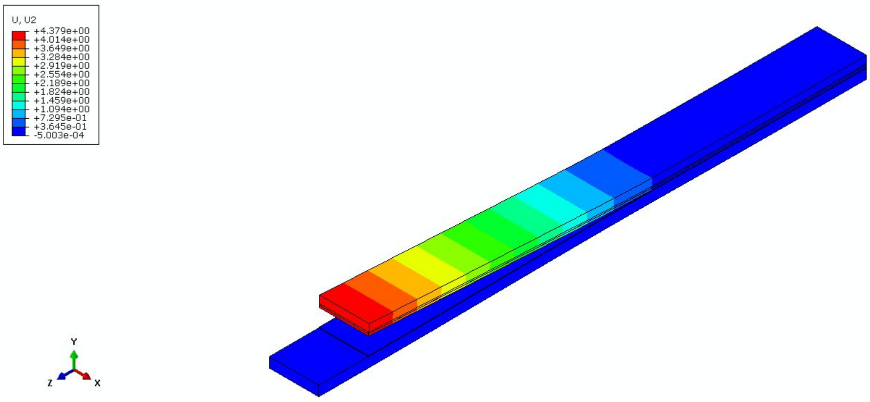

Figure 5.3: Deformed configuration of the specimen with coordinate system

The specimen's deformed configuration is presented along with the coordinate system in Figure 5.3. The coordinate system will be essential to interpret the contour of the damage variables in the following figures. The damage variable in the bottom interface is plotted in Figure 5.4 for the three cohesive zone lengths. In this interface, delamination is observed in all three models. The length of the delamination is similar for the first two cases. However, for the 1.5mm case, the delamination appears to terminate in the middle while it propagates near the free edges. The delamination is also accompanied by matrix cracks in the 90_4 ply block plotted in Figure 5.7 and are oriented at an angle that is similar to the orientation observed in the experiments. The STATUSXFEM variable indicates the severity of the crack opening where 1 represents a fully opened crack, 0 indicates no crack and any value in between indicates a partially opened crack or a partially damages matrix. Many partially opened cracks can be observed in all three cases indicating multiple crack kinking events.

Delamination migration becomes favorable when the kinked matrix crack has degraded completely. However, migration is said to have occurred when delamination is also observed in the top interface. The stiffness degradation variable (SDEG) corresponding to the top interface interface is plotted in Figure 5.5. To assess migration, both Figure 5.5 and Figure 5.7 need to be considered. Although significant delamination is not observed in Figure 5.5a, the regions that have a non-zero SDEG value coincide with the matrix where STATUSXFEM is 1. In the case of 0.75mm cohesive zone length migration is first observed in the mid-width point of the specimen which coincides with the matrix crack in the ply block. However, complete degradation of the matrix crack near the free edges is not observed and the delamination continues to propagate at the bottom interface. The subsequent matrix crack in the 90_4 ply block degrades uniformly across the width which becomes favorable for migration. This results in delamination across the width of the top interface of the specimen as observed in Figure 5.5b. In the case of 1.5mm cohesive zone, the matrix crack degrades only in the middle similar to the first matrix crack observed in the 0.75mm case. The delamination in the bottom interface terminates at this location since migration becomes favorable. The delamination in the top interface can be observed in Figure 5.5c. The region of this delamination is consistent with the location where the matrix crack has completely degraded. Migration can be captured in the models corresponding to 0.57mm and 1.5mm cohesive zones with further loading. However, migration is expected to occur at a distance of 8-9mm as observed in experiments as well as in [40]. In the three cases above, migration and kinking attempts are observed much later.

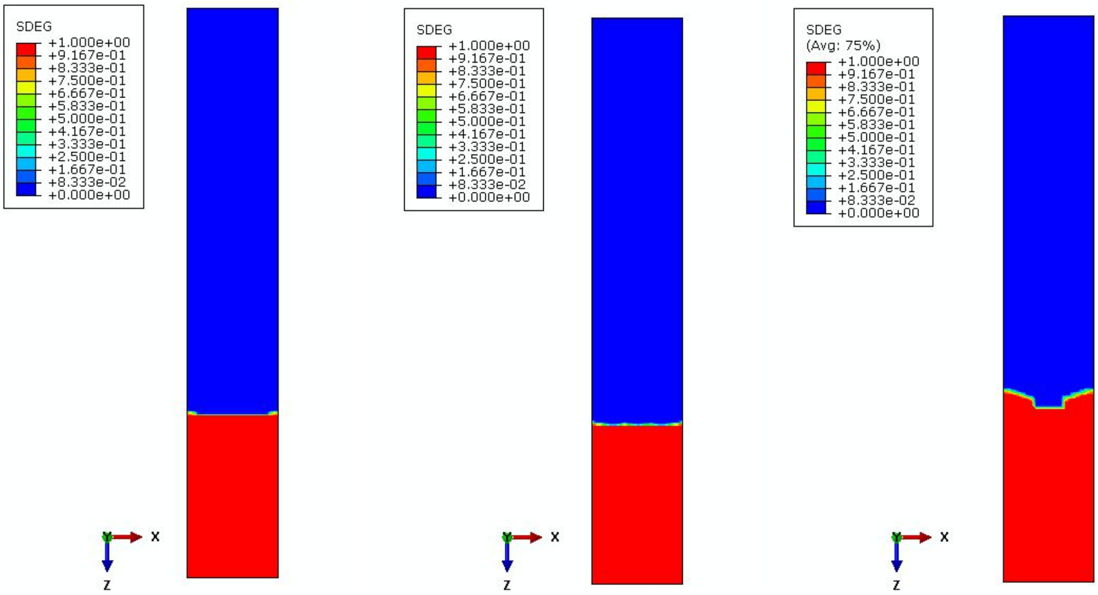

(a) L_e=0.19mm **(b)** L_e=0.25mm **(c)** L_e=0.50mm

Figure 5.4: Damage in the bottom 0/90 interface cohesive elements

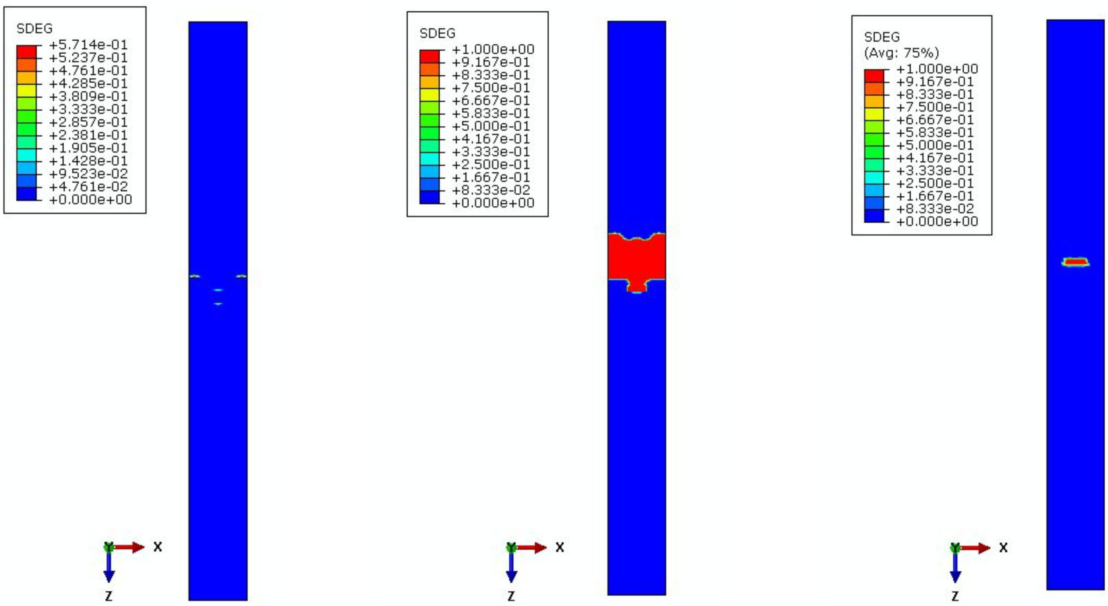

(a) L_e=0.19mm **(b)** L_e=0.25mm **(c)** L_e=0.50mm

Figure 5.5: Damage in the top 90/0 interface cohesive elements

The first attempt of crack migration or crack kinking for the three cases is plotted in Figure 5.6. The values in the plot are the locations where delamination in the bottom interface terminates

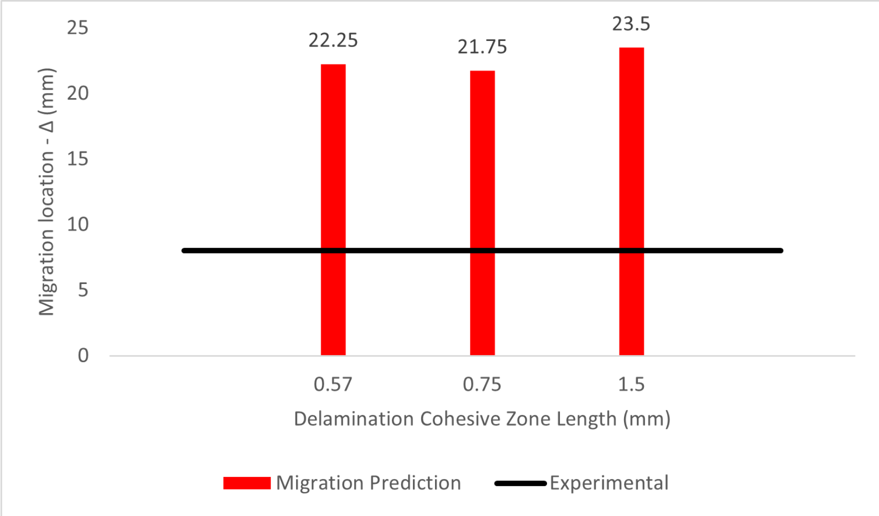

Figure 5.6: Migration location as a function of Cohesive Zone Length

and the first attempt of migration occurs due to the degradation of the matrix crack. For the 0.75mm case, the location where the crack migration is plotted since it is the only model that predicts migration. The horizontal line at Δ =8mm represents the location at which migration is often observed in experiments. The distance is measured from the pre-crack front. The Δ for each case is almost 3 times the distance observed in experiments. The difference in the locations does not vary significantly. The difference between the crack kinking location for 0.57mm and 0.75mm case is 0.5mm which is equal to the solid element length which indicates minimal variation in the crack kinking location. Although migration is captured in only one of the three cases, crack kinking attempts is observed in all the cases at a distance far behind the expected migration location. Almost no matrix crack degradation is observed close to the location where migration is expected.

Matrix cracks are also observed at a distance of 8-9mm from the pre-crack front however they are confined to the first layer of elements and do not extend across the width of the specimen nor grow through the thickness. These cracks do not degrade further and hence do not create favorable conditions for crack migration. Crack nucleation in the solid element occurs only when the LaRC05 failure criterion is satisfied. The stress concentration due to the delamination initiates a matrix crack in the first layer of elements. The stress concentration due to the degradation of the matrix crack in the first layer would initiate cracks in the elements above the first ply resulting in crack growth through the ply block. Crack degradation in an element would also initiate matrix cracks in the adjacent element within the same layer resulting in crack growth across the width. However, crack growth does not seem to occur uniformly across the width in the above simulations. For instance, the degradation of matrix crack is only confined to the middle elements in the first layer as seen in Figure 5.7a. This could be attributed to inaccurate energy dissipation when the crack grows across the width. The matrix crack degradation follows the extrinsic traction-separation law, which means mesh refinement in the matrix cohesive zone would be necessary for accurate energy dissipation during the damage evolution. One layer of element per ply provides sufficient refinement through the thickness since the cohesive zone is much larger than the ply thickness, therefore mesh must be refined across the width. However, further mesh refinement resulted in a computationally expensive simulation. Therefore, in the subsequent section, adapting the matrix cohesive zone is explored as an alternate strategy to predict migration using the current mesh configuration.

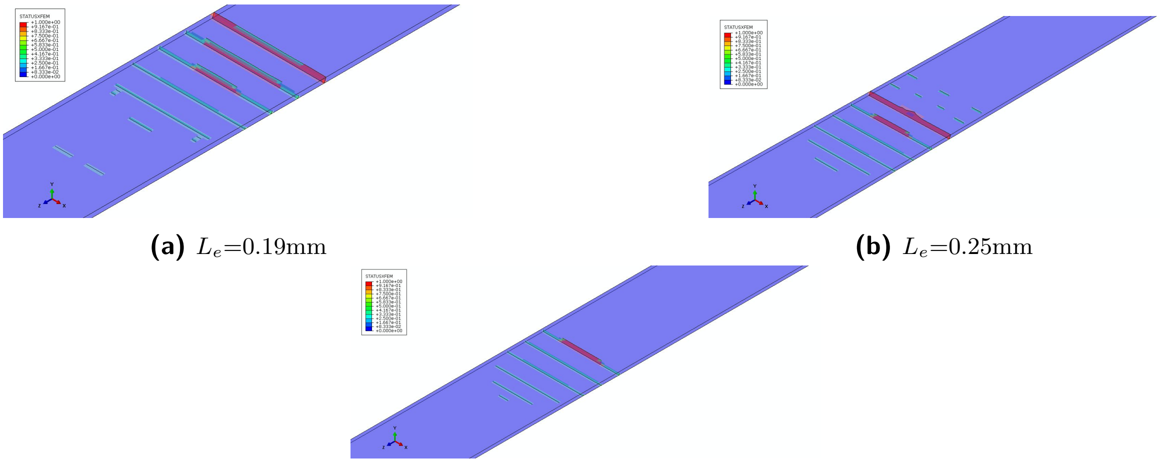

(a) L_e=0.19mm

(b) L_e=0.25mm

(c) L_e=0.50mm

Figure 5.7: Matrix crack in 90_4 ply block

5.3 Effect of Matrix Strength

The solid element length obtained from the mesh convergence study was 0.5mm whereas the cohesive zone length of the matrix material is 0.56mm. Placing three elements in the cohesive zone would require solid elements as small as 0.18mm. This simulation was found to be computationally expensive. As an alternate approach, the cohesive zone length of the matrix was adapted by reducing the transverse strength and the shear strength of the ply. The new transverse and shear strengths for the matrix crack, which were calculated at least three elements in the cohesive zone, are 33.61 MPa and 43.38 MPa. The cohesive zone length for this case is 1.8mm. The same initiation strengths were assigned to the cohesive elements as well since the peak load was found to be strength-insensitive. In addition to the above simulation, another simulation was conducted where the matrix crack strength was 1.2 times the delamination strength, which resulted in a transverse strength of 40.32MPa and 52.05MPa and the resulting cohesive zone length was 1.25mm. The objective of this section is to observe whether the lower initiation strength promotes migration at a distance of 8-9mm from the pre-crack as observed in experiments.

The plot in Figure 5.8 shows the force response of the specimen for the two modified strengths in comparison with the previous simulations where the delamination cohesive zone length was 0.75mm and matrix strengths were not modified. The peak load in all three cases is the same since the initial delamination is not sensitive to the initiation strength. The force response for the matrix strength of 40.32 MPa is almost similar to the unmodified matrix strength case, indicating that the migration likely occurs at the same location. However, in the case of a matrix strength of 33.6 MPa, two peaks are observed after the first peak. The first peak after the delamination occurs at an approximate displacement of 0.9mm after which there is a stable increase in the force before an unstable drop in the load is observed at a displacement of 1.3mm. To understand what these peaks represent, the sequence of damage predicted by the simulation was observed.

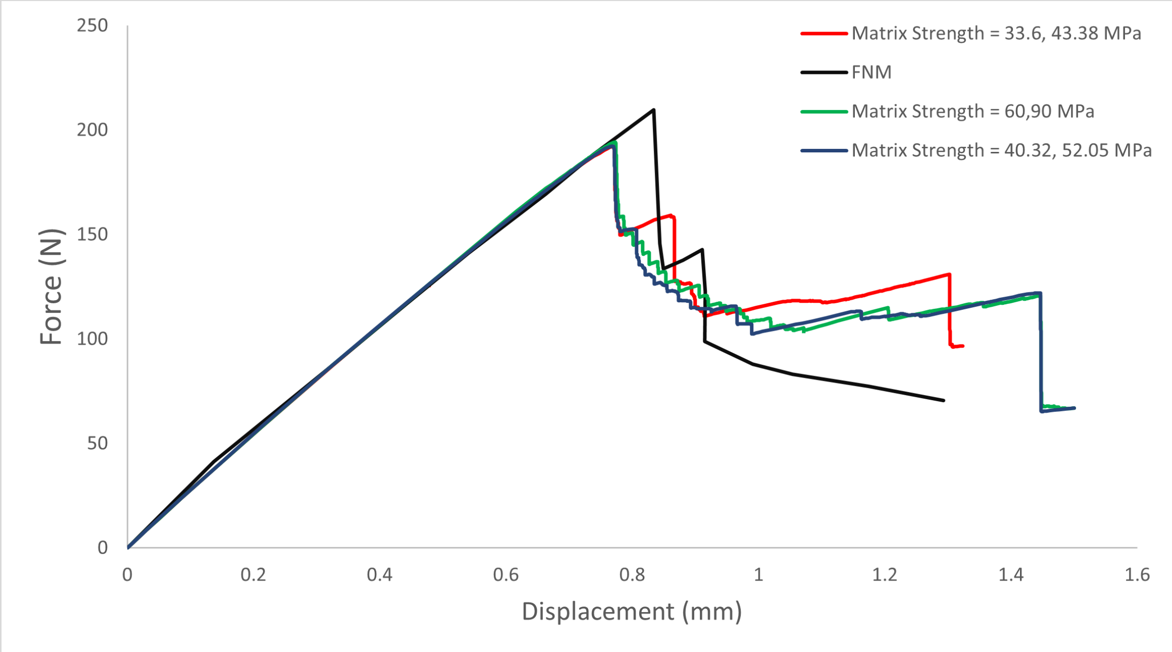

Figure 5.8: Force Response with modified matrix strength

In Figure 5.9, the matrix crack growth corresponding to the different stages of the force response is presented. The first linear stage of the force response has no significant matrix cracks and the load drop only corresponds to the delamination growth at the bottom interface. In the second stage, the second peak and unstable drop in the load are accompanied by a matrix crack degradation. However, as shown in the figure, the orientation of the matrix crack with respect to the delamination growth direction is greater than 90°. This orientation of the crack does not enable migration, and is likely caused by negative shear stresses. On further loading, the subsequent matrix cracks that initiate are oriented with a θ less than 90°, which is favorable for migration. In the final stage of the force-displacement curve, the unstable drop in the load indicates the degradation of the matrix crack which enables migration. The matrix crack observed in the second stage propagates through the thickness of the specimen. The propagation of this matrix crack through the thickness results in the termination of the delamination in the bottom interface and results in a delamination at the top interface.

Although the force responses for the matrix strengths of 40.32MPa and 60 MPa are similar, the migration location is significantly different as shown in Figure 5.10. The migration for the transverse strength of 33.6MPa occurs at 18.5mm and for the transverse strength of 40.32 MPa is observed at 18mm as shown in Figure 5.10a and Figure 5.10b. The migration is delayed by one element for the 33.6MPa case. However, for 60MPa, the migration is observed at a distance of 21.75mm and the offset is almost 3-3.5mm, which is roughly 6-7 elements in the longitudinal direction. The early migration observed in the 40.32 MPa case does not justify the force response being similar to the 60 MPa case. One can observe that the offset of 3-3.5mm is equivalent to the crack spacing observed in all three simulations in Figure 5.10. Matrix cracks initiate every 6-7 elements as the delamination grows and this spacing does

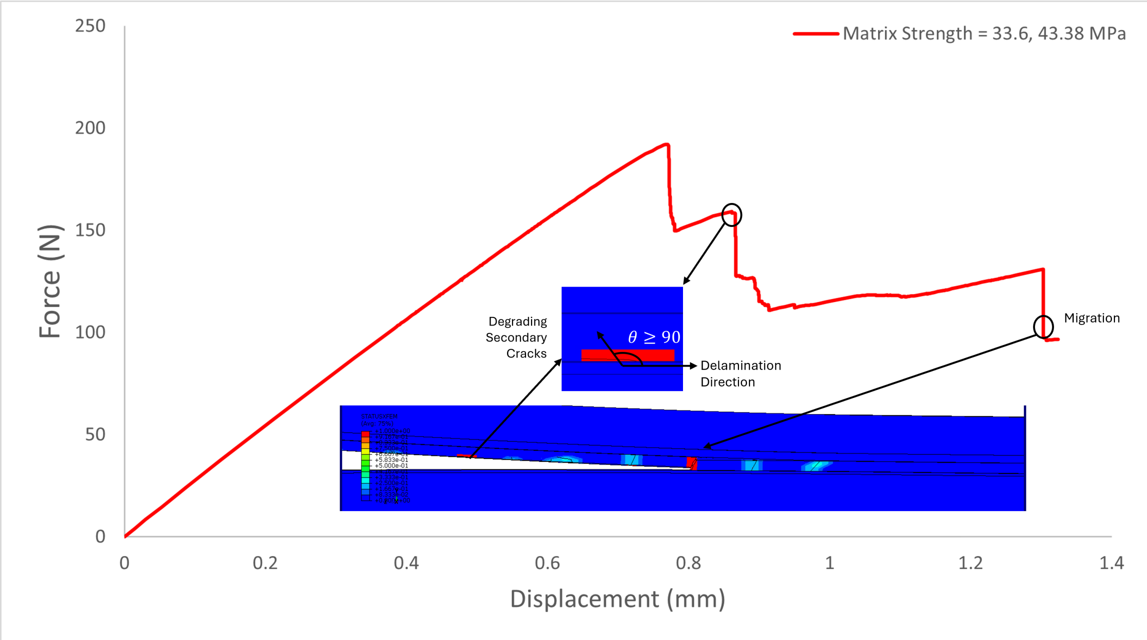

Figure 5.9: Sequence of damage and migration for matrix strength of 33.6 MPa and 43.8 MPa shown along with force response

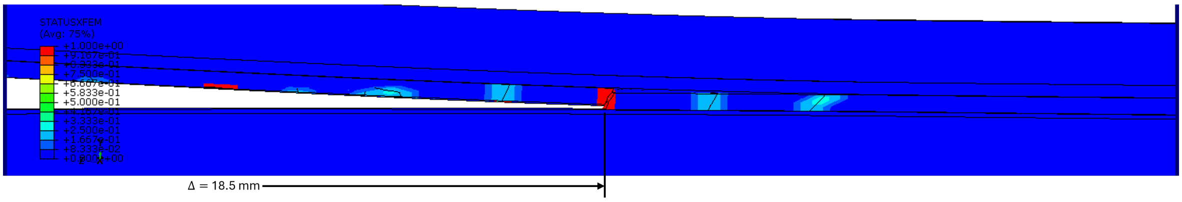

(a) Transverse Strength = 33.6MPa, Shear Strength = 43.38MPa

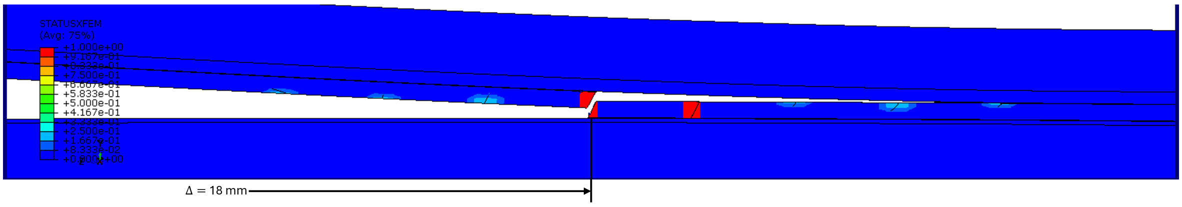

(b) Transverse Strength = 40.32MPa, Shear Strength = 52.05MPa

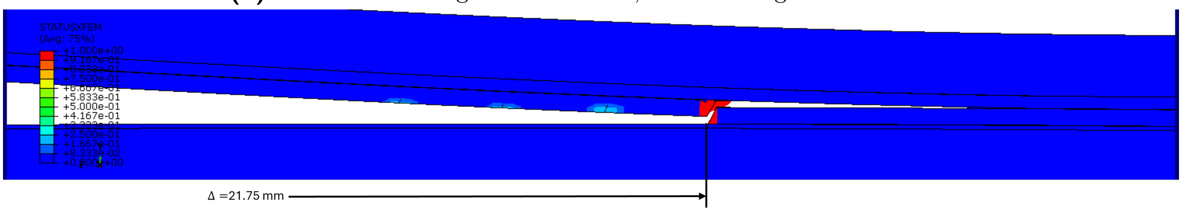

(c) Transverse Strength = 60MPa, Shear Strength = 90MPa

Figure 5.10: Crack Migration location for each case

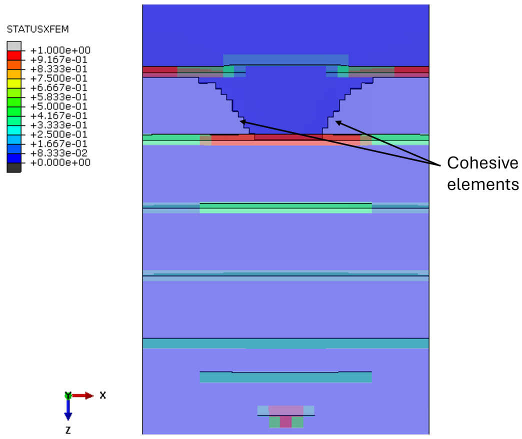

Figure 5.11: State of damage in the specimen corresponding to the peak before second unstable load drop for the case of matrix strength of 40.32 MPa

not change with variation of the matrix strength. Migration occurs when one of these cracks degrades completely across the width and thickness. For 33.6MPa only one matrix crack with the correct orientation appears to degrade completely across the width at a distance of 18.5mm. However, for 40.32 MPa, a second matrix crack degradation can be observed behind the migration location in Figure 5.10b. This crack occurs at a distance of 21.75mm which coincides with the migration location of 60 MPa, however, this matrix crack does not result in migration. To understand what causes the similarity in the force response with the 60 MPa case, the sequence of damage for the 40.32 MPa case was studied. The damaged state of the 90° ply block before migration is presented in Figure 5.11. The cohesive elements behind the first degraded matrix crack are undamaged while significant delamination is observed near the free edges where the matrix has not degraded. As this delamination grows at the free edges, a new matrix crack is initiated 6 elements behind the first degraded matrix crack. This new matrix crack grows through the thickness, however the crack does not grow across the width. The progressive degradation of both the matrix cracks results in a stable increase in the reaction force as the specimen is loaded further. However, on further loading the first matrix crack fails across the width and results in migration. In the case of 60MPa, a similar damage sequence is observed. The undamaged cohesive elements behind the first matrix crack fail on load application and the subsequent migration occurs through the second matrix crack which occurs at a distance of 21.75mm.

The migration location predicted by the two simulations presented in this section does not correlate well with the expected distance of 8-9mm. A matrix crack with a correct orientation ($\theta \leq 90°$) initiates at a distance of 12mm. However, this crack does not grow through the thickness and is not favorable for migration. Although different strengths were used in the study presented above, the matrix crack nucleation sites were the same as in the 60MPa case. The crack spacing between the nucleation sites remained the same for all cases. The migration locations for 33.6MPa and 40.32MPa are almost the same, however, the sequence of damage and force response are similar for the 40.32 MPa and 60 MPa matrix strengths. Migration attempts were also observed at 18.5mm in the case of 60 MPa. However, migration was delayed since delamination was energetically favorable. Therefore, migration is promoted only when the energy release rate of the matrix crack exceeds the fracture energy of the matrix

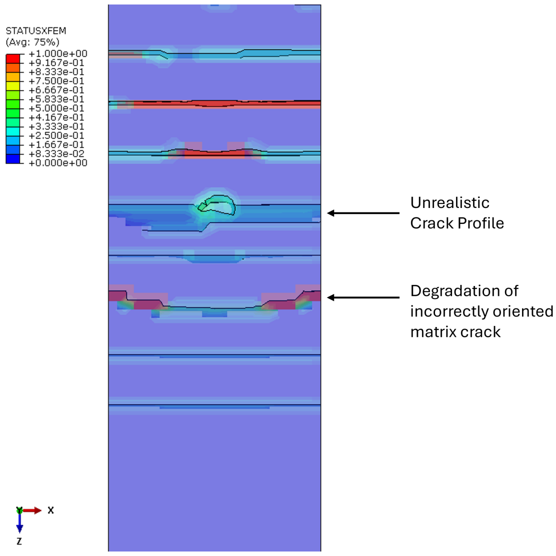

Figure 5.12: Matrix Crack Profiles in 90○ ply block with matrix strength of 33.6 MPa

as well as the energy release rate of the delamination. Therefore, one could conclude that a lower matrix fracture energy would promote delamination migration while a higher fracture energy would result in a delay. A low matrix strength would result in more nucleation sites thus promoting migration through the matrix crack in these sites. To test whether this is true, a parametric study would be required where the matrix cohesive parameters are altered while the delamination properties are held constant.

In the case of 33.6 MPa, secondary cracks are initiated and oriented incorrectly as shown in Figure 5.9. The degradation of these cracks resulted in inaccurate force response of the specimen. The initiation of these cracks may be attributed to inaccurate shear stresses in the solid elements since full integration elements used in these simulations are prone to shear locking. Furthermore, subsequent matrix cracks shown in Figure 5.12 were not uniform across the width and do not seem realistic. The reason behind the formation of such cracks could not be identified. Initiation and degradation of such cracks are not desirable for a parametric study. In the following section, the effect of mesh discretization through the thickness of the stack of 90° plies and the influence of the element integration scheme on the migration prediction will be studied to observe whether such inaccuracies are predicted.

5.4 Thickness Discretization and Integration Scheme

Since complex matrix crack profiles were predicted in the models used in the previous section, the above simulation with the matrix strength of 33.6MPa was repeated with a single layer of element through the thickness of the ply block. This was done to study whether similar inaccuracies in the crack profile are observed when a coarse mesh is used. Additionally, two more simulations with reduced integration elements were carried out to observe whether they predict the degradation of incorrectly oriented matrix cracks. The first simulation with reduced integration elements consists of one layer of elements through the ply-block while the second simulation consists of four layers of reduced integration elements.

The matrix cracks predicted from the three simulations are presented in Figure 5.13. In the case of the full integration element, Figure 5.13a, two matrix cracks can be observed where the second matrix crack has degraded completely across the width. The delamination in the bottom interface is shown in Figure 5.14a and the delamination in the top interface can be seen in Figure 5.14b. The first instance of the delamination in the top interface coincides with the first degraded matrix which is restricted to the mid-region of the crack. Complete migration is obtained when the second matrix crack fails resulting in delamination propagating in the top interface. The matrix cracks propagate along the same row of elements and do not display any significant variations. There are also no partially degraded secondary cracks observed in this simulation and the migration occurs at a distance of 20.7mm. However, the first migration attempt occurred 8mm earlier since the crack spacing is roughly 8mm in this case.

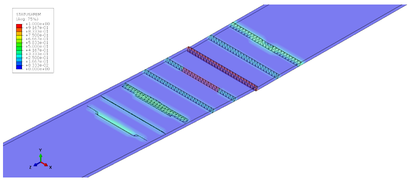

(a) Single C3D8 element

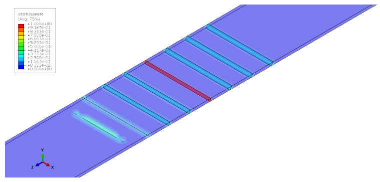

(b) Single C3D8R element

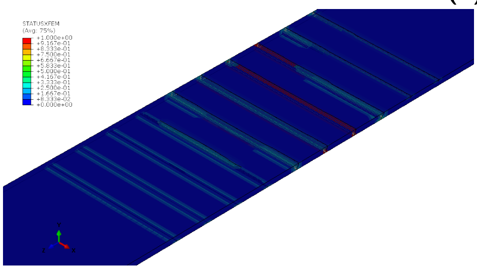

(c) 4 C3D8R element

Figure 5.13: Migration predicted with single element through the thickness

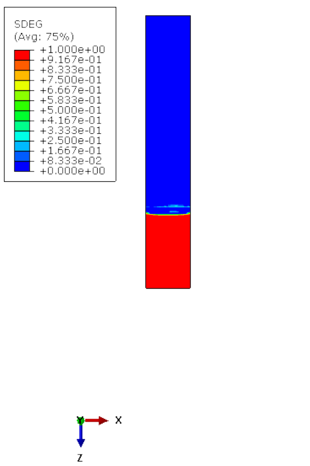

(a) Cohesive Elements in Bottom 0/90 interface

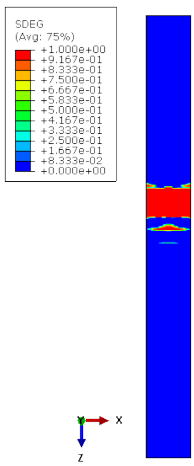

(b) Cohesive Elements in Top 90/0 interface

Figure 5.14: Migration predicted with single element through the thickness

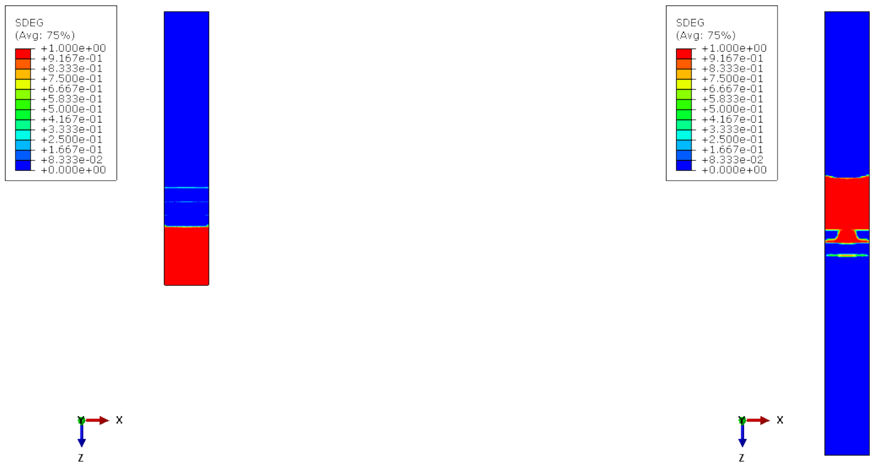

(a) Cohesive Elements in Bottom 0/90 interface

(b) Cohesive Elements in Top 90/0 interface

Figure 5.15: Migration predicted with single reduced integration element present through the thickness

In the case of the coarse reduced integration element, only a single matrix crack degrades and results in migration as seen in Figure 5.13b. However, the first instance of delamination in the top interface observed in Figure 5.15b does not align with the location where the matrix crack occurs. The delamination predicted occurs at a distance of 16.5mm however the deformation of the specimen is not accurate since a single reduced integration element does not capture the bending behavior of the upper sublaminate accurately. Therefore, the delamination observed at the top interface does not align with the location where the matrix crack fails.

Four layers of reduced integration elements captured the bending behavior more accurately. The resulting matrix cracks for this model, are shown in Figure 5.13c. Multiple matrix cracks initiate in the specimen throughout the loading sequence, and migration occurs at a distance of 18.7 mm which is similar to the migration location observed with four layers of full integration elements. Complex crack surfaces and degradation of cracks with incorrect orientations were not observed in this simulation.

The degradation of secondary cracks observed in the refined full integration elements might not be a realistic phenomenon or at least, is not reported in the literature. The discontinuity introduced by XFEM in the bulk elements is only an artifact of the initiation criterion being satisfied due to the stress state of the bulk material when the specimen is loaded. In the experiments, the effect of negative shear stress is predominantly observed in the 0/90 interface close to the pre-crack when delamination initiates in the specimen. The authors of [1] report shear hackles in the delaminated surface close to the pre-crack which is a result of the shear stress in the interface. The crack originating from the PTFE insert attempts to propagate into the lower 0° ply, however, the lack of energetically favorable conditions forces the crack to propagate in the interface as a delamination. In this region, the crack propagates in a mixed-mode condition up to a certain distance after which the delamination is mode I. This phenomenon at the ply interface cannot be captured accurately by the FEM model since the failure of the matrix and delamination are treated separately. However, the negative shear stress that results in shear hackles could have manifested itself as an XFEM crack which resulted in degradation in the solid elements. Since this is an extremely local phenomenon,

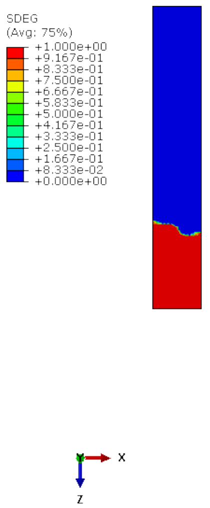

(a) Cohesive Elements in Bottom 0/90 interface

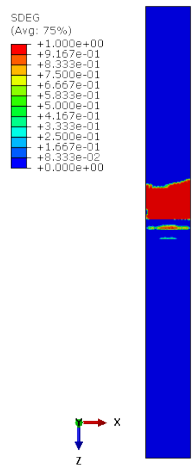

(b) Cohesive Elements in Top 90/0 interface

Figure 5.16: Migration predicted with four layers of reduced integration element

this event could have been captured only when a fine mesh is used with full integration elements and when sufficient elements are present in the cohesive zone. The three cases present in this section do not provide sufficient fidelity to capture this local phenomenon, therefore degradation of secondary cracks may not be observed.

To study the effect of matrix cohesive parameters on migration more accurately, it may not be ideal to use full integration elements in the current model. This is to avoid capturing local stress fluctuations that influence the subsequent damage events as well as the global response of the laminate. Full integration elements present across the thickness of the element can provide sufficient resolution for the stress state of the plies and even predict an accurate matrix crack across the width of the laminate. The matrix cracks predicted by reduced integration elements also appear to be sufficiently accurate in terms of the orientation of the crack. The model with reduced integration elements allows capturing the migration event fairly accurately without degradation of secondary cracks or complex crack profiles therefore, the following parametric study was done using the model.

5.5 Parametric Study

Earlier sections indicated that lower matrix strength results in more nucleation sites, however, migration occurred when the delamination was not energetically favorable. Different matrix strengths and fracture energies were used to determine what parameter delays or promotes migration. The matrix strengths and fracture energies ratios used in this parametric study are presented in Table 5.2. The strength ratio refers to the ratio between the matrix crack strength to the interlaminar strength. Similarly, fracture ratio refers to the ratio of fracture energy between matrix fracture energy and interlaminar fracture energy. The interlaminar strength and fracture energies were held constant for all the cases.

Strength Ratios	Transverse Strength (MPa)	Shear Strength (MPa)	G_{Ic}	G_{IIc}	Fracture Energy Ratio
0.8	26.88	34.704	0.168	0.616	0.8
			0.21	0.77	1
			0.252	0.924	1.2
1	33.6	43.38	0.168	0.616	0.8
			0.21	0.77	1
			0.252	0.924	1.2
1.2	40.32	52.056	0.168	0.616	0.8
			0.21	0.77	1
			0.252	0.924	1.2
1.5	50.4	65.07	0.168	0.616	0.8
			0.21	0.77	1
			0.252	0.924	1.2

Table 5.2: Parametric Study with constant delamination properties

The migration location as a function of the strength ratio is presented in Figure 5.17. The three curves correspond to each fracture energy ratio. When the strength of the matrix is 1.5 times the interlaminar strength, the location of migration does not change with an increase in the matrix fracture energy and the migration occurs at a distance of 23.7mm.

The earliest migration location is obtained for both strength ratios of 0.8 and 1 when the fracture energy ratios are 0.8 and 1. A lower fracture energy does not seem to promote migration. For the fracture energy ratios of 0.8 and 1, an increase in the matrix strength delays the migration. In the case of strengths ratios of 0.8 and 1, the difference in the migration location is 0.5, which is again an offset of element. However, for a strength ratio of 1.2, the migration is offset by almost 1.5mm, which is equivalent to three elements.

The migration in the specimen for strength ratios of 0.8, 1, and 1,2 are presented for the fracture energy ratio of 0.8 in the following Figure 5.18. It can be seen that migration occurs at the same location for strength ratios of 0.8 and 1, however, migration attempts occur much earlier for these cases. This is represented by the degraded elements present through the thickness. Migration does not occur through these elements despite lower matrix fracture energy. These matrix cracks are arrested near the top interface thus delaying migration. Another aspect that can be observed is, that the crack spacing remains the same for all three strength ratios, however, the location where the crack is initiated is offset by 2 elements for the strength ratio of 1.2. The first migration attempt for a strength ratio occurs at a distance of 17.2mm, however, the migration is delayed due to delamination being more energetically favorable and since the crack spacing is constantly 3-3.5mm, the migration occurs at distance 20.2mm. In all cases, migration appears to be a function of this crack spacing. Note that no non-default crack spacing was introduced in the modeling step, however, the strength-insensitive crack spacing seems to determine where the migration is favorable. If a certain matrix crack does not degrade fully, the migration is delayed by 6 elements. The location where the first matrix crack with correct orientation appears to determine where the subsequent matrix cracks will initiate. However, a lower matrix crack allows initiation cracks through the thickness at a lower load while a higher matrix strength restricts the number of crack nucleation sites through the thickness. This finding seems to rule out the possibility of migration being insensitive to matrix strength.

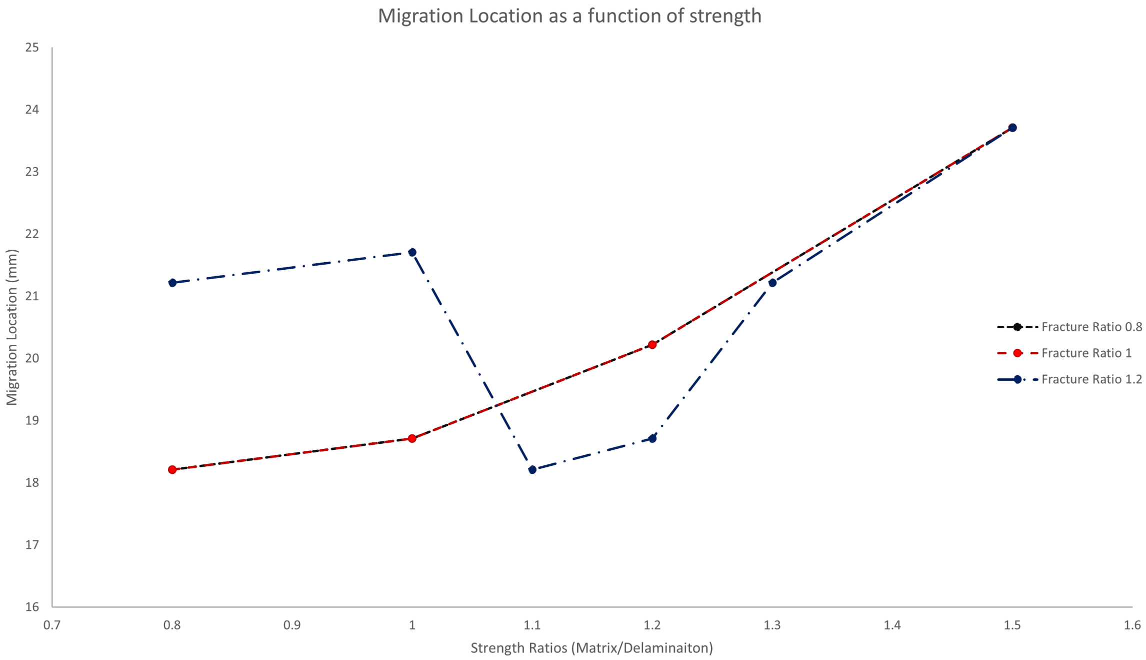

Figure 5.17: Effect of matrix strength and fracture energy on the location of migration

Since the fracture energy ratio of 0.8 and 1 result in the same trend for the location where migration is predicted, a higher matrix fracture energy was considered. The ratio of matrix fracture energy to delamination fracture energy of 1.2 was simulated for the four strength ratios. The hypothesis was that a higher fracture energy would delay the migration significantly for all strength ratios. In Figure 5.17, one can observe that this hypothesis holds true only for strength ratios of 0.8 and 1. For the strength ratio of 1.2, the migration was predicted at 18.7mm. Assuming this simulation resulted in an outlier, strength ratios of 1.1 and 1.3 were also tested. The migration for these cases occurred at a distance of 18.2 and 21.2mm respectively. The migration location for the fracture ratio of 1.1 was offset by 0.5mm when compared to the location for the ratio of 1.2 which is equivalent to one element length. The offset for the ratio of 1.3 is 2.5mm which is almost equivalent to the crack spacing. This finding again reinforces the notion that the crack spacing determines the location where migration is likely to occur after a failed attempt. This crack spacing appears to be a mesh-dependent parameter that could not be controlled. The location of the first matrix crack depends on the matrix strength, however, subsequent matrix cracks occur at discrete distances equivalent to the crack spacing. Further mesh refinement would be required to determine whether the crack spacing is mesh-dependent.

5.6 Discussion

In the first section of this chapter, a detailed mesh convergence study for solid elements was conducted to ensure accuracy in predicting the peak load response. From this study,

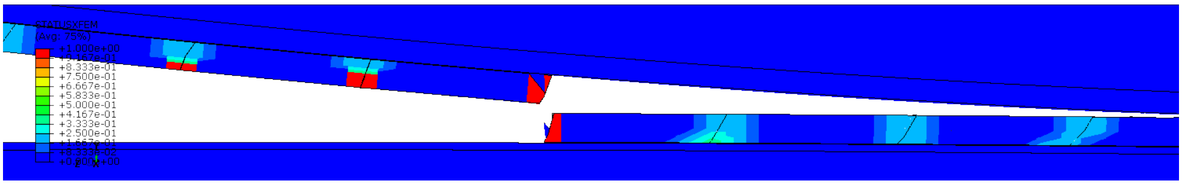

(a) Strength Ratio = 0.8

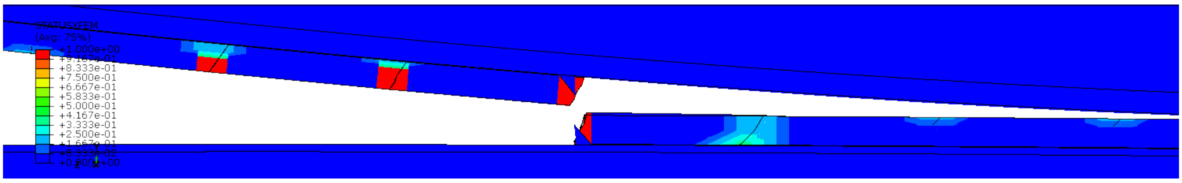

(b) Strength Ratio = 1

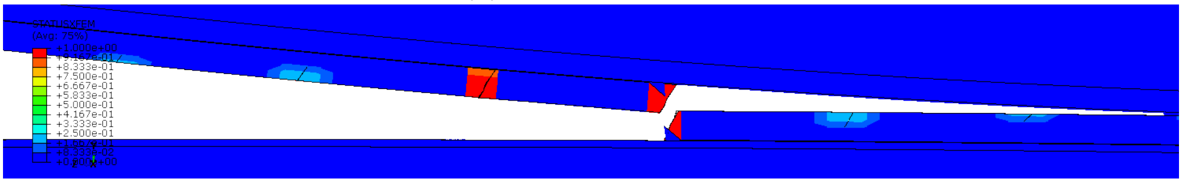

(c) Strength Ratio = 1.2

Figure 5.18: Crack Migration location for each case

an element length of 0.5mm was selected, as it met the convergence criteria effectively. The material used in the study, IM7/8552, was found to have a cohesive zone length of 0.56mm, which necessitated the use of a highly refined cohesive mesh to model delamination. However, the fine mesh significantly increased computational costs, with the simulation time extending to approximately 70 hours using 20 computational cores. Despite these efforts, the model failed to predict crack migration, even though material properties from existing literature were applied. As a result, it became necessary to examine how the cohesive zone parameters influenced the model's ability to predict migration. To address this, a study on the effect of cohesive zone length on delamination was carried out. Three different cohesive zone lengths were considered: 0.57mm (close to the material's cohesive zone), 0.75mm, and 1.5mm. Simulations incorporating these three cohesive zone lengths were performed, revealing that migration was successfully predicted for the 0.75mm case under the applied load conditions. However, in all three cases, migration attempts were observed, though they occurred at distances 2-3 times greater than those recorded in experiments (8-9mm).

Another important observation was that no matrix degradation was found near the pre-crack front, which was essential for initiating the crack migration closer to the actual crack tip. This led to the conclusion that a finer mesh would be required to accurately capture matrix crack growth across the width of the specimen, particularly near the pre-crack front. However, since further mesh refinement was computationally prohibitive, the strategy shifted toward reducing the matrix strength. This adjustment was intended to modify the matrix's cohesive zone length, allowing the model to achieve sufficient refinement in the cohesive zone without an excessively fine mesh. The subsequent simulations focused on evaluating the impact of reduced matrix strength on migration. It was discovered that lowering the matrix strength encouraged crack migration at a much smaller distance, bringing the predicted location closer to experimental observations. Despite this improvement, the migration location remained approximately 2-3 times farther than what was observed in physical experiments. However, for lower matrix strengths, the distance between the migration points matched the crack spacing. Another issue encountered during the simulations was the prediction of complex crack profiles and incorrect degradation of matrix cracks, particularly when using full integration elements with reduced matrix strength. This led to the formation of incorrectly oriented cracks in the matrix. Switching to reduced integration elements appeared to alleviate this problem, but the predicted location of crack migration still remained inaccurate.

Subsequent parametric studies explored the relationship between matrix strength and migration location. A clear monotonic delay in migration was observed as the matrix strength increased, provided that the matrix fracture energy ratio was kept constant with respect to delamination. However, when higher matrix fracture energies were used, this monotonic trend no longer held, suggesting that the interaction between fracture energy and matrix strength might be more complex than initially anticipated. Throughout these studies, the crack spacing remained constant, and migration location seemed to depend on this parameter. It was determined that the crack spacing was a numerical artifact, likely due to the mesh configuration, as no specific crack spacing setting was applied within the numerical model. This suggests that crack spacing is influenced by the discretization of the model, requiring further investigation with finer mesh configurations to better understand its impact.

Despite these challenges, the combination of the XFEM-Cohesive Elements (XFEM-CE) method captured the interaction between matrix cracking and delamination sufficiently well. This indicates that the method is robust enough to simulate complex damage phenomena and is suitable for application at a structural level. However, the effect of cohesive parameters on migration and the crack spacing artifacts remains an area for improvement.

Chapter 6

Skin-stiffener - Modeling

The capability of the XFEM-CE method to capture the interaction between matrix cracks and delamination was demonstrated through a series of simulations of delamination migration tests in the previous chapter. These simulations also examined how the cohesive parameters of the matrix crack and delamination influenced the migration location. For thermoset matrix materials, the cohesive zone was as small as 0.5 mm, leading to high computational costs when refining the mesh. To address this, an alternative strategy was employed: adapting the cohesive zone by reducing the material strength. However, thermoplastic composite materials, known for their significantly higher fracture toughness, result in cohesive zones almost 3 times larger than that of thermoset composites. This allows for the use of a relatively coarse mesh while still maintaining experimentally determined material properties.

Given that the XFEM-CE approach can predict the tendency for crack migration, the method was extended to simulate migration in a stiffened panel subjected to out-of-plane loading. In regions where migration is expected, solid elements as small as one-third the size of the cohesive zone are required. To manage this, a global-local modeling approach was adopted. This chapter details the numerical model of the stiffened panel and the implementation of this approach.

6.1 Single Stiffener Panel

The panel used in this study is similar to the skin-stiffener studied in [27]. However, only a single stiffener is modeled to study the crack propagation at the skin-stiffener interface. The panel geometry is not revealed to maintain confidentiality. The skin is a quasi-isotropic laminate with 19 plies while the web layup consists of 18 plies. The short fiber filler material connects the laminates of the stringer and skin, resulting in a butt-joint configuration as depicted in Figure 6.1. The damage at the skin-stiffener interface was introduced by inserting a PTFE insert at the mid-length of the stringer during the consolidation process. Since this method introduces a blunt crack tip, a sharp crack tip was generated through an out-of-plane indentation on the skin resulting in a longer and sharper crack representative of damages

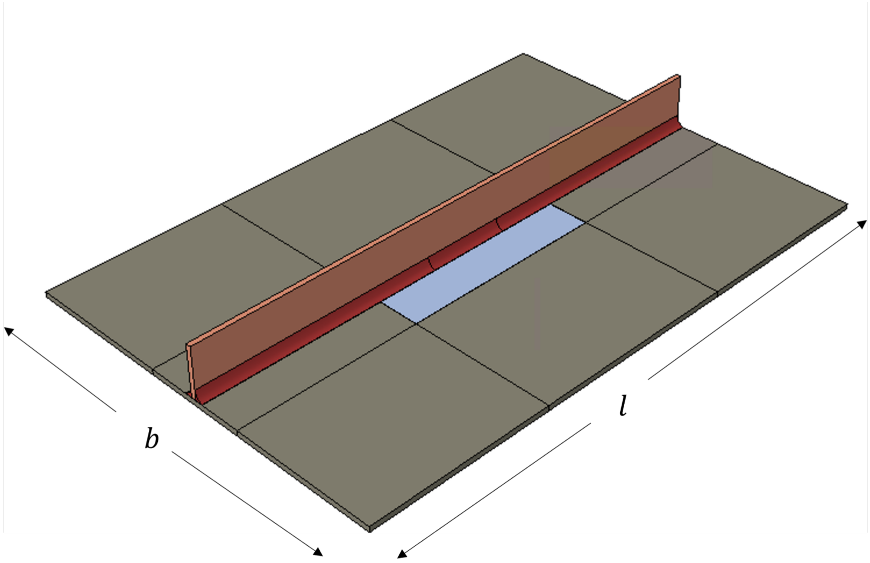

Figure 6.1: Panel Geometry and Dimensions

in an airframe during service. This damaged panel was subjected to compressive loads to evaluate its load-bearing capacity in the post-buckled regime. However, C-scans of the skin before post-buckling tests reveal delaminations within the skin underneath the skin-stiffener interface. It may be possible that the indentation process introduced delaminations in the skin. C-scans of the skin during the post-buckling tests have also shown this delamination propagates further into the skin along the panel length while no crack growth is observed at the skin-stiffener interface. It may be essential to account for such damage within the skin in the numerical simulations of the panel.

In this chapter, the model for the simulation of the out-of-plane indentation will be presented. The objective is to verify whether the delamination in the skin is a consequence of crack migration or if it is just the failure of a weak ply interface in the skin. Therefore, a simulation with just cohesive elements at the skin-stiffener and ply interfaces were conducted without XFEM. This was done to determine whether delaminations are observed in the skin without any matrix cracks in the plies. The subsequent simulations included XFEM for the ply elements. The modeling approach for these simulations is presented in detail in the following sections.

6.2 Panel Modeling Approach

To predict delamination within the skin, the plies were modeled separately. Given the large geometry, it would not be feasible to model the plies individually for the entire length and width of the panel. Therefore, a global-local approach was followed, where the outer +/-45° plies were modeled separately as done in [46]. The material for the global model of the panel was specified using a composite layup definition. Two models 1 and 2 were created using the approach as shown in Figure 6.2a and Figure 6.2b. The skin region in blue in both models was modeled using continuum shells with composite layup definition. The filler material and

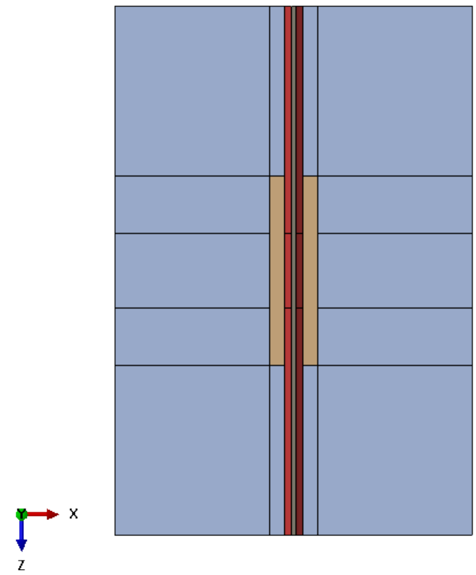

(a) Panel Model 1

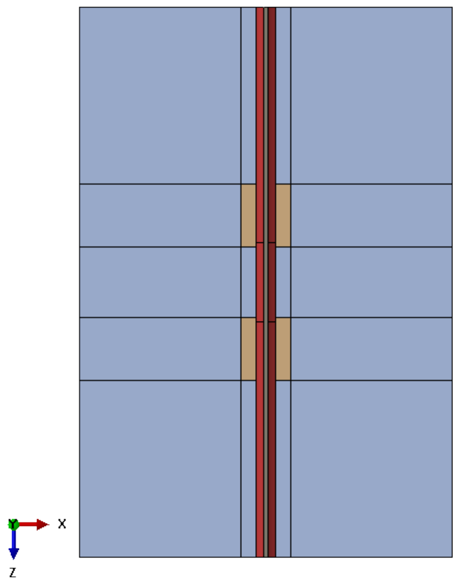

(b) Panel Model 2

Figure 6.2: Panel Models

the web region are the same in both models. The local model is located at the central region in Panel Model 1 shown in Figure 6.2a. Panel Model 2 Figure 6.2b was created by modeling the region beneath the PTFE insert using composite layup definition and the local models are placed only near the pre-crack fronts. The length of the artificial crack is also not specified for confidentiality. The distance between the local regions in Panel Model 2 was less than the pre-crack length to prevent unrealistic delamination at the ply interface (shown in the results chapter).

The first two plies in the local model are meshed using solid elements. The lower sublaminate of 17 plies is modeled as a separate part using a continuum shell elements and composite layup definition. The local region was assembled by placing the two solid plies on top of the sublaminate and these parts are placed inside the global shell model. Cohesive elements were placed between the skin-filler interface and between the +/-45° solid plies. No cohesive elements were placed in the 40mm pre-crack region at the skin-filler interface. The detailed view of this local region can be seen in the cross-section view depicted in Figure 6.3. Tie constraints were defined between all the connecting surfaces. Tie constraints were also used to connect the local model to the global model as done in [46].

6.3 Material Properties

The thermoplastic skin was manufactured using AS4D/PEKK material. The elastic properties of this material are taken from [27] and [42]. The material properties are given in Table 6.1 below. The transverse strengths Y_t and Y_c required for the LaRC05 criterion along with the mode I and mode II fracture energies were taken from [48]. The BK criterion was used for damage evolution and the BK exponent of 2.9 was also taken from the previous reference.

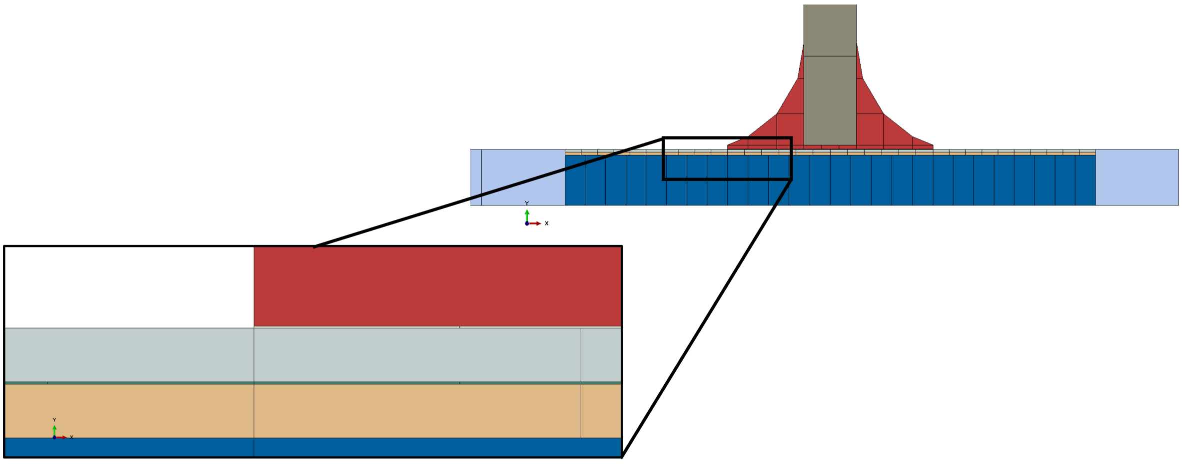

Figure 6.3: Cross-section with details of high-fidelity model

Elastic Property	Value	Units	Strengths	Value	Units
E1	126100	MPa	Xt	2559	MPa
E2	11200	MPa	Xc	1575	MPa
E3	11200	MPa	Yt	87	MPa
μ_{12}	0.30	-	Yc	284	MPa
μ_{13}	0.30	-	Sl	90	MPa
G12	5460	MPa	GIc	1.12	KJ/m^3
G13	5460	MPa	GIIc	2.35	KJ/m^3
G23	3700	MPa	BK Power	2.9	
μ_{23}	0.45	-	K_{normal},K_{shear}	4e+6, 1.9e+6	N/mm^3

Table 6.1: AS4D-PEKK Elastic Properties, Strengths and Fracture Energies

Assuming the ply interface properties are the same as the matrix properties, the strength and fracture energies for the cohesive elements in the ply interface were assigned the same values.

For the skin-filler interface, the fracture energy is specified in [27] although, strength values are not given. It was shown in the previous section that in the presence of a pre-crack the strength can be modified based on the desired element length assuming three cohesive elements are present in the cohesive zone. In this simulation three elements of 0.5mm in the cohesive zone result in a cohesive zone length of 1.5mm. This is equivalent to the cohesive zone length of the AS4D-PEKK determined material using the properties presented in the table above. The normal and shear strengths obtained assuming a cohesive zone length of 1.5mm were 95.1 MPa and 110.73MPa. This is similar to the strength used in [42]. The cohesive parameters used for cohesive elements at this skin-filler interface are presented in the following Table 6.2.

Property	Value	Units
G_I	1.4	kJ/m^3
G_{II}	1.9	kJ/m^3
BK	2.3	
S_{normal},S_{shear}	95.1, 110.73	MPa
K_{normal},K_{shear}	2e+5, 1.6e+5	N/mm^3

Table 6.2: Skin-stiffener interface properties

The penalty stiffness for the cohesive elements is determined using the following expression recommended in [30]. Here, h refers to the substrate thickness and E_33 is the out-of-plane elastic modulus of the substrate. Here E_33 is assumed to be the transverse elastic modulus specified in Table 6.1. For the skin-stiffener interface, the h is assumed to be the nominal thickness of the skin which is 2.62mm whereas the h is the ply thickness for the ply interface, which is 0.138mm. This approach results in the normal and shear penalty stiffness (K$_{normal}$,K$_{shear}$) presented in Table 6.1 and Table 6.2.

$$K_{normal} = 50\frac{E_{33}}{h}$$

$$K_{shear} = K_{normal}\frac{G_{IC}}{G_{IIC}}\left(\frac{S_{shear}}{S_{normal}}\right)^2$$

6.4 Mesh

The skin and the web are meshed with continuum shell elements of length 4mm. The solid plies are meshed with reduced integration solid elements (C3D8R) along with stiffness hourglass control. The element size for the solid elements is 1mm, which results in an aspect ratio of 7.2. The lower plies part in the high-fidelity region is meshed with 1mm continuum shell elements. Since the cohesive zone length is almost 1.5mm, cohesive elements placed at the ply interface and skin-stiffener interface are meshed with 0.5mm element length. A viscosity of 1e-6 is defined for the cohesive section to enable convergence during the damage process. In the simulation with XFEM and cohesive elements, the solid element length in the plies used was 0.5mm and the cohesive element length used was 0.25mm.

The filler material was meshed with solid elements with incompatible modes (C3D8I) to capture the bending behavior. However additional partitions were included in the filler to improve the mesh quality as shown in Figure 6.4. A refined mesh at the foot of the filler was used (Figure 6.5a) to account for deformations in the filler which would arise due to the panel curvature during the out-of-plane displacement. In Figure 6.5b, the mesh is refined near the delamination to capture the stress concentrations arising at the crack tip. In this region, the element size is approximately 1mm and towards the end, the element size is 2mm. The worst aspect ratio in this mesh is around 7, which satisfies the guidelines that recommend 10 as the maximum aspect ratio.

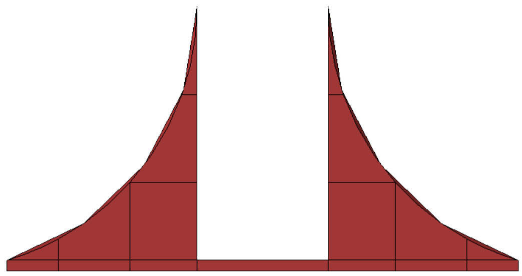

Figure 6.4: Partitions in Filler Material

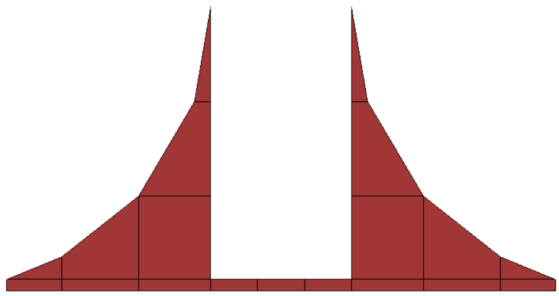

(a) Filler Mesh Front View

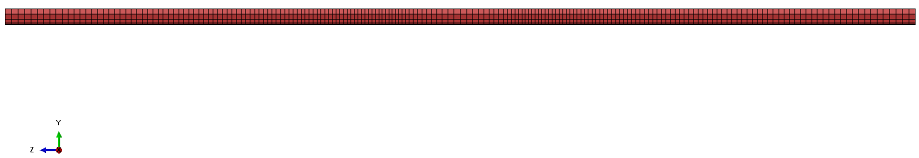

(b) Filler Mesh Sideview

Figure 6.5: Filler Mesh

6.5 Loads and Boundary conditions

As mentioned earlier, the panel is indented or subjected to an out-of-plane displacement load such that the artificial crack is extended. The original specimen was subjected to a three-point bending load with the skin being simply supported. Moreover, the out-of-plane load is introduced very close to the filler through a cross-head pushing the skin away from the stiffener on either side of the filler material. This load is distributed over a region that is as long as the artificial crack. This would likely result in a mode I crack opening initially and the evolution would depend on the deformed configuration of the panel and subsequent damage if predicted.

In the FE model, two rows of nodes were selected on the skin and lower plies to simulate the simply-supported boundary condition. The out-of-plane displacement is constrained (U_2=0)on these nodes. To ensure a simply supported boundary condition, the longitudinal displacement is constrained (U_3=0) on one row of the support nodes. Additionally, the transverse displacement U_1=0 is applied on the skin as shown in Figure 6.6 to constrain the lateral displacement of the panel. For the load application nodes were selected on the top surface of the skin such that the load can be applied close to the filler material as shown in Figure 6.7. A displacement of 0.5mm is applied on these nodes such that the out-of-plane deformation of the skin is away from the stiffener enabling the crack opening at the skin-stiffener interface.

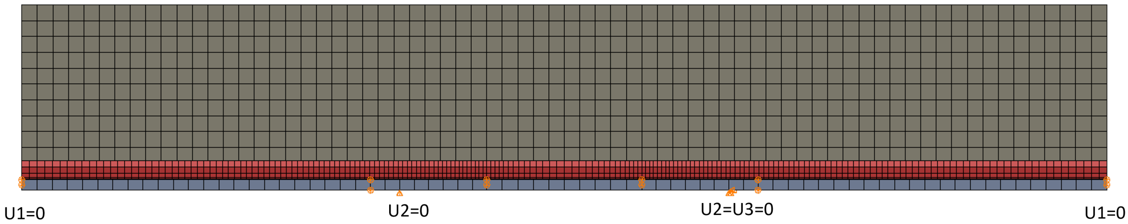

Figure 6.6: Panel Simply Supported Boundary Conditions

6.6 Non-Linear Solution Control and Additional Parameters

The full Newton-Rapshon solution procedure was used for the non-linear simulation. The non-default time incrementation parameters used in the crack migration simulation were specified here to enable convergence of each increment and ensure completion of the simulations. The minimum and maximum increments are 1e-15 and 0.1. The MULTICRACKS keyword was included to allow cracks to initiate multiple XFEM cracks in the matrix. Since the simulations with XFEM suffered from convergence difficulties initially, the effect of automatic stabilization was also included in the solution procedure. This would include damping of a factor term to the global equilibrium equation and enable convergence. The default damping factor of 2e-4 was used in the simulations.

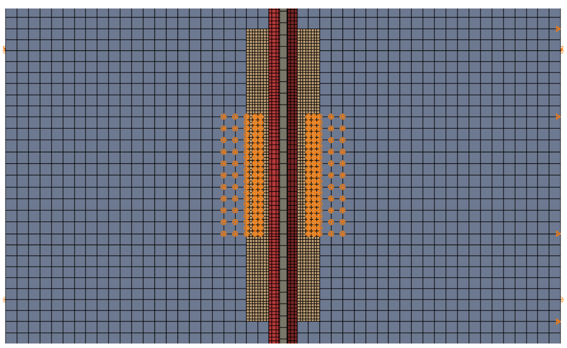

(a) Load on Panel Model 1

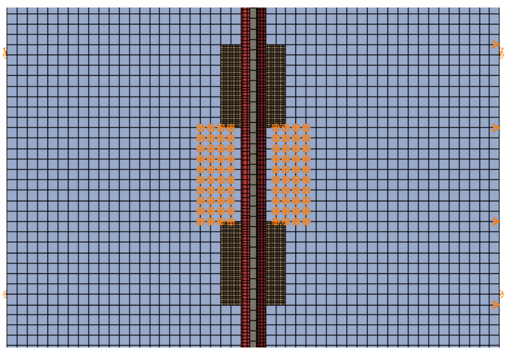

(b) Load on Panel Model 2

Figure 6.7: Load Application

6.7 Studies conducted with the panel

First, the linear response of the models was studied and compared with a model that does not contain the local refined region. The model without the local refinement is also used to determine the out-of-plane displacement required to extend the artificial crack to a length of 70mm since experimental data was not available. The subsequent simulations are carried out using the model with local refinement. These simulations only predicted delaminations and no matrix cracks were initiated since XFEM was not activated. The objective was to determine whether delamination in the skin is a consequence of migration or high interlaminar stresses. Following this, the solid elements of the outer two plies were enriched. The results obtained from these simulations are presented in the following chapter.

Chapter 7

Skin-stiffener - Results

This chapter presents the results of the skin-stiffener simulation. The first section focuses on linear elastic simulations of the panel, excluding non-linearities such as damage, with the goal of comparing the stiffness differences among the various modeling approaches. The subsequent section discusses simulations of skin-stiffener separation, where cohesive elements are introduced at the skin-filler interface. These simulations are used to establish the force response of the stiffened panel, serving as a benchmark for the subsequent analyses.

Following this, the chapter presents results from two simulations that incorporate delamination within the skin. These simulations aim to determine whether the observed delamination is driven by local peeling stresses or is an inherent consequence of the applied loading conditions. Finally, the outcomes of a model that includes enriched elements for XFEM cracks will be discussed, providing insights into the complex interactions between matrix cracks and delamination in the stiffened panel.

7.1 Linear Elastic Response

Four levels of model complexities are considered in this section. Model 1 comprises of the skin, filler, and web-connected through mesh tie constraints. The filler and skin are not tied in the region where the PTFE insert is present. The second case includes the local model where the outer 45/-45 plies and the lower sublaminate and no cohesive elements are used in the model. All the parts are connected through tie constraints. The third model is similar to the second case, however cohesive elements are included at the filler-skin interface and 45/-45 ply interface in the local model. Damage parameters are not defined for the cohesive elements to allow the models to deform only in the linear elastic regime. The fourth model utilizes the same global-local model, however, cohesive elements are used only at the skin-filler interface whereas the 45/-45 ply interface does not contain any cohesive elements.

The load response of the four models is shown in Figure 7.1. The stiffness of the panel for the applied load is higher for Model 1, where the skin is entirely meshed using continuum shell elements. The stiffness of the other models is considerably lower compared to Model 1.

Case	Model	Details
1	Model-1	Shell skin, no CE in skin-filler interface
2	Model-2	Local model, no CEs in skin and ply interface
3	Model-3	Local model, includes CEs in both interfaces
4	Model-4	Local, CE only between skin and filler

Table 7.1: Details of the models tested

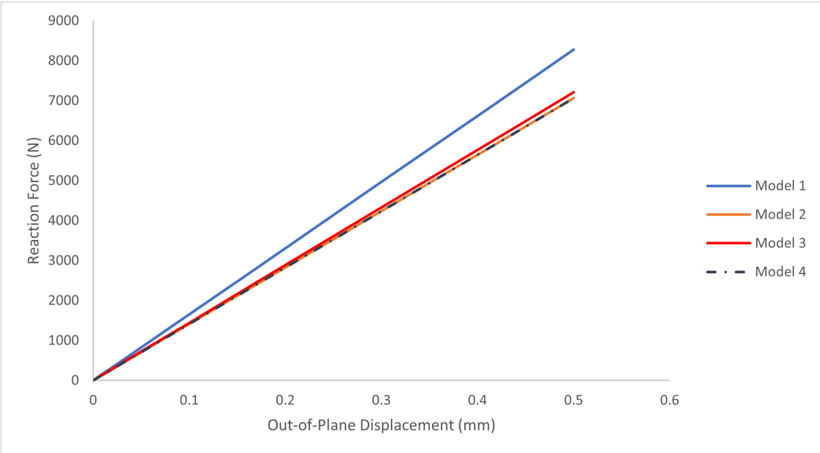

Figure 7.1: Reaction forces

The stiffness of Models 2 and 3 are not different significantly, however, the effect of including cohesive elements at two interfaces appears to stiffen the response of the structure. The response of models 2 and 4 is similar indicating that the presence of cohesive elements at the ply interface has an influence the response of the model. The local refinement of the panel introduced some degree of compliance into the structure. However, a comparison with experimental results would be required to validate the modeling approaches. The deformed configuration of the panel is presented in Figure 7.2. The deformation magnitude is higher in the middle of the panel close to the filler material, where the load is applied. The effect of the simply supported boundary conditions can be seen in the deformed configuration. The out-of-plane loads on the panel is aimed at extending the crack at the filler interface. The following sections present the response of the panel when damage is included in the model.

7.2 Crack extension at skin-filler interface

This section includes cohesive elements at the skin-filler interface in Model 1. Cohesive elements are not placed in the pre-crack region. The out-of-plane displacement of 0.5mm is applied and the response of the panel is obtained through the simulation.

The force response of the skin-stiffener is plotted in Figure 7.3. The panel seems to respond linearly up to a displacement of 0.36mm where the peak reaction force is 3.8kN. Following this peak, a significant drop in the load is observed followed by a series of unstable drops in the load and a stable increase in the reaction forces. This response of the reaction force is accompanied by damage in the cohesive elements. The final damaged state of this interface

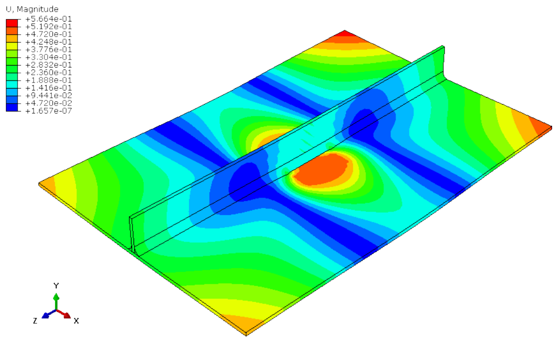

Figure 7.2: Deformed Configuration of Model 1

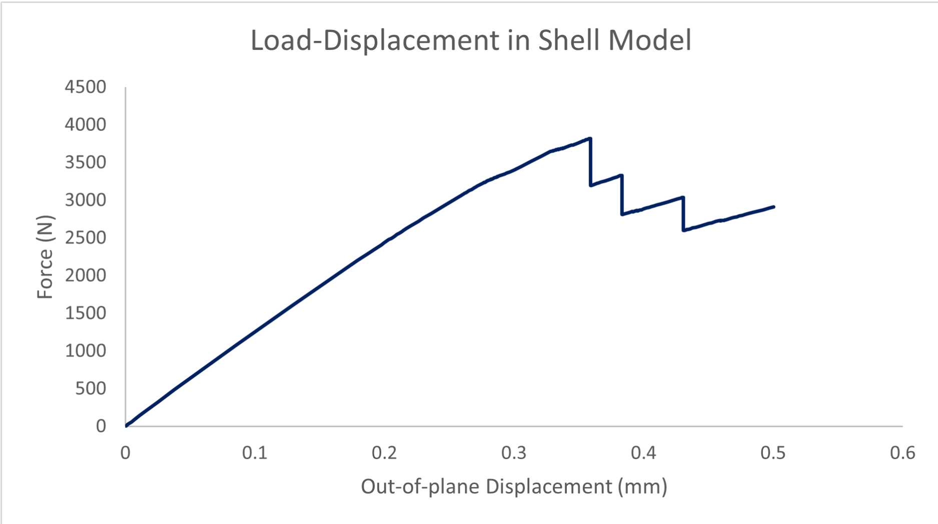

Figure 7.3: Force response of skin meshed with shell elements

is shown in Figure 7.4a. The elements highlighted in red are elements where the energy has not been dissipated and the failed elements are transparent (highlighted in pink). The damage region is more concentrated in the middle section of the interface, likely due to the increased stiffness of the web and filler material in this area. The higher stiffness in the central region amplifies stress concentrations, leading to more pronounced damage compared to the surrounding areas. The crack extends to 8.5mm on both sides resulting in the pre-crack of 40mm extending to a length of 57mm. The crack extension is predominantly mode I as shown in Figure 7.4b. Experimental data regarding this step is not available for verification or validation, however, the result of this simulation provides some details regarding the nature of crack propagation and the response of the load that could be expected from the simulations with local refinement.

7.3 Ply Delamination Modeling

After establishing the load response characteristics of the skin-stiffener panel, simulations were performed using a local model without the inclusion of XFEM to ensure that delaminations

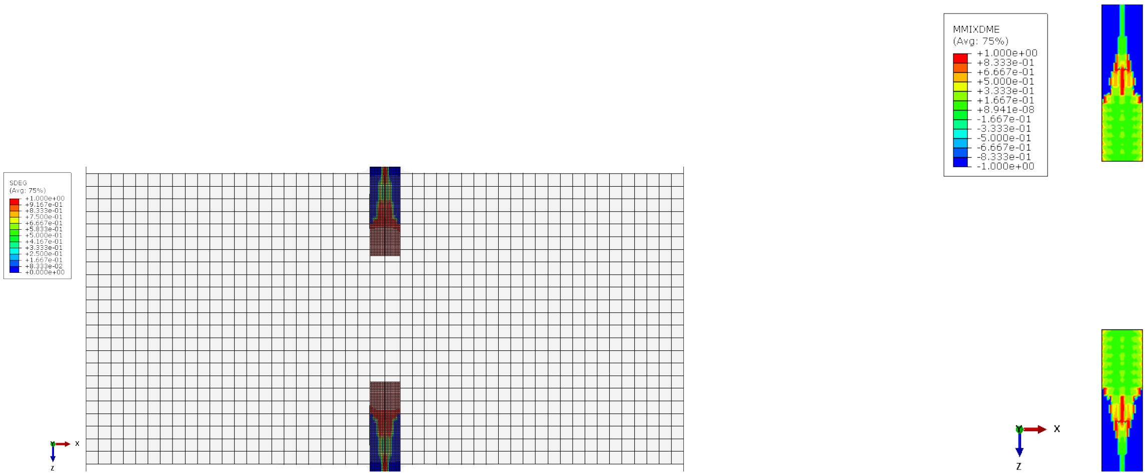

(a) **(b)**

Figure 7.4: (a)Damaged cohesive elements in skin-filler interface (b)Mode Mix ratio of the damage in the interface

did not arise from high interlaminar stresses at the ply interfaces. In these models, a viscosity of 1e-6 was applied to the cohesive elements, and a damping factor of 2e-4 was introduced through automatic stabilization in the step definition. As detailed in the previous chapter, the dimensions of the local model were specified, with particular emphasis on ensuring that the distance between the local regions in Panel Model 2 was shorter than the pre-crack length. In this section, results for the same model are presented, with the distance set equal to the pre-crack length as well.

The damage in the skin-filler interface for Panel Model 1 is shown in Figure 7.5a. The crack extension predicted by this model was 6mm, which results in a total length of 46mm. The damage in the 45/-45 ply interface can be seen in Figure 7.5b. Damaged regions are localized and coincide with the load application points. The maximum damage variable is 0.96 which indicates that there is no interlaminar failure in this region. Further mesh refinement could reveal whether damage is observed in this region. However, the model does not predict any delamination in the region underneath the filler material, which rules out the possibility of delamination in the skin occurring due to high interlaminar stresses.

The damage predicted in Panel model 2 with the distance between the local models set equal to the pre-crack is presented in Figure 7.6c and Figure 7.6a. This model predicts lesser damage in the skin-filler interface with almost no crack extension and failure occurs only in a few elements close to the crack front. However, this model predicts significant delamination in the 45/-45 interface elements, shown in Figure 7.6c.

When the distance between the local model is reduced such that the pre-crack front lies within the high-fidelity region, the damage predicted in the skin-filler interface is significantly longer than what was observed earlier. The damage at this interface is shown in Figure 7.6b, and the crack length is 47mm. Moreover, this model does not predict any delamination in the 45/-45 interface elements and the failure index in this interface is much less than 1 indicating no sign of delamination onset, shown in Figure 7.6d.

The extensive delamination predicted by the model with the coincident high-fidelity regions

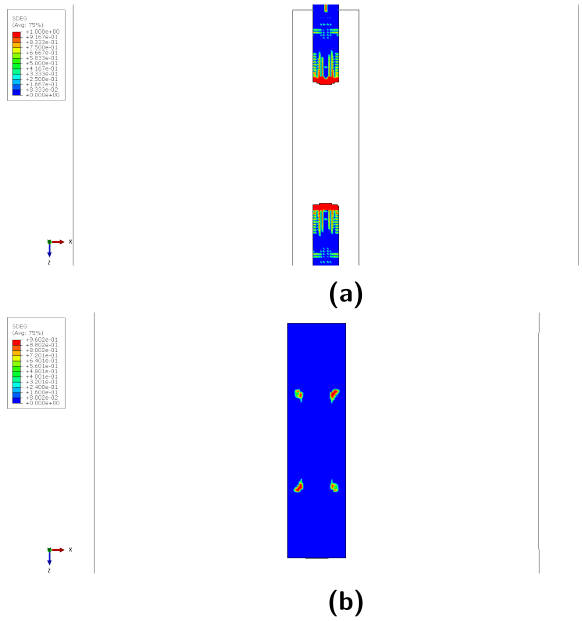

Figure 7.5: (a)Damaged cohesive elements in skin-filler interface (b)Damage in 45/-45 interface

could have been a consequence of the modeling strategy. Mesh ties were used to constrain the degrees of freedom of the local model to the global skin model. However, significant peeling stresses developed in the cohesive elements placed at the ply interfaces. The large deformations of the cohesive elements closer to this region can be seen in the deformed configuration of the high-fidelity section in Figure 7.7a.

However, these simulations present an issue with the force response shown in Figure 7.8: no load drop is observed following the onset of damage. Instead, the load increases as soon as damage initiates and continues to rise to unrealistic levels. The force response is only presented up to a displacement of 0.35 mm, as this is the point where unstable crack growth was observed in the skin-stiffener model meshed with shell elements. This response is unrealistic and inconsistent with expected behavior in a damage simulation.

To investigate the issue, the various components of energy were analyzed, revealing that the static dissipation energy associated with automatic stabilization increased exponentially after damage initiation. This indicates that the default damping factor used in the automatic stabilization might not be appropriate for this model, contributing to the unrealistic force response. As a result, an alternative approach will be needed to address convergence issues without relying on default stabilization parameters, ensuring more accurate damage representation in the simulations. Therefore. a parametric study on the viscosity in cohesive elements was carried out and the results are presented in the following section.

7.4 Parametric Study: Viscosity

In this section, the effect of viscosity is considered for the simulation of Panel Model 2. Automatic stabilization is useful for problems that contain local instabilities such as material

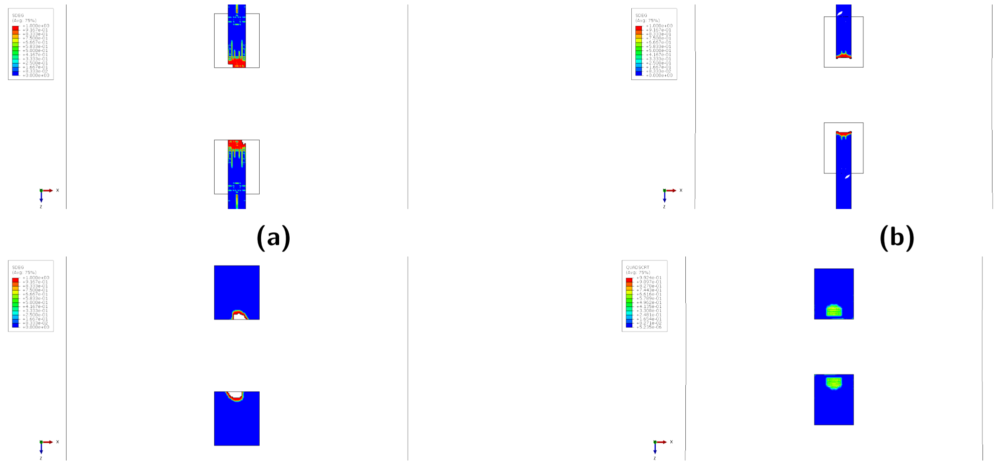

(a) (b) (c) (d)

Figure 7.6: (a)Damaged cohesive elements in skin-filler interface in Panel Model 2 with the distance between local regions equal to pre-crack length (b)Damaged cohesive elements in skin-filler interface in Panel Model 2 with the reduced distance between local models (c) Delamination in 45/-45 interface in Panel Model 2 with the distance between local regions equal to pre-crack length (d) Damaged cohesive elements in skin-filler interface in Panel Model 2 with the reduced distance between local models

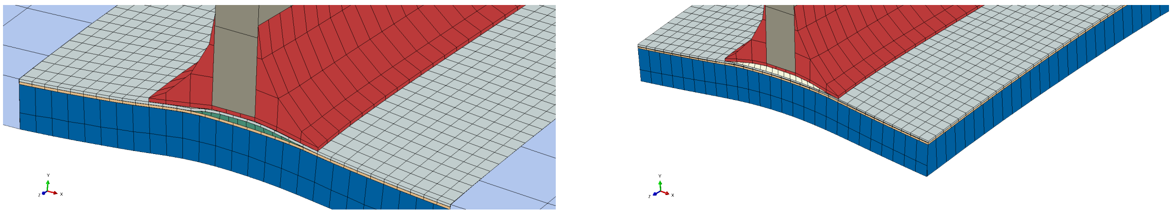

(a) (b)

Figure 7.7: (a)Peeling in ply interface cohesive elements (b)No delamination in skin observed after the distance between local model was reduced

softening [17]. However, in the current scenario instability such as negative stiffness is observed during the unstable crack growth when multiple cohesive elements fail. Therefore, increasing the viscosity was considered a reasonable approach. Three values of viscosity, 1e-6, 1e-5, and 1e-4, are considered for the cohesive elements.

The load response for the three viscosity values is presented in Figure 7.10, compared to the load response of the shell model discussed earlier. Introducing a viscosity of 1e-4 facilitated convergence and allowed the simulation to complete in a shorter duration. The load response for this viscosity shows load drops at various points throughout the loading sequence. However, a distinct unstable drop in the load was not observed, likely due to the significant viscous forces introduced during unstable events, such as the failure of multiple cohesive elements. Despite this, the damage sequence aligns closely with that observed in the shell model.

When a lower viscosity of 1e-6 is specified, convergence issues arise, with the simulation exhibiting increment sizes in the range of 1e-5 to 1e-7 as it progresses. This suggests that while lower viscosities might offer more accurate damage progression, they lead to computational

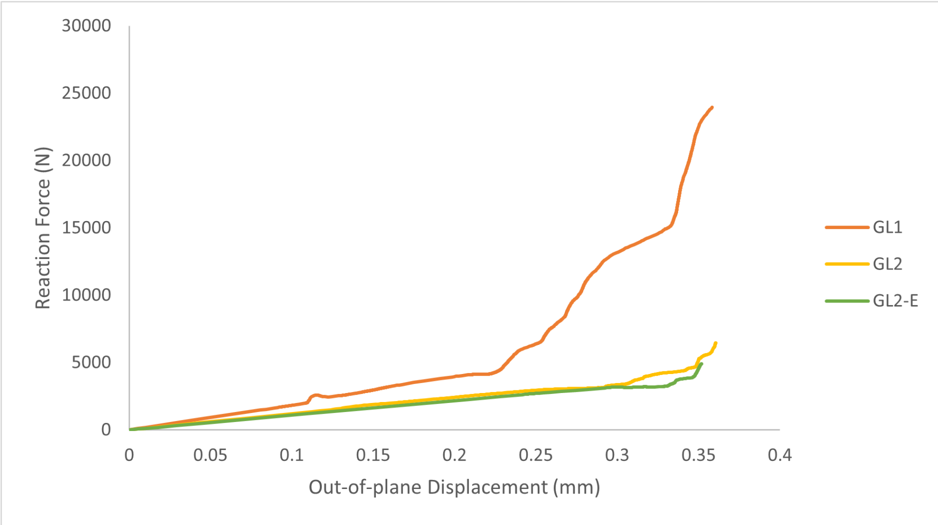

Figure 7.8: Reaction force for the above three models

difficulties.

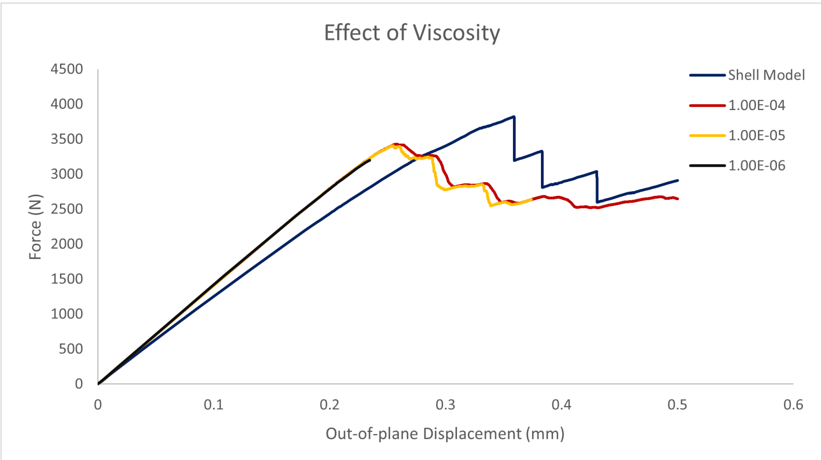

Figure 7.9: Force response with different viscosities

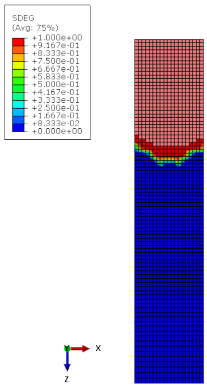

Figure 7.10: Crack extension

The simulation with a viscosity of 1e-4 predicts a crack length extension of 68mm, which is much longer than the length predicted by the shell model by 12mm. The failed cohesive elements shown in Figure 7.10 depict the extension of the pre-crack only on one side since the crack growth is symmetric on both ends.

This study demonstrates that a sufficiently high viscosity is necessary to achieve faster simulation completion without compromising accuracy. While reducing the viscosity did not significantly alter the force response, it introduced convergence issues and slowed down the simulation process. The results indicate that higher viscosity effectively stabilizes the simulation, allowing for timely completion, while still providing a force response and damage sequence consistent with lower viscosity models. In the following simulations, enriched elements were incorporated into the model to account for matrix cracking, and a viscosity of was 1e-5 applied for all cracks.

7.5 Combined XFEM-CE simulations

In this final section of the results for the skin-stiffener simulations, the outcomes of simulations conducted using the combination of XFEM and standard cohesive elements are presented. The previous results established critical model requirements, including viscosity and the necessary out-of-plane displacement for effective crack extension. For this simulation, where XFEM cohesive segments will be utilized to model matrix cracks, the mesh of the components was refined. Specifically, shell elements measuring 2 mm were employed near the pre-crack in the skin, while the solid elements of the 45° and -45° plies were reduced to 0.5 mm to ensure sufficient refinement in the cohesive zone.

To capture crack migration with adequate precision, the cohesive elements were further refined to 0.25 mm, even though 0.5 mm would have sufficed for cohesive zone requirements. Material properties, as detailed in the previous chapter, were applied to the corresponding components, and all remaining model parameters were kept consistent with earlier simulations.

The delamination at the skin-filler interface is illustrated in Figure 7.11. The crack extension predominantly occurs near the edges, extending up to 11.25 mm on one side. The maximum crack length observed reaches 62.5 mm, factoring in the extensions at the edges. However, a significant area of cohesive elements remains undamaged in the central region, and the crack profile differs from those seen in previous cases.

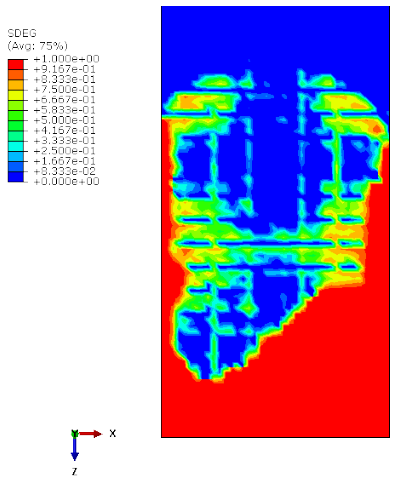

Figure 7.11: Damage at the skin-filler interface

The matrix cracks and delamination in the 45°/-45° interface are illustrated in Figure 7.13 and Figure 7.12. The extensive damaged area observed in the 45°/-45° interface indicates substantial delamination within the skin. Additionally, Figure 7.13 reveals a significant number of matrix cracks in the 45° ply. The delamination observed at the ply interface occurs behind the first matrix crack, as shown in Figure 7.14. This suggests that the degradation of the matrix crack is a precursor to delamination within the skin. Furthermore, most solid elements exhibit a STATUSXFEM value of 1, signifying notable matrix degradation, which creates favorable conditions for crack migration. The undamaged cohesive elements at the skin-filler interface overlaid on the outer 45° ply, are shown in Figure 7.15. The crack extension within the skin-filler interface terminates near the area of significant matrix crack degradation, reinforcing the notion that migration is indeed occurring in the stiffened panel under out-of-plane loading.

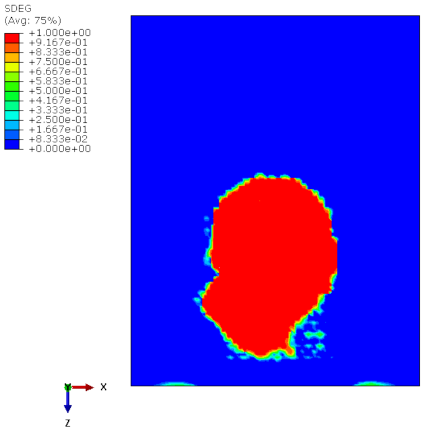

Figure 7.12: Delamination in 45/-45 interface

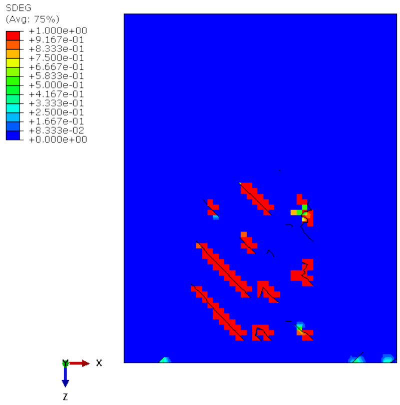

Figure 7.13: Matrix cracks in 45° ply

The force response of the panel is presented in Figure 7.16, where the peak force predicted by this model is 3.6 kN. Notably, the stiffness of the panel in this simulation is higher than that observed in the shell model. However, the peak load predicted by both simulations remains comparable. The post-peak response of the XFEM-CE model diverges from that of the shell model, as the force remains relatively constant with further displacement. After the peak load, the matrix cracks in 45° ply facilitate a path for crack propagation into the skin. This phenomenon is illustrated in Figure 7.17, where the bulk elements on one side of the crack exhibit out-of-plane deformation, leading to the initiation and extension of delamination beneath the ply. Additionally, the cracks are aligned along the fiber direction, and the orientation of the cracks within the ply enhances the energy dissipation of the matrix crack.

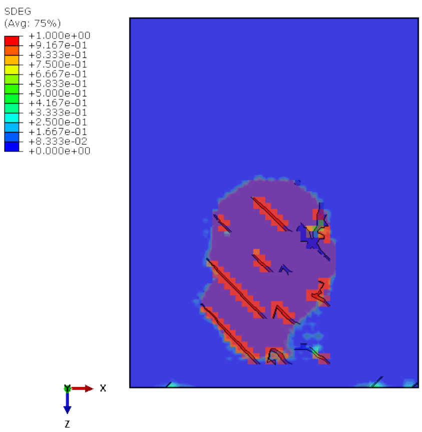

Figure 7.14: Matrix cracks in 45° ply overlayed on cohesive elements in 45/-45 interface

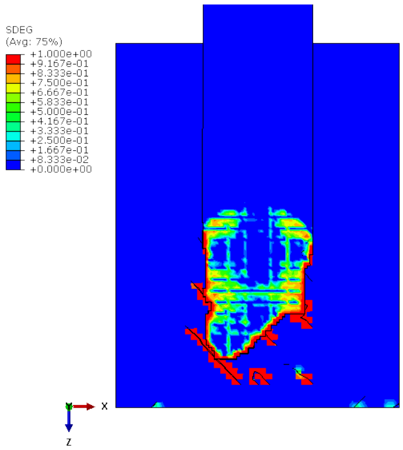

Figure 7.15: Cohesive elements in skin-filler interface overlayed on 45° ply

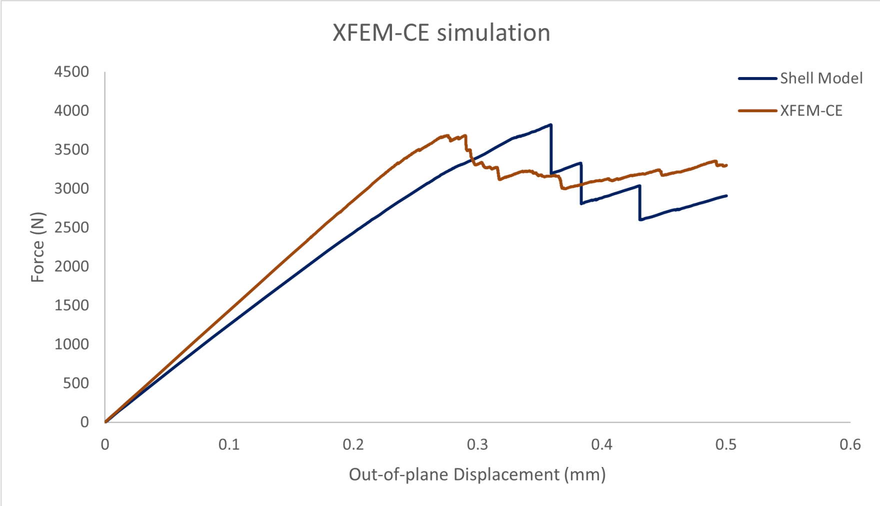

Figure 7.16: Force response of the applied load

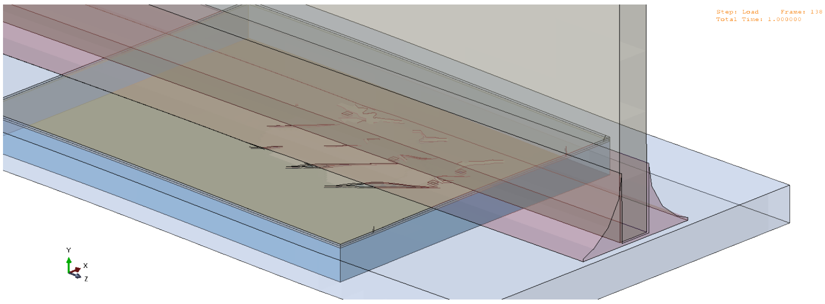

Figure 7.17: Cross-section and detailed view of matrix cracks in the outer ply which create favorable conditions for crack migration

7.6 Discussion

The mode I crack extension observed in the shell model does not manifest at the skin-filler interface when matrix failure and ply delamination are incorporated into the model. In this scenario, matrix cracks initiate in the outer ply due to significant transverse and out-of-plane stresses. As loading continues, these matrix cracks degrade, leading to peeling of the material on one side, which subsequently initiates delamination in the 45°/-45° interface. As a result, the remaining load is diverted toward extending the delamination rather than propagating the crack at the skin-filler interface. The crack at the skin-filler interface primarily extends near the edges, leaving a substantial portion of the material at the interface intact within the ply. Figure 7.17 illustrates the matrix cracks present in the outer ply. Notably, both delamination and matrix cracks remain largely confined to the filler region, with minimal extension of the cracks or ply delamination extending beyond the filler boundary. This behavior suggests that the higher fracture energy of the filler interface may make crack migration more favorable than skin-stiffener separation. However, accurately characterizing the fracture properties of the filler interface is essential for understanding this migration tendency in this structure. It is crucial to consider the propensity for migration in order to effectively predict the fracture energy of the filler interface.

Chapter 8

Conclusions and Recommendations

Having performed the migration test and the bending simulation of the butt-joint skin-stiffener with XFEM and cohesive elements, the research question can now be answered. Firstly, the sub-questions will be answered based on the conclusion of the results.

1. How effective can matrix crack determined by LaRC05 be in predicting the interaction of matrix crack and delamination?

   The LaRC05 failure criterion effectively predicts the orientation of matrix cracks, which is crucial for accurately assessing energy dissipation during the degradation of these cracks. The crack orientation is directly influenced by the strength of the matrix material, making it imperative to calibrate the strength values employed in the simulations to ensure reliable migration predictions. This calibration process necessitates rigorous validation to confirm that the model accurately reflects the material behavior. Given that the migration phenomenon in the test is primarily driven by shear stress, accurate characterization of shear strength will enhance the reliability of the predictions.

2. How accurate is this combination of XFEM with standard cohesive elements in predicting the interaction of matrix cracks and delamination?

   The migration test simulations predicted crack migration in most cases. The matrix degradation occurring near the cohesive interface led to significant delamination. To mitigate errors arising from cohesive elements that share nodes with adjacent solid elements, sufficient refinement of the cohesive elements is essential. While mesh ties can be employed to connect different parts, this approach may significantly increase the number of degrees of freedom (DOFs), thereby escalating computational requirements.

   Although the combination of the methods used captures the propensity for migration, the overall response of the laminate may not be fully reliable. This modeling approach serves as a valuable tool for providing an initial estimate of the damage sequence. However, for more accurate predictions regarding migration locations and the load response, alternative strategies—such as enriching the cohesive interface—could yield improved approximations. These enhancements would allow for a more detailed representation of the damage mechanisms, ultimately leading to better predictions of the structural behavior under various loading conditions.

3. How do numerical parameters influence the interaction of matrix cracks and delamination?

   Since both damage mechanisms are predicted using cohesive zone models, the methodologies inherently exhibit mesh dependency. Consequently, a finer mesh is often required to accurately capture the interactions between matrix cracks and delamination. To mitigate potential inaccuracies in kinematics, the number of cohesive elements per solid element must exceed one. This approach ensures that the model sufficiently represents the complex behavior of materials at the interfaces, thereby reducing errors that could arise from simplified kinematic assumptions.

   Careful attention must be given to mesh refinement during simulations to achieve reliable and accurate predictions of the interactions between different damage modes in composite structures. To this end, a dedicated mesh refinement study for the cohesive elements is essential. This study will help identify the optimal mesh configuration needed to capture the nuances of the damage mechanisms effectively, ultimately improving the overall predictive capability of the model. In this thesis, using two cohesive elements per solid element along the length was found to predict migration, while a finer mesh required additional loading.

4. How do material parameters influence the interaction of matrix cracks and delamination?

   The fracture energy of the delamination and matrix material was considered in the parametric study. Although monotonic results were not obtained, some trends that were observed could be discussed. Lowering the matrix strength while holding the fracture energy constant appears to delay migration. For the same interlaminar and intralaminar strength, a higher matrix fracture energy delays the migration. Lower matrix fracture energy also seemed to delay migration since the cohesive interface that the matrix crack reaches has higher fracture energy. However, this would require further validation through experiments or damage simulations using different modeling techniques.

   To answer this in a better manner, sufficient calibration of the matrix strength would be required followed by ensuring mesh objective solutions can be obtained from the simulation such that monotonic trends are observed for a range of material properties. However, this is not straightforward as the literature also indicates complexities in migration prediction when different strength values are considered as shown in [49].

5. To what extent does accounting for a discrete matrix crack and interlaminar failure in the skin influence the response of the stiffened panel?

   In the simulation of the stiffened butt-joint panel, no delamination was observed when matrix cracks were excluded from the model. However, significant delamination emerged when discrete matrix cracks were predicted using the eXtended Finite Element Method (XFEM). The structural response varied markedly with the inclusion of matrix cracks; for instance, the crack profiles at the skin-stiffener interface exhibited distinct differences, and the extent of damage at the skin-filler interface was notably reduced compared to models that did not account for matrix cracking.

Despite these insights, the global response of the structure requires further verification and validation, as the stiffness response obtained from the XFEM model differed significantly from that of the panel modeled using shell elements. Moreover, the accuracy of the post-peak response is uncertain; the combination of standard cohesive elements and XFEM may not accurately capture the kinematics at the matrix crack tip. Consequently, additional studies and validation are deemed necessary to enhance the reliability of the predictions.

Having addressed the sub-questions, the main research question can be conclusively answered. The XFEM-CE approach is effective in capturing the interaction between the two primary damage mechanisms: matrix cracking and delamination. These mechanisms are essential to understanding the migration phenomenon. While this modeling technique can predict the propensity for migration, achieving an accurate response necessitates substantial verification and validation efforts.

Additionally, the method's mesh dependency underscores the need for a fine mesh in regions where damage is anticipated. However, the high fracture energy characteristic of thermoplastic composite materials permits the use of a sufficiently coarse mesh in these areas, enabling the prediction of damage interactions at a structural level. This capability highlights the XFEM-CE approach as a valuable tool for analyzing and understanding complex damage behaviors in composite structures, while also pointing to the need for ongoing refinement in modeling practices to enhance predictive accuracy.

8.1 Future scope and recommendation

The objective of this thesis was to capture the delamination within the stiffened panel using the computational fracture mechanics method. It was hypothesized that delamination is a consequence of migration and this hypothesis has been accepted based on the current simulation. However, further verification or validation would be required to improve the confidence of this hypothesis. Some of the following themes could be considered for future research.

1. Crack migration validation for thermoplastic composite materials

   The higher fracture toughness and longer cohesive zone associated with thermoplastic composite materials make non-linear fracture simulations more computationally efficient compared to those conducted on thermoset composites, which often have smaller cohesive zones. In this thesis, the crack migration test simulation was focused on thermoset composite materials, presenting notable computational challenges due to the necessary mesh refinement.

   However, in light of the need to predict migration behaviors for novel aeronautical structures likely to be manufactured from thermoplastic composites, future migration tests paired with virtual test campaigns could be implemented. The primary goal of this test campaign would be to generate the material strength parameters required for the LaRC05 failure criterion. Doing so would facilitate the accurate prediction of matrix crack orientation, enhancing the reliability and applicability of the XFEM-CE approach in assessing the structural integrity of advanced composite materials used in aeronautics. This strategy underscores the importance of aligning material characterization efforts with the specific demands of predictive modeling in composite applications.

2. Butt-joint filler material characterization

   The fracture properties of the butt-joint filler material must be carefully characterized while ensuring that no migration occurs in the specimen. This process will also require monitoring the propensity for matrix cracks to develop in the plies at the interface. A virtual Double Cantilever Beam (DCB) or End Notch Flexure (ENF)-type test could be conducted for the butt joint using a mesoscale model in conjunction with the XFEM-CE method. Provided that the interlaminar and intralaminar properties are accurately defined, this approach would allow for the assessment of the propensity for migration.

   To mitigate migration, adjustments could be made to the layup configuration while ensuring that no matrix cracks develop in the outer ply. This strategy could pave the way for new experimental campaigns aimed at accurately determining the fracture energy of the skin-filler interface.

3. Post-bucking simulations

   The global-local approach employed in this study can be extended to simulate the panel in the post-buckled state, providing a valuable framework for conducting verification and validation studies. These studies could assess whether this modeling technique accurately captures the structural response during and after buckling events. The XFEM-CE method would also facilitate the evaluation of crack migration in this context. Similar studies, such as those presented in [46], have employed Continuum Damage Mechanics (CDM) using explicit time integration for post-buckling simulations. A comparative analysis between these two modeling approaches—XFEM-CE and CDM—could be conducted for the stiffened butt-joint panel, offering deeper insights into the effectiveness of the XFEM-CE methodology in predicting structural behavior under various loading conditions. Moreover, alternative methods such as the Floating Node Method (FNM) could be utilized to model the entire laminate and predict both migration and the global response of the laminate more accurately. Integrating these methodologies could enhance the predictive capabilities of damage modeling in composite structures, leading to improved design strategies and structural integrity assessments in aeronautical applications.

References

[1] J G Ratcliffe, M W Czabaj, and T K O'brien. A Test for Characterizing Delamination Migration in Carbon/Epoxy Tape Laminates.

[2] M F Pernice, N V. De Carvalho, J G. Ratcliffe, and S R. Hallett. Experimental study on delamination migration in composite laminates. *Composites Part A: Applied Science and Manufacturing*, 73:20–34, 6 2015.

[3] H. Mohammad and S. Mousa. Finite element modeling strategies for 2D and 3D delamination propagation in composite DCB specimens using VCCT, CZM and XFEM approaches. *Theoretical and Applied Fracture Mechanics*, 103:102246, 10 2019.

[4] Y. Mi, M. A. Crisfield, G. A.O. Davies, and H. B. Hellweg. Progressive Delamination Using Interface Elements. 32(14):1246–1272, 7 1998.

[5] P P Camanho, C G Dávila, and M F de Moura. Numerical simulation of mixed-mode progressive delamination in composite materials. *Journal of composite materials*, 37(16):1415–1438, 2003.

[6] T. A, P P Camanho, C. J, and C G Dávila. A damage model for the simulation of delamination in advanced composites under variable-mode loading. *Mechanics of materials*, 38(11):1072–1089, 2006.

[7] B van Dongen, A van Oostrum, er, and Z. Dimitrios. A blended continuum damage and fracture mechanics method for progressive damage analysis of composite structures using XFEM. *Composite Structures*, 184:512–522, 1 2018.

[8] X Wang, Z Guan, S Du, G Han, and Z Li. An accurate and easy to implement method for predicting matrix crack and plasticity of composites with an efficient search algorithm for LaRC05 criterion. *Composites Part A: Applied Science and Manufacturing*, 131:105808, 4 2020.

[9] S. Wei, G. Zhidong, and L. Zengshan. Simulation of Low Velocity Impact Induced Inter- and Intra-Laminar Damage of Composite Beams Based on XFEM. *Applied composite materials*, 24(6):1459–1477, 2017.

[10] L B Zhao, Z. J, J Y Zhang, Z L Liu, and H. N. XFEM simulation of delamination in composite laminates. *Composites part a-applied science and manufacturing*, 80:61–71, 2016.

[11] X. J. Fang, Q. D. Yang, B. N. Cox, and Z. Q. Zhou. An augmented cohesive zone element for arbitrary crack coalescence and bifurcation in heterogeneous materials. *International Journal for Numerical Methods in Engineering*, 88(9):841–861, 12 2011.

[12] B Y Chen, T E Tay, S T Pinho, and V B C Tan. Modelling delamination migration in angle-ply laminates. *Composites science and technology*, 142:145–155, 2017.

[13] X F Hu, B Y Chen, M Tirvaudey, V B C Tan, and T E Tay. Integrated XFEM-CE analysis of delamination migration in multi-directional composite laminates. *Composites part a-applied science and manufacturing*, 90:161–173, 2016.

[14] R Krueger, J G. Ratcliffe, and P J. Minguet. Panel stiffener debonding analysis using a shell/3D modeling technique. *Composites Science and Technology*, 69(14):2352–2362, 11 2009.

[15] A C Orifici, R S Thomson, D. R, B. C, Bay, and o. J. A finite element methodology for analysing degradation and collapse in postbuckling composite aerospace structures. *Journal of Composite Materials*, 43(26):3239–3263, 2009.

[16] A. Raimondo and A. Riccio. Inter-laminar and intra-laminar damage evolution in composite panels with skin-stringer debonding under compression. *Composites Part B: Engineering*, 94:139–151, 6 2016.

[17] Abaqus 6.14 Documentation.

[18] C Soutis. Fibre reinforced composites in aircraft construction. *Progress in aerospace sciences*, 41(2):143–151, 2005.

[19] C Kassapoglou and M Kaminski. Modeling damage and load redistribution in composites under tension–tension fatigue loading. *Composites Part A: Applied Science and Manufacturing*, 42(11):1783–1792, 2011.

[20] K. Martin. Analysis of failure in fiber polymer laminates: The theory of alfred puck. *Analysis of Failure in Fiber Polymer Laminates: The Theory of Alfred Puck*, pages 1–205, 2008.

[21] S. R. Hallett, B. G. Green, W. G. Jiang, and M. R. Wisnom. An experimental and numerical investigation into the damage mechanisms in notched composites. *Composites Part A: Applied Science and Manufacturing*, 40(5):613–624, 5 2009.

[22] F P. van der Meer. Mesolevel Modeling of Failure in Composite Laminates: Constitutive, Kinematic and Algorithmic Aspects. *Archives of Computational Methods in Engineering 2012 19:3*, 19(3):381–425, 8 2012.

[23] P. Maimí, P. P. Camanho, J. A. Mayugo, and C. G. Dávila. A continuum damage model for composite laminates: Part I – Constitutive model. *Mechanics of Materials*, 39(10):897–908, 10 2007.

[24] C. Furtado, G. Catalanotti, A. Arteiro, P. J. Gray, B. L. Wardle, and P. P. Camanho. Simulation of failure in laminated polymer composites: Building-block validation. *Composite Structures*, 226:111168, 10 2019.

[25] Z P. Bažant and B. H. Oh. Crack band theory for fracture of concrete. *Matériaux et Constructions*, 16(3):155–177, 5 1983.

[26] K. Ronald. Virtual crack closure technique: History, approach, and applications. *Applied Mechanics Reviews*, 57(1):109 – 143, 1 2004.

[27] K. S. van Dooren, B.H.A.H. Tijs, J.E.A. Waleson, and C. Bisagni. Skin-stringer separation in post-buckling of butt-joint stiffened thermoplastic composite panels. *Composite Structures*, 304:116294, 1 2023.

[28] D. S. Dugdale. Yielding of steel sheets containing slits. *Journal of the Mechanics and Physics of Solids*, 8(2):100–104, 5 1960.

[29] A. Turon, P. P. Camanho, J. Costa, and J. Renart. Accurate simulation of delamination growth under mixed-mode loading using cohesive elements: Definition of interlaminar strengths and elastic stiffness. *Composite Structures*, 92(8):1857–1864, 7 2010.

[30] A Turon, C G Dávila, P P Camanho, and J Costa. An engineering solution for mesh size effects in the simulation of delamination using cohesive zone models. *Engineering fracture mechanics*, 74(10):1665–1682, 2007.

[31] J. M. Melenk and I. Babuška. The partition of unity finite element method: Basic theory and applications. *Computer Methods in Applied Mechanics and Engineering*, 139(1-4):289–314, 12 1996.

[32] N Moës, J Dolbow, and T Belytschko. A finite element method for crack growth without remeshing. *International Journal for Numerical Methods in Engineering*, 46(1):131–150, 1999.

[33] Anita Hansbo and Peter Hansbo. A finite element method for the simulation of strong and weak discontinuities in solid mechanics. *Computer Methods in Applied Mechanics and Engineering*, 193(33):3523–3540, 2004.

[34] B. H.A.H. Tijs, K. S. van Dooren, and C Bisagni. Development of a Numerical Framework for Virtual Testing to Support Design of a Next Generation Thermoplastic Multifunctional Fuselage. *II European Conference On Multifunctional Structures (EMuS2020), November, 17-18, 2020*, 2 2021.

[35] Y Shi, T Swait, and C Soutis. Modelling damage evolution in composite laminates subjected to low velocity impact. *Composite structures*, 94(9):2902–2913, 2012.

[36] B. Y. Chen, T. E. Tay, P. M. Baiz, and S. T. Pinho. Numerical analysis of size effects on open-hole tensile composite laminates. *Composites Part A: Applied Science and Manufacturing*, 47(1):52–62, 4 2013.

[37] N A Petrov, G. Larissa, and Stepan V Lomov. A parametric study assessing performance of eXtended Finite Element Method in application to the cracking process in cross-ply composite laminates. *Composite structures*, 187:489–497, 2018.

[38] F P. Van Der Meer and C G. Dávila. Cohesive modeling of transverse cracking in laminates under in-plane loading with a single layer of elements per ply. *International Journal of Solids and Structures*, 50(20-21):3308–3318, 10 2013.

[39] B. Y. Chen, S. T. Pinho, N. V. De Carvalho, P. M. Baiz, and T. E. Tay. A floating node method for the modelling of discontinuities in composites. *Engineering Fracture Mechanics*, 127:104–134, 9 2014.

[40] N. V. De Carvalho, B. Y. Chen, S. T. Pinho, J. G. Ratcliffe, P. M. Baiz, and T. E. Tay. Modeling delamination migration in cross-ply tape laminates. *Composites Part A: Applied Science and Manufacturing*, 71:192–203, 4 2015.

[41] T E Tay, X S Sun, and V B C Tan. Recent efforts toward modeling interactions of matrix cracks and delaminations: an integrated XFEM-CE approach. *Advanced composite materials*, 23(5-6):391–408, 2014.

[42] B. Ismet, L L Warnet, and A. Remko. Assessment of failure and cohesive zone length in co-consolidated hybrid C/PEKK butt joint. *Engineering structures*, 168:420–430, 2018.

[43] D M Grogan, C M O Brádaigh, and S B Leen. A combined XFEM and cohesive zone model for composite laminate microcracking and permeability. *Composite structures*, 120:246–261, 2015.

[44] R. Vescovini, C. G. Dávila, and C. Bisagni. Failure analysis of composite multi-stringer panels using simplified models. *Composites Part B: Engineering*, 45(1):939–951, 2 2013.

[45] C Meeks, E Greenhalgh, and B G. Falzon. Stiffener debonding mechanisms in post-buckled CFRP aerospace panels. *Composites Part A: Applied Science and Manufacturing*, 36(7):934–946, 7 2005.

[46] J Action and F A. Leone. Progressive damage failure analysis of a multi-stringer post-buckled panel. *AIAA Scitech 2020 Forum*, 1 PartF, 2020.

[47] X. Lu, M. Ridha, B.Y. Chen, V.B.C. Tan, and T.E. Tay. On cohesive element parameters and delamination modelling. *Engineering Fracture Mechanics*, 206:278–296, 2 2019.

[48] B. H.A.H. Tijs, S. Abdel-Monsef, J. Renart, A. Turon, and C. Bisagni. Characterization and analysis of the interlaminar behavior of thermoplastic composites considering fiber bridging and R-curve effects. *Composites Part A: Applied Science and Manufacturing*, 162:107101, 11 2022.

[49] N V De Carvalho, B R Seshadri, J.G Ratcliffe, G.E Mabson, and L.R. Deobald. Title: Simulating matrix crack and delamination interaction in a clamped tapered beam. *Boeing Research and Technology*, page 98124.